In-situ Polymerization of Diacetylene Ligands for Applications in Quantum Dot Solar Cells



Daniel A.F. Gregory

St Catherine's College

Hilary Term 2021

A thesis submitted in fulfillment of requirement for the degree of

DPhil in Materials at the University of Oxford

Abstract

Improving the efficiency of next-generation solar cells is crucial to their commercialization. This thesis presents a novel approach to coupled organic-inorganic nanostructures through *in-situ* polymerization of a ligand, creating an extended, delocalized sp^2 environment surrounding lead sulfide (PbS) quantum dots in a thin film.

Through the design of this novel, *in-situ* polymerizing ligand, ligand exchange dynamics are explored by looking at terminal alkynes, primary amines, and carboxylic acids as anchoring moieties. Using Fourier Transform Infrared Spectroscopy (FTIR) and X-ray Photoelectron Spectroscopy (XPS), it is shown that terminal alkynes and primary amines do not coordinate to PbS quantum dots, and that ligands containing sp-hybridized bonds can influence the band position of thin films through successful coordination via a carboxylic acid coordinating group. A proof-of concept diacetylene ligand, dodeca-5,7-diynedioic acid (D57DDA) is synthesized and coordinated to PbS quantum dots, confirmed through the use of XPS. *In-situ* polymerization of the diacetylene ligand is confirmed using FTIR and XPS. Finally, solar cells incorporating the novel D57DDA ligand are fabricated and compared to PbS quantum dot control devices. Devices using the coupled organic-inorganic nanostructure as the hole-transport layer show comparable device efficiencies to control devices at 4%, with performance improving with increased UV exposure. This is hypothesized to be due to the polymer's band alignment with the quantum dots leading to efficient charge transfer of holes and increased mobility through the hole-transport layer. Impurities, believed to be chloride ions introduced in the ligand synthetic isolation, are shown to improve device performance with their absence reducing short circuit current.

Acknowledgements

Completing a DPhil in the best of circumstances is always challenging, completing one in the middle of a pandemic requires a mental fortitude that can only be achieved with a strong community of support. This thesis is dedicated to that support network.

Firstly, I'd like to thank my supervisors for this thesis, Professor Andrew Watt & Professor Hazel Assender, for their guidance throughout my degree both technical and personal. From discussing ideas, to being patient with my acquisition of the DPhil thought process, to data acquisition and analysis, to helping me develop coping mechanisms for the stress and time management, I could not have done this without either of you. Begbroke can be an isolating place to work, so to the many faces coming through the lab I'd like to thank you all for wonderful companionship, in particular Wing Chung Liu, Assia Kasdi, and Zheng Zhang. To Neil Young and Gareth Hughes, thank you for your considerable patience with my electron microscopy training. Likewise, I extend my thanks to Wolfgang Stockinger from the Chemistry department, Iago Pozo in Materials, and Manuel Klober-Cznery and Suer Zhou from Physics for your advice and guidance with the troubleshooting of my organic syntheses, assisting in my cyclic voltammetry measurements, and running/helping analyze my Photoluminescence experiments, respectively.

A list of all of the many people across Oxford who helped make my stay so pleasant would make this the longest section of my thesis, and I would inevitably leave some of you out by accident. There are so many of you who have fueled my many curiosities and enriched my stay. For this I am exceedingly grateful, you have helped me grow as a person in so many ways, often unexpected. I would like to make a special dedication to the Oxford University Athletics Club, a much needed and often overused escape from the frustrations inherent in undertaking this degree. I would like to extend my gratitude in particular to Justin Leung, Lesley Bryant, and Ailsa Wallace for being

not only fantastic coaches and running mates but excellent humans and friends as well. To my family, thank you for your support and guidance through this degree, helping me to maintain my focus and providing a safe space to recharge either online or occasionally in person whenever I felt overwhelmed. Your constant encouragement has been a reminder of why I wanted to start this and given me confidence when I most needed it to finish it. To my partner, Irene Gibson, thank you for believing in me, being my emotional and mental support, and a guiding light towards finishing the largest project I have ever undertaken. Your encouragement that I can do this and checking in that I want has helped me to become more organized, less anxious, and improved me as both a scientist and a person. I'd also like to thank Hanwei Fang, Anna Niedbala, and Emily Sellman for their constant, positive support, and powerful friendship, all of which have been immensely appreciated. Having your stories and experiences during this degree to ground my expectations and mentally prepare for the challenging phases of a DPhil has been incredible, I have tried to pay it forward.

Finally, I'd like to specially acknowledge to the inspiration for its undertaking, my grandfather, Alan Frank Gregory, PhD. Your encyclopedic knowledge of rocks I would bring you on the beach as a kid and the stories behind them were what sparked my fascination with science as a field of study, and have ultimately led to this degree. Along the way I have learned of your experiences and stories, tried to replicate your athletic achievements, and done my best to take in all the wisdom you have offered. I can now look forward to the life that lies ahead, with your life serving as an excellent guide in that regard once again. Thank you.

Statement of Originality

The research and written report of this work has not, at time of submission, been reproduced in any academic journal. Further, no part of this work has been submitted, in whole or in part, as material for examination for any other degree at any other institution outside of the University of Oxford, Department of Materials. It serves only as material for the examination of the DPhil in Materials Science.

List of Abbreviations

PV – photovoltaic

(g/)kWh – (grams per) kilowatt hour

GW(/yr) – gigawatt (per year)

W/m^2 – watts per square meter

Wp – watts produced at peak production

MHz – megahertz, unit of frequency

SRH – Shockley-Reed-Hall

VRH – variable range hopping

eV – electron volt, unit of energy

PTFE – poly(tetrafluoroethylene)

Rpm – revolutions per minute

K – Kelvin, temperature unit

V_{bi} – built in voltage

V_{mp} – voltage at maximum power

J_{sc} – short-circuit current density

PbSe – lead selenide

TiO_2 – titanium dioxide

D57DDA – dodeca-5,7-diynedioic acid

EDT – ethanedithiol

EDA – ethanediamine

E_{tr} – transport energy

MTR – multiple trap and release

XPS – X-ray Photoelectron Spectroscopy

CO_2 – carbon dioxide

CIGS – copper Indium Gallium Sulfide/Selenide

FTIR – Fourier Transform Infrared Spectroscopy

UV – ultraviolet, class of wavelengths of light

KP – kelvin probe

H^1NMR – hydrogen nuclear magnetic resonance

C^{13}NMR – carbon nuclear magnetic resonance

FET – field effect transistor

DI – de-ionized

ppm – parts per million

k_B – Boltzmann Constant

V_{OC} – open circuit voltage

I_{mp} – current at maximum power

PbS – lead sulfide

CdS – cadmium sulfide

ZnO – zinc oxide

P3HT – poly(3-hexylthiophene)

TBAI – tetrabutylammonium iodide

HTL – hole-transport layer

HOMO – highest occupied molecular orbital

LUMO – lowest unoccupied molecular orbital

Table of Contents

Abstract 1
Acknowledgements 2
Statement of Originality 4
List of Abbreviations 4
Table of Contents 5
1 Introduction 9
1.1 The Big Picture 9
1.1.1 The Case for Renewable Energy 9
1.1.2 Wider Impact of Photovoltaic Technology on Society 9
1.1.3 Current Market Share of Photovoltaic Technologies 10
1.1.4 Advantages of Quantum dot solar cells 11
1.2 Key Photovoltaics Concepts 12
1.2.1 Blackbody Radiation and the Solar Spectrum 12
1.2.2 Formation of a p-n junction 13
1.2.3 Operating Principles of Photovoltaics 16
1.2.4 Mobility, Lifetime, and Recombination 20
1.2.5 Limits of Photovoltaic Efficiency 21
1.3 Key Quantum Dot and Organic Semiconductor Concepts 22
1.3.1 Semiconductors and Quantum Dots 23
1.3.2 Quantum dot band position control 26
1.3.3 Quantum Dot solar cell design 27
1.4 Charge Transport in and Transfer between Semiconductors 30
1.4.1 Charge Transport in bulk semiconductors 31
1.4.2 Charge Transport in Quantum Dot Semiconductors 31
1.4.3 Charge Transport in Organic Semiconductors 35
1.4.4 Lead-site trap states 37
1.4.5 Charge Transfer between Quantum dots and Organic Semiconductors 39
1.5 Mobility and Lifetime of charges 40
2 Literature Review 41
2.1 Principles of Quantum Dot synthesis 42
2.2 Improving Quantum Dot Solar Cell Performance 44
2.3 Core-Shell Passivation 45
2.4 Ligand Passivation 46

2.4.1 Synthetic Ligands for Devices 48
2.4.2 Ligand Exchange 49
2.4.3 Small Organic Ligands 50
2.4.4 Halide and Pseudo-halide ligands 51
2.4.5 Conjugated Ligands 53
2.4.6 Coupled Organic Inorganic Nanostructures (COINs) 53
2.4.7 Hybrid Polymer-nanostructure devices 55
2.5 Diacetylenes 57
2.5.1 Topochemical polymerization 58
2.5.2 Diacetylene Photovoltaics 60
2.6 Summary of concepts 60
3 Methods 62
3.1 PbS Nanoparticle Synthesis 62
3.2 ZnO Nanoparticle Synthesis 64
3.3 ITO substrate preparation and Cleaning 64
3.4 Solid State Ligand Exchange Process 65
3.5 Solution Ligand Exchange Process 66
3.6 Gold top-contact evaporation 66
3.7 Synthesis of dodeca-5,7-diynedioic acid 66
3.8 Work-up recrystallization method for Dodeca-5,7-diynedioic acid 67
3.9 FTIR spectroscopy 67
3.9.1 FTIR spectrum of Quantum dot thin films with propargylamine 68
3.9.2 FTIR spectra of 2-butynoic acid quantum dot thin films 70
3.9.3 FTIR spectra of UV-cured Dodeca-5,7-diynedioic acid quantum dot thin films 71
3.10 UV-vis Spectroscopy 72
3.11 Raman Spectroscopy 73
3.12 Nuclear Magnetic Resonance (NMR) Spectroscopy 75
3.13 Kelvin Probe 76
3.14 X-ray Photoelectron Spectroscopy (XPS) 77
3.14.1 XPS elemental scans with peak fitting of amine-passivated PbS quantum dot films 82
3.14.2 XPS elemental scans with peak fitting of 2-butynoic-passivated PbS quantum dot films 83
3.14.3 XPS elemental scans with peak fitting of dodeca-5,7-diynedioic acid passivated films 85
3.15 Transmission Electron Microscopy (TEM) 86

3.16 Cyclic Voltammetry Measurements 87
3.17 Current-Voltage characterization 89
3.17.1 Illuminated J-V characteristics of D57DDA passivated PbS in different device layers 89
3.17.2 Illuminated J-V characteristics of different hole-transport layers incorporating D57DDA 90
3.17.3 Illuminated J-V characteristics of devices with respect to UV irradiation time 91
4 Coordination of alkyne-based ligands to the quantum dots. 93
4.1 Introduction 93
4.2 Terminal Amine Ligand Exchange Dynamics 94
4.2.1 Results 95
4.2.2 Discussion 97
4.3 Carboxylic Acid as an Anchor Moiety for alkyne-based ligands 101
4.3.1 Results 102
4.3.2 Discussion 102
4.4 Coordination of Terminal Alkynes to PbS Quantum Dots 105
4.4.1 Results 105
4.4.2 Discussion 106
4.5 Conclusions of Chapter 4 107
5 Synthesis and Coordination of Diacetylene Ligand 110
5.1 Introduction 110
5.2 Ligand Requirements 112
5.3 Ligand Design 113
5.4 Synthesis of dodeca-5, 7-diynedioic acid 116
5.5 Discussion 117
5.6 Coordination of ligand to quantum dots 119
5.7 Discussion 122
5.8 Conclusions of Chapter 5 123
6 Characterizing Quantum Dot-Polydiacetylene Photovoltaic Devices 125
6.1 Introduction 125
6.2 Quantum dot- Poly(diacetylene) layer positioning and comparison 126
6.2.1 Discussion 126
6.3 Effect of UV curing on Hole-Transport layer 129
6.3.1 Discussion 129
6.4 Nature of purified Diyne's poor performance 132
6.4.1 Discussion 134

6.5 Conclusion 135
7 Conclusions and future work 136
7.1 Conclusions of the Thesis 136
7.2 Future Work 138
8 References 139

1 Introduction

1.1 The Big Picture

1.1.1 The Case for Renewable Energy

As humans have developed ever more sophisticated and interconnected societies, the world's energy demands have steadily and rapidly increased. Speaking in broad terms, since Europe's industrial revolution in the mid-19th century, this demand for energy has largely been met by burning fossil fuels such as coal, oil, and gas. The burning of these fuels has released ever increasing amounts of carbon dioxide (CO_2) into the atmosphere, anywhere from 400-1000 g/kWh depending on the type of fuel burned [1],[2]. This build-up of CO_2 has many far-reaching consequences, predominantly the exacerbation of the greenhouse effect, raising global temperatures at an unprecedented rate [3]. As the world faces the reality of climate change, one of the most important challenges is the shift of energy generation from non-renewable to renewable sources[4].

1.1.2 Wider Impact of Photovoltaic Technology on Society

The electromagnetic radiation output of the sun provides energy to the earth by which life can sustain its eternal fight against increasing entropy. Conversion of light to chemical energy has been honed by nature over billions of years in the form of plant life, producing the biomass and fossil fuels that humans have learned to extract for energetic, mechanical, and chemical gain over our species' existence. Uneven heating of the atmosphere results in winds and the water cycle, fluid movements we have turned into electric power through the development of turbines. Most directly, incident radiation from the sun supplies an endless, if intermittent, source of light and heat that can be concentrated or converted to electricity. This thesis focuses on the direct conversion of electromagnetic radiation to electricity: solar photovoltaics. Whilst championed as a way of

decoupling developed economies from their historically large carbon dioxide emissions, photovoltaics arguably hold more promise as a leapfrog technology for developing nations to modernize without emitting vast quantities of greenhouse gases. In addition, the ubiquity of sunlight allows for photovoltaic deployment in remote locations where the logistics of fuel resupply can be particularly challenging. Based on this, solar photovoltaic technology has risen from laboratory test scale to an established commercial field over the past 50 years, with associated production costs associated falling dramatically in the past decade [5]. These falling production costs have brought additional benefits, with the energy payback time halving from 3.5 to 1.8 years between 2010 and 2015 [2].

1.1.3 Current Market Share of Photovoltaic Technologies

At present, the world's energy demand is met predominantly through the use of fossil fuels [4]. Globally, the International Energy Association's 2018 annual report documents solar PV accounting for 2.8% of global energy consumption. While the percentage is small, installed capacity continues to grow beyond original major milestones of 500 GW cumulative capacity and 100 GW yearly installed capacity [6]. Production capacity has ramped up significantly in recent years, with over 200 GW/yr expected to be installed in 2022. Installation of solar PV has been predominantly focused to select few countries, with the top 10 countries responsible for 87% of installed capacity. This coincides with the falling of the average electricity cost for solar PV, from \$0.32 to \$0.22/ Wp as of March 2020 [7]. In countries with abundant solar resources such as the United Arab Emirates, prices have fallen as low as \$0.03/ Wp [8]. Expansion is expected to increase with international collaboration, particularly in the EU, seen as a method of expanding capacity for these intermittent sources without wasting electricity production [4], [9], [10].

The market share within solar PV is dominated by mature technologies such as crystalline silicon, which hold 97% of the market. This market share has increased from 86% in 2011 and 92% in 2014, largely due to the scale-up in production from Southeast Asian countries and China [11]. Crystalline Silicon's dominance is largely due to the familiarity of silicon processing techniques to manufacturers, as high-quality silicon wafer production has been a mainstay of microelectronics and indeed solar research for over half a century. However, intense research into thin film technologies and the knowledge of photovoltaic systems from silicon has led to a rapid rate of innovation and efficiency gains in thin film PV technologies.

1.1.4 Advantages of Quantum dot solar cells

The commercial viability of next-generation solar cells will reply on a combination of high efficiency, low-cost, flexible processing methods and ability to combine with established technologies such as Silicon or CIGS. One promising technology in this regard is quantum dot photovoltaics. Low-cost synthesis and fabrication techniques and solution processing compatible with high-throughput manufacturing techniques such as roll-to-roll or inject printing offer the potential of low-cost panels on a range of flexible substrates, freeing solar cells from the bulky encapsulation of glass and steel. Moreover, simple control over the size of the quantum dots allows for precise control over the band gap, resulting in accurate tuning to the solar spectrum or the ability to work in tandem with other solar cell technologies. This size-dependent band gap also increases the library of photovoltaic materials, as previously unfavorable compounds become viable solar cell materials.

One of the more exciting possibilities of photovoltaics deploying quantum dots is their ability to surpass the Queisser limit, discussed later in section 1.2.5. They can do this through the conversion of one photon to more than one exciton, a process known as multiple exciton generation [12]–[16].

This would reduce carrier cooling losses and increase the number of charge carriers, giving overall improvements up to 44% power conversion efficiency under ideal conditions [17]–[19].

1.2 Key Photovoltaics Concepts

A full understanding of the work detailed in this thesis requires the explanation of specific scientific concepts. This section lays the foundation for a full conceptual understanding of the thesis by explaining the underlying processes governing inorganic and organic semiconductors, quantum dots, and solar photovoltaics.

1.2.1 Blackbody Radiation and the Solar Spectrum

Everything above absolute zero temperature, 0 K, emits electromagnetic radiation [20]. At 6000 K, the sun emits radiation predominantly in the ultraviolet, visible, and infrared regions. This radiation travels through the vacuum of space and hits the earth's atmosphere at a rate of 1337 W/m^2. However, through scattering and absorption, the air mass of the atmosphere dissipates much of this radiation, and the surface of the earth only receives between 100-300 W/m^2 [21], [22]. Figure 1.1 shows how solar emission at the edge of the atmosphere (red) is absorbed and scattered to give the spectrum on earth's surface as a result of the air mass index (blue, green). The most direct use of this radiation is solar photovoltaics, direct conversion of light to electricity. This section will conceptually explain the materials and processes involved in solar photovoltaic devices.

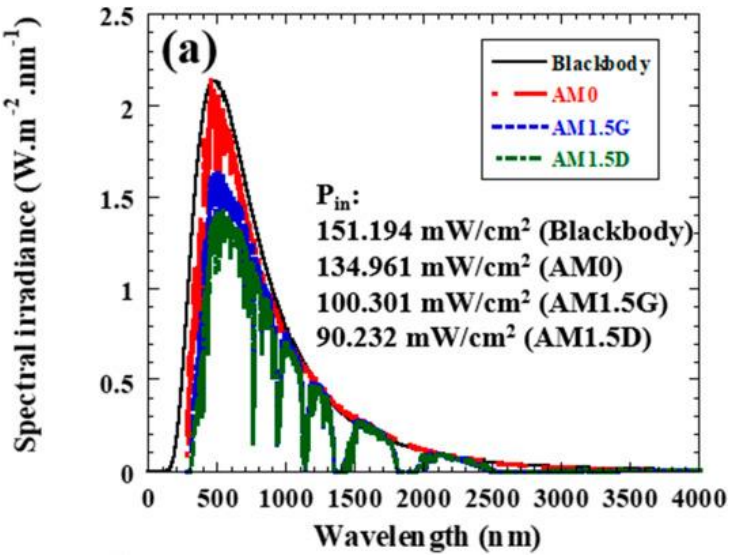


Figure 1.1 - Blackbody radiation from the sun (6000 K), at the edge of earth's atmosphere, (AM0), at the surface of the earth from direct radiation (AM1.5D) and direct & diffuse radiation (AM1.5G) as a function of the electromagnetic radiation's wavelength. Reprinted with permission from Chantana et al. [13]

1.2.2 Formation of a p-n junction

All materials have energy bands, formed from the overlap of energy levels in the atoms that constitute the material. As the bands are comprised of atomic energy levels, electrons fill them from the lowest to the highest available energy. The first band with available, unoccupied energy levels in it is called the conduction band, and the preceding one is known as the valence band. A semiconductor has a band gap between its conduction and valence bands, within which lies the Fermi level. The Fermi level is the energy level at which where there is a 50% chance of finding an electron in the material above zero kelvin. The probability of finding an electron in a different energy level E can be described by the following equation:

$$f(E) = \frac{1}{1+e^{(E-E_F)/k_bT}} \qquad \text{Eq. (1)}$$

Where k_b is the Boltzmann constant and T is the temperature in Kelvin. In both n and p-type semiconductors, one of the carriers is in the majority (electrons for n-type, holes for p-type) and the other is the minority carrier. As a result, n-type materials have a fermi level closer to the conduction band than the valence band, and p-type materials are the inverse. Charges generally do

not populate the conduction band unless they are given energy, either through light, heat, or applied potential difference. If more energy has been given than is necessary to reach the band edge, charge carriers will relax to this band edge and release heat, a process known as thermalization. While predominantly at the band edge, these charges do gain and lose small amounts of thermal energy and so are distributed in the band, with exponentially fewer carriers at energies further from the band edge. This carrier concentration n can be expressed according to the following exponential relation:

$$n \propto e^{-E/k_b T} \qquad \text{Eq. (2)}$$

Where E is the energy of the carrier, T is the temperature of the material in kelvin, and k_b is the Boltzmann constant. After a period of time, these charges will relax back across the band gap in a process known as recombination. This can be facilitated by energy states within the band gap, known as trap states and caused by defects in the material such as crystal dislocations or impurities. The average amount of time a charge remains excited for before recombining is known as the lifetime, τ.

When two materials of differing work function come into contact with each other, there is a difference in the concentration of charges. However, the fermi level must remain constant across the boundary. Charges compensate by diffusing across the interface, with electrons moving from the material with the higher work function to the lower and holes the opposite direction. The generated diffusion current, $J_{x,diff}$ can be described by the equation:

$$J_{n,diff} = q \frac{l_n^2}{2\tau_n} \frac{dn(x)}{dx} \qquad \text{Eq. (3)}$$

$$J_{p,diff} = -q\frac{l_p^2}{2\tau_p}\frac{dp(x)}{dx} \qquad \text{Eq. (4)}$$

Where $J_{x,diff}$ is diffusion current of the charges, q is elementary charge of electron, l_x is mean free path of the charge, τ is the lifetime of the charge and n,p are the concentrations of electrons and holes, respectively. Subscripts $_{n,p}$ refer to electron and hole values, respectively. This equation holds for one-dimensional diffusion. The diffusion current allows the Fermi level to remain constant across the junction, and causes a potential to form at the junction as formerly neutral regions gain or lose charge. This built in potential, V_{bi}, is determined by the difference in the original Fermi levels between the two materials:

$$V_{bi} = \frac{(E_{F,n} - E_{F,p})}{q} \qquad \text{Eq. (5)}$$

Where q is the elemental charge. The built in potential causes charges to dissociate across the junction. As the built-in potential increases from charges in causes creates a current $J_{x,drift}$ that opposes the diffusion current:

$$J_{x,drift} = q(n\mu_n + p\mu_p)E_x \qquad \text{Eq. (6)}$$

Where $J_{x,drift}$ is the drift current in the x-direction, q is elemental charge, E_x is the magnitude of the electric field in the x direction, n is the concentration of electrons, p is the concentration of holes, and $\mu_{n,p}$ is the mobility of electrons and holes, respectively. Again, this equation holds only for one-dimensional drift.

The system reaches an equilibrium where J_{drift} caused by V_{bi} balances out J_{diff} caused by the imbalanced fermi levels. Physically, the result is a region either side of the contact area where the material is charged and there are no free carriers, this is known as the depletion region or the space charge region. The built-in voltage acts within this region, and its width can be independently calculated for either side of the p-n interface:

$$w_n = \frac{1}{N_d}\sqrt{\frac{2\varepsilon_s(V_{bi}-V)}{q\left(\frac{1}{N_a}+\frac{1}{N_d}\right)}} \qquad \text{Eq. (7)}$$

$$w_p = \frac{1}{N_a}\sqrt{\frac{2\varepsilon_s(V_{bi}-V)}{q\left(\frac{1}{N_a}+\frac{1}{N_d}\right)}} \qquad \text{Eq. (8)}$$

Where ε_s is the permittivity of the semiconductor, q is the elemental charge, V_{bi} is the built-in voltage across the junction, V is the external applied potential to the junction, and N_a and N_d are the acceptor and donor atom densities, respectively. The equation above is based on the following assumptions:

1) The electric field V_{bi} is confined to the junction region, there is no electric field in the neutral region of the n- and p-type materials.
2) There are no free carriers in the depletion region

1.2.3 Operating Principles of Photovoltaics

The movement of charges in the diode is best explained by examining what happens when a potential is applied. Initially, it will be assumed that there is no light incident on the cell. If potential is applied to the diode, current will flow through the device as minority carriers recombine across the band gap. The rate at which this happens given an applied voltage is dependent on the minority carrier concentration, which is exponential as shown in equation. Relating all of these components together gives the Diode equation:

$$J = J_0\left(e^{\frac{V}{nk_bT}} - 1\right) \qquad \text{Eq. (9)}$$

Where J_0 is the saturation current density, n is the diode ideality factor, k_b is the Boltzmann constant, and T is the temperature of the diode in kelvin. Current is measured as a density per unit area, to make results across different sizes of solar panels comparable.

When light is incident on the material, it excites an electron into the conduction band, forming an exciton (an electron-hole pair). The potential across the depletion region causes these charges to move in opposite directions, where they can be collected by electrodes. When no contacts are applied, this current is at its highest, known as the short-circuit current or J_{sc}.

By contacting the cell's electrodes to a load, we can apply a potential opposing the V_{bi} that reduces this short circuit current. This will power the load and reduce the current collected from the device. The applied potential required to stop current flow is the open circuit voltage, or V_{oc}. It is important to note that this V_{oc} has an upper bound of the V_{bi}, but is often less in practice due to recombination of charges in the cell. This recombination reduces the maximum current that must be counteracted to achieve V_{oc} conditions.

The Quasi-Fermi level is a way of representing the average energy of one side of the junction when potential is applied to the system. This can be the application of an external voltage potential to the system, or the internal potential generated by photo-generated carriers after relaxing to the band edge. The fermi energies remain the same distance from the band gaps, but the as potential is applied the V_{bi} changes and the bands themselves move closer or further apart.

Revisiting the diode equations, a solar cell under illumination has a current even when no potential is applied due to the photo-generated charges, known as the photocurrent J_{ph}. This changes the diode equation to read as:

$$J = J_0 \left(e^{\frac{V}{nk_bT}} - 1 \right) - J_{ph} \qquad \text{Eq. (10)}$$

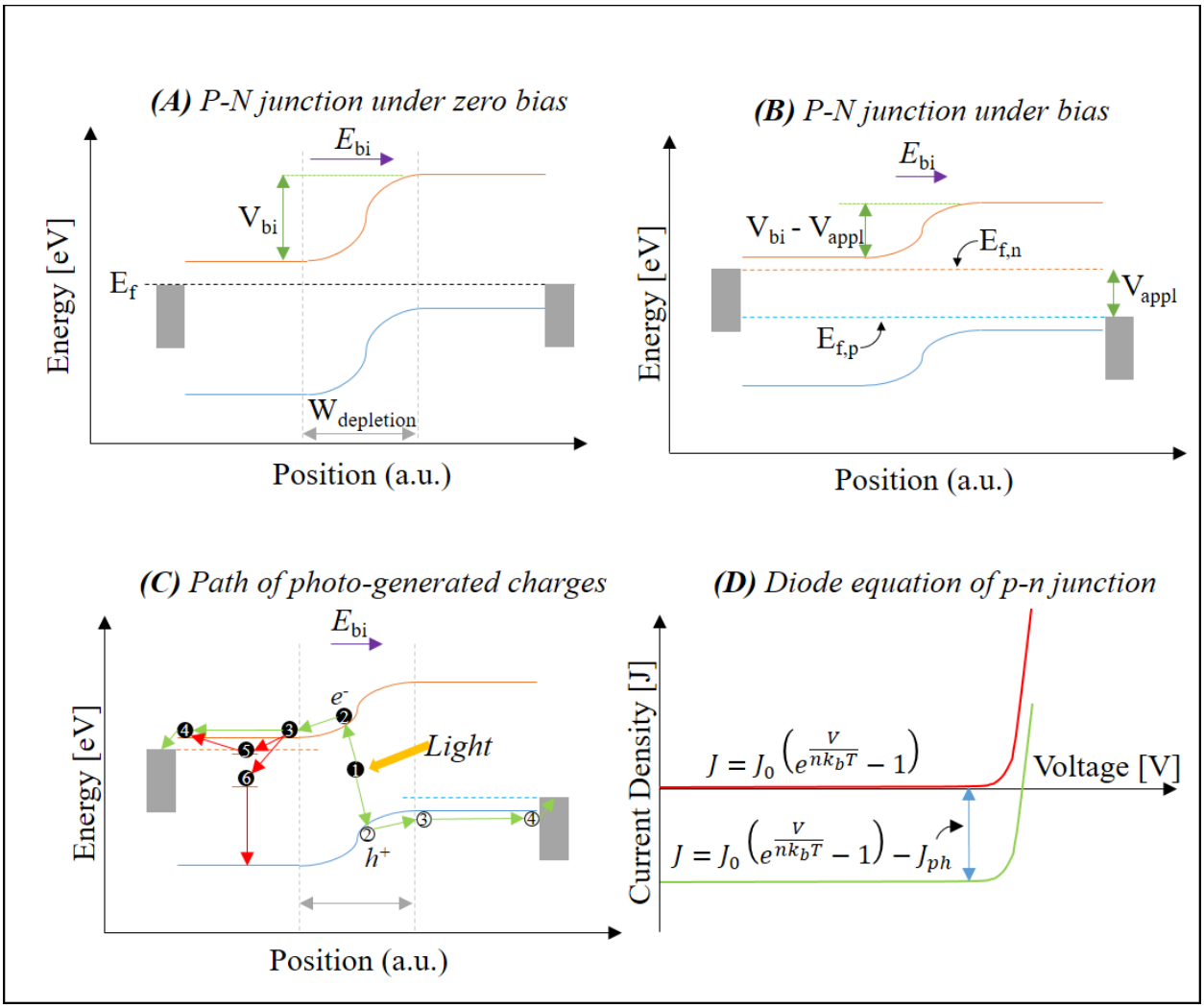


Figure 1.2 – (A) Band structure of a pn junction under zero bias showing the built-in voltage V_{bi}, Depletion region W, and direction of the electric field created by the depletion region E_{bi}. (B) band structure of a pn junction under forward bias. An applied voltage reduces the built-in voltage and creates two quasi-fermi levels, one for holes and one for electrons. (C) an illustrative path of photo-generated charges through a pn junction. Light excited an exciton (1) which dissociates in the depletion region into an electron (2, black) and hole (2, white). These charges are then forced out of the depletion region by the built-in electric field and collected by the electrodes (3-4). Trap states can slow the movement of charges to the electrodes (5) or cause them to recombine (6) depending on their depth with respect to the band gap. (D) diode curves of a pn junction in darkness (red) and under illumination (green). Adapted with permission from [23].

We can extract several key parameters from the relation of current to voltage in the diode equation to determine the performance of the solar cell, beyond simply the J_{sc} and V_{oc}. A power curve for the cell can be calculated by multiplying each voltage with its corresponding current. This will show an applied bias at which the maximum amount of power can be extracted, known as the maximum power point. The fill factor is a measure of how close the voltage and current at the

maximum power point are to their respective open and closed circuit counterpoints, the maximum possible values for the device. A good fill factor will therefore show the "square-ness" of the diode curve, with the theoretical maximum being 86%. Its reliance on material quality can be conceptualized by two forms of resistance within the cell. Series resistance is the resistance charges meet in series whilst travelling through the cell as expected. This is a sum of the internal resistances intrinsic in the materials and device interfaces like the external contacts. A high series resistance will negatively affect device performance. The shunt resistance is a measure of how many charges are moving through the cell along paths other than through the p-n junction. These can be caused by manufacturing defects such as shorts across layers of the solar cell. High shunt resistance indicates that charges will favour travelling through the p-n junction as opposed to alternative pathways, while low shunt resistances indicate that the alternative pathways are easier to travel through. The effect of shunt resistance becomes pronounced at low illumination levels, as there are fewer photo-generated charges and thus a higher percentage will take shunt recombination paths. The two resistances can be combined into the diode equation to give the equation:

$$J = J_0\left(e^{\frac{qV-JR_{se}}{nk_bT}} - 1\right) - J_{ph} + \frac{V+JR_{se}}{R_{sh}} \qquad \text{Eq. (11)}$$

Where R_{se} is the series resistance and R_{sh} is the shunt resistance. Due to current density being on both sides of the equation, this full description can only be solved numerically. The resulting effects of the series and shunt resistances on the diode curve are shown in Figure 1.3:

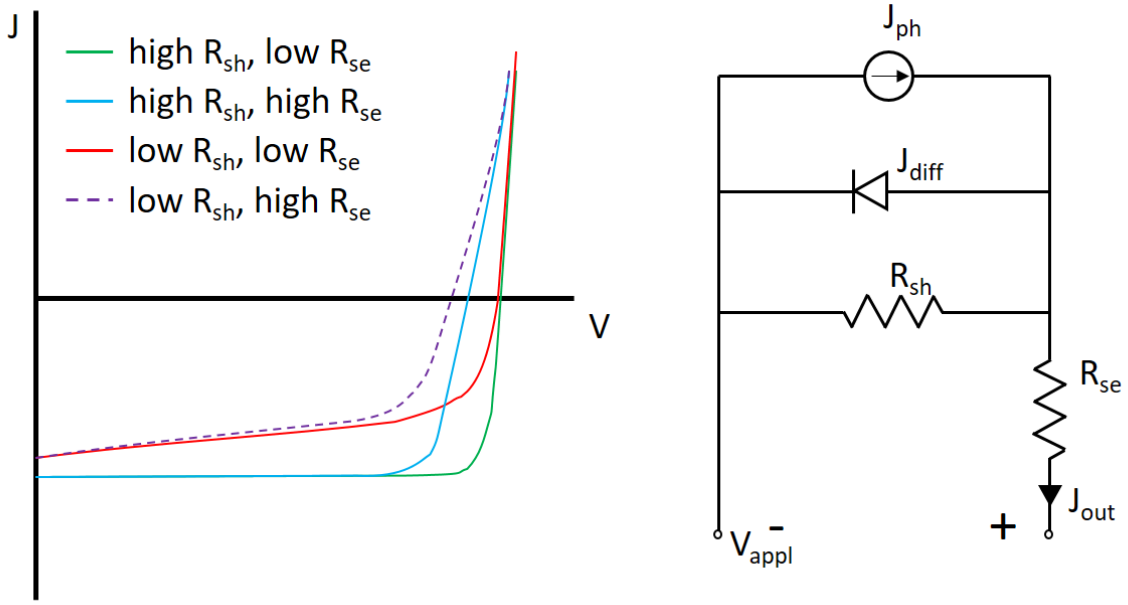


Figure 1.3 – Left: effects of high series and low shunt resistance on solar cells. Right: an equivalent circuit of a solar cell, showing the role series and shunt resistances play.

The total efficiency of the solar cell can be calculated by comparing the current and voltage at the maximum power point of the cell (I_{mp} and V_{mp} respectively) to the power of the incident light (P_{in}), in the following equation:

$$\eta = \frac{I_{mp}V_{mp}}{P_{in}} \qquad \text{Eq. (12)}$$

1.2.4 Mobility, Lifetime, and Recombination

Creating an efficient solar cell requires balancing the absorption of light to generate charges with the ability to extract those charges from the cell. A thick solar cell can absorb more incident light, but too thick a material will mean charges cannot be efficiently extracted. This is to do with how far a charge can travel in a material once excited. The mobility μ of a charge is the speed at which it can travel through a material. Combining the mobility and lifetime τ of a charge in an electric field E gives the drift length:

$$L_{drift} = \tau E \mu \qquad \text{Eq. (13)}$$

This is in contrast to the diffusion length, which is related to the mobility via the Einstein equation:

$$L_{diff} = \sqrt{\frac{\mu k_B T}{q}\tau} \qquad \text{Eq. (14)}$$

As charge transport is more efficient under a drift regime, one approach to a better cell is to increase the width of the depletion region. This extends the built-in electric field and therefore L_{drift}, increasing their likelihood of extraction before recombination. More general approaches to improving the cell involve increasing the mobility or the lifetime. Improving the mobility is closely related to the mechanism by which charges move through the cell, known as charge transport. This will be discussed in depth in section 1.4, in specific relation to quantum dots.

A key approach to maximizing the lifetime is to minimize recombination pathways for excited charges. Recombination refers to the relaxation of an electron from the conduction band back to the valence band, which can happen through a number of pathways [24]. During radiative recombination, the electron releases its energy as a photon. The charge carrier can also give its energy to another carrier in the same band, which then thermally relaxes back to the band edge. Interactions of this type are known as Auger recombination. When a charge carrier relaxes via a mid-gap energy level it is described as Shockley-Read-Hall recombination. The energy level could be introduced in a number of ways such as through the addition of an impurity in the material, a dislocation in the material lattice, or an unpassivated bond on the material's surface.

1.2.5 Limits of Photovoltaic Efficiency

The Queisser limit is the maximum theoretical efficiency of a single junction photovoltaic cell under standard terrestrial conditions [25]. It changes depending on the band gap of the material, as shown in Figure 1.4 [26]. The Queisser limit is based on the interactions of competing loss pathways and is dependent on two key assumptions: each photon incident on the cell is capable of producing only one charge carrier, and charge carriers relax to the band edges.

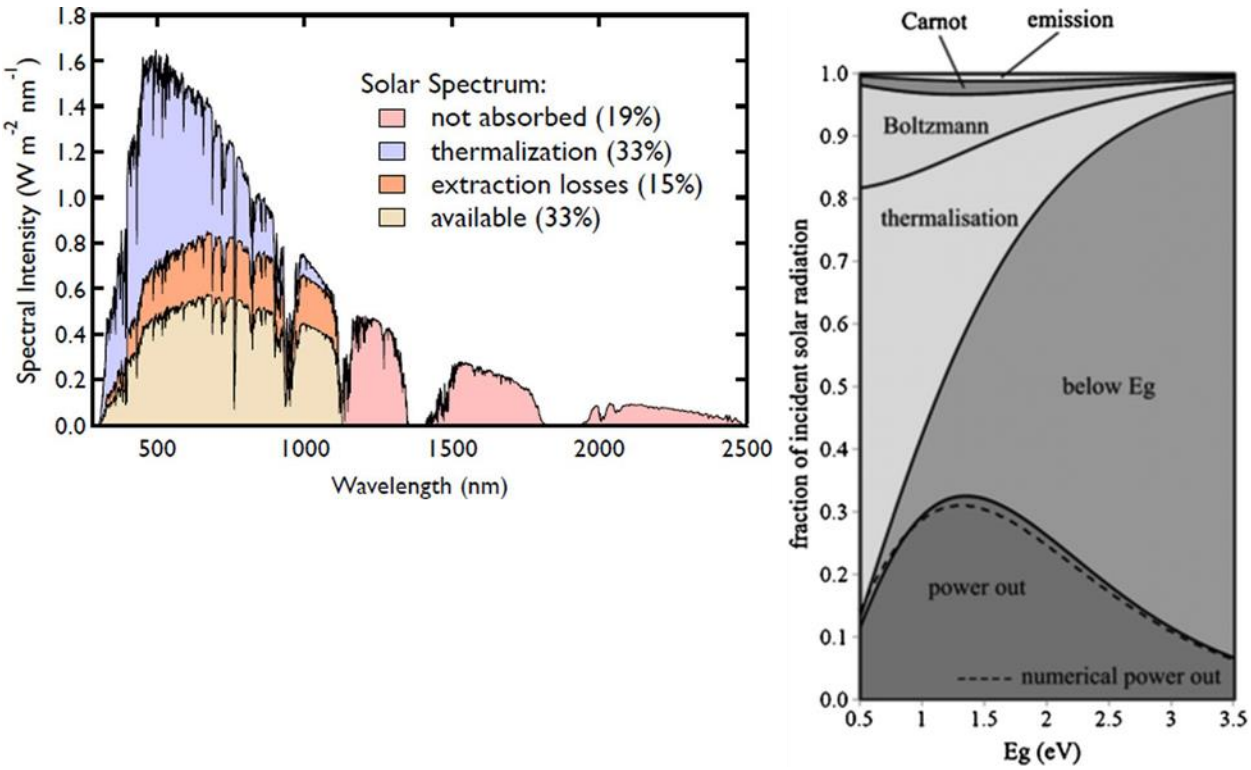


Figure 1.4 - Visualization of the Queisser Limit with respect to the AM1.5 spectrum for a single junction cell of a specific band gap. Reprinted with permission from Rao et al, 2017. b) Graph showing the change in losses associated with the Queisser Limit as a function of the single-junction cell's band gap. Reprinted with permission from Nelson et al.

1.3 Key Quantum Dot and Organic Semiconductor Concepts

With a solid understanding of the physics behind solar cells, the attention of this introductory chapter now turns to the materials they are made of. As mentioned in Section 1.2, photovoltaics cells are made using semiconductors, materials with a gap between their conduction and valence bands. Semiconductors can be made from many different kinds of materials, the main focus of this thesis being semiconducting quantum dot films. This section will explain the origin of quantum dots, how their affects their properties, and the basics of solar cell design using quantum dots as a photoactive material.

1.3.1 Semiconductors and Quantum Dots

An electron can be described as both a particle and a wave. The relation between these two different descriptions is summarized in the equation for the De Broglie wavelength, which relates the momentum of a particle p to its wavelength λ by way of *h*, the Planck constant:

$$\lambda = \frac{h}{p} = \frac{h}{mv} \qquad \text{Eq. (15)}$$

Defining the position of the electron when referring to it as a wave is complex, but necessary to understand its interactions with regards to quantum mechanics. This is achieved by solving the Schrödinger equation for the particle in free space, shown below in one dimension:

$$\frac{-\hbar^2}{2m}\frac{\partial^2 \Psi}{\partial x^2} = i\hbar\frac{\partial \Psi}{\partial t} \qquad \text{Eq. (16)}$$

Where $\hbar$ is the reduced Planck constant (h/2π), *m* is the mass of the particle, *i* is the imaginary component, and $\Psi(x,t)$ is the wavefunction for the particle describing the environment with respect to time and position.

When an electron is constrained by the coulombic interaction with an atom, the interaction can be conceptualized as the "particle in a box" thought experiment. Here, the coulombic interaction of the atom and electron creates a potential well which the electron resides in, bound by potential barriers. Within the box, the electron must have a continuous wavefunction, and the wavefunction outside of the box must reduce to zero exponentially. As a result, the electron's wavefunction is limited to a discrete number of solutions as the space in which the electron can reside is confined, shown in Figure 1.5.

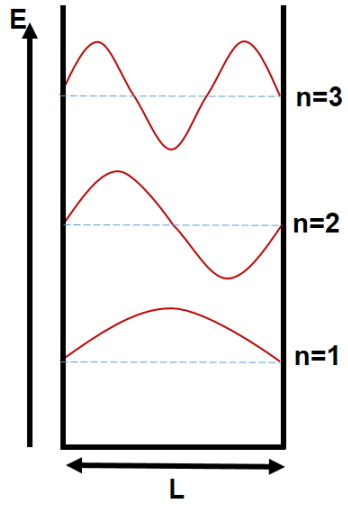


Figure 1.5 - The discrete energy levels of a particle in a box arise due to the wavefunction of the particle being continuous in the box and zero outside the box.

One property of these solutions is that electrons can only have certain discrete energies within this system, known as atomic orbitals. When bound by a proton, the lowest of these discrete energy levels is known as the Bohr radius, the minimum distance an electron can be from the proton. This can be defined through a series of fundamental constants: ε_0 the permittivity of free space, $\hbar$ the reduced Planck constant, m_e the electron rest mass, and e the fundamental charge of an electron. This is expressed as a_0, the Bohr radius.

$$a_0 = \frac{4\pi\varepsilon_0\hbar^2}{m_e e^2} = 5.2918 \times 10^{-11} m = 0.0529 nm \qquad \text{Eq. (17)}$$

When a sufficient number of "particles in a box" are brought into the same system, such as the repeating series of atoms in a bulk semiconductor lattice, energy levels of identical boxes separate due to the Pauli Exclusion Principle. This leads to a distribution of energy states per unit volume, known as the "density of states". These states are then filled with electrons according the Pauli Exclusion Principle, staring at the lowest available energy. The energy of all the electrons in a material can be statistically described by the Fermi level. In conductors, this Fermi level lies inside a band, allowing the material to conduct electrical charge easily. The Fermi level of semiconductors resides in a band gap, allowing them to conduct electrical charge only under

specific circumstances. An electron "excited" across this gap will leave behind a "hole" at the energy level it was at previously, which is also capable of transporting charge. These two charges are bound together and known as an exciton. As the exciton has an effective mass and the material has its own permittivity, the Bohr radius of the exciton can be calculated, and can be up to nanometre length scales in materials such as lead sulfide.

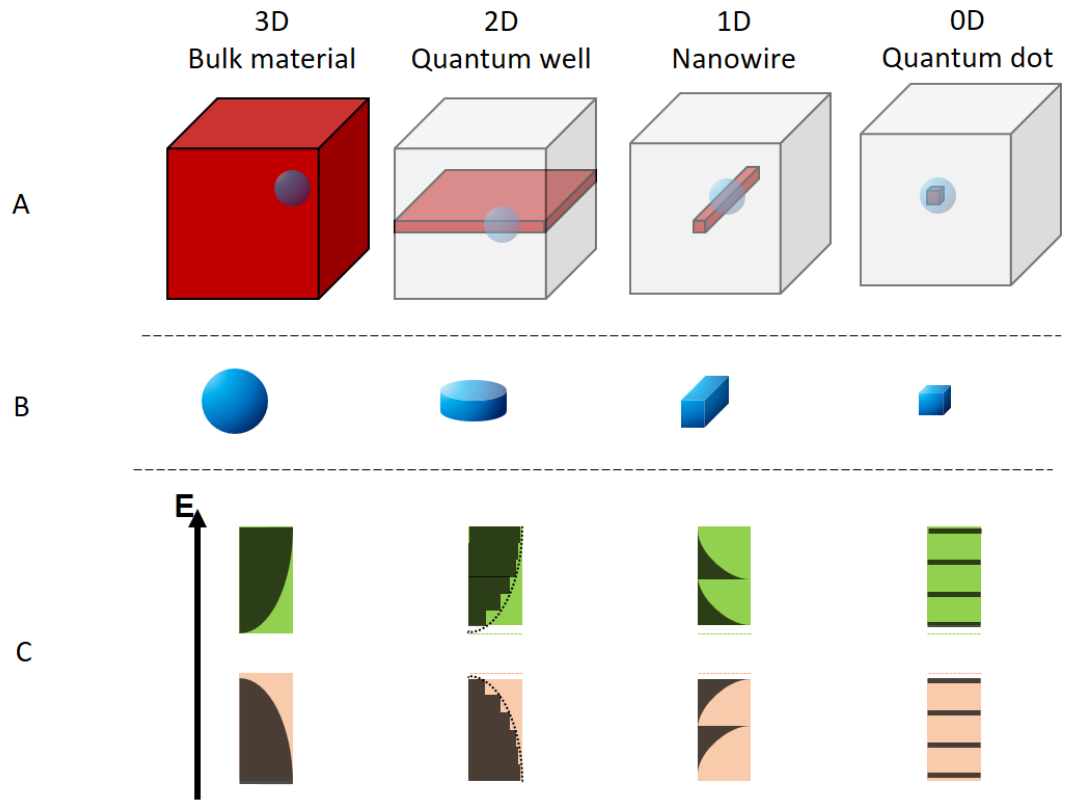


Figure 1.6 – Effect of quantum confinement on the density of states in a material. As a material is confined in more dimensions (A, left to right), the Bohr radius is also confined (B, left to right). This confinement changes the available number of energy states in the material, leading the change in shape of the density of states (C, left to right).

When the dimension of a material is reduced to a length comparable to twice the material's exciton Bohr radius, charge carriers will be confined in that dimension. A result of this confinement is that the density of states changes in distribution on increasing levels of confinement, as atoms providing the energy states are removed to reduce the material's dimensions. At quantum dot

length scales, this leads to discrete, quantized energy levels similar to the particle in a box. Effectively, the quantum dot acts as its own particle-in-a-box confinement for the charge carrier, with box length *L* defined by the diameter of the dot.

1.3.2 Quantum dot band position control

One result of the quantum confinement in quantum dots is precise control over the material's band structure. It is possible to change a film's band gap, fermi, band positions relative to the vacuum level, and fermi level relative to the valence band through control over different materials. Band gap size can be controlled through the physical size of the quantum dots [28], [29]. The position of the fermi level relative to the valence band is a phenomenon known as doping. There are several methods by which the doping of a quantum dot can be controlled, as detailed by Stavrinadis [30]. When the stoichiometry, or ratio of atoms in the quantum dot, differs from the ideal bulk material more or fewer electrons will be present, shifting the fermi level closer to the conduction or valence bands, respectively [31], [32]. Oxidation of the quantum dot surface will also introduce new energy levels close to the valence band, bringing the fermi level closer to the valence band and forming a p-type material [33]. As a result, controlling the level of oxidation can tune the p-doping of a quantum dot thin film. The effect can be enhanced or reduced by the use of ligands, ions or molecules that coordinate to the surface of a quantum dot. Upon coordination with the quantum dot surface, the dipole moment of the ligand will pull charges towards or away from the quantum dot, shifting the band positions relative to the vacuum level. A comprehensive review of research into ligand coordination for improved solar cell performance is found in section 2.4. While considerably more challenging than their common use in bulk semiconductor doping, heterovalent impurities can be added to quantum dots through ion exchange mechanisms [34]. For lead chalcogenide quantum dots, this method of doping has been demonstrated using Ag^{+} and Bi^{3+}

atoms for n- and p-type doping, respectively [35], [36]. Finally, remote doping of quantum dots is realized by injecting charges from a nearby material into the quantum dot, raising the fermi level towards the conduction band[30], [37]. Common materials for this form of doping are molecules such as ferrocene or cobaltocene derivatives [38], electrodes or electrolytes in electrochemical cells [39], metallic nanoparticles [40], or wide-bandgap semiconductor nanocrystals such as zinc oxide [41].

1.3.3 Quantum Dot solar cell design

Broadly speaking, quantum dot solar cells are designed under the same principles outlined in section 1.2: two semiconducting materials with offset band gaps are brought together, and a space-charge depletion region is formed between them. This is then contacted on either side by a charge conductor to produce the working cell. There are several different combinations of band offsets quantum dots are capable of, leading to a wide variety of device architectures illustrated in Figure 1.7.

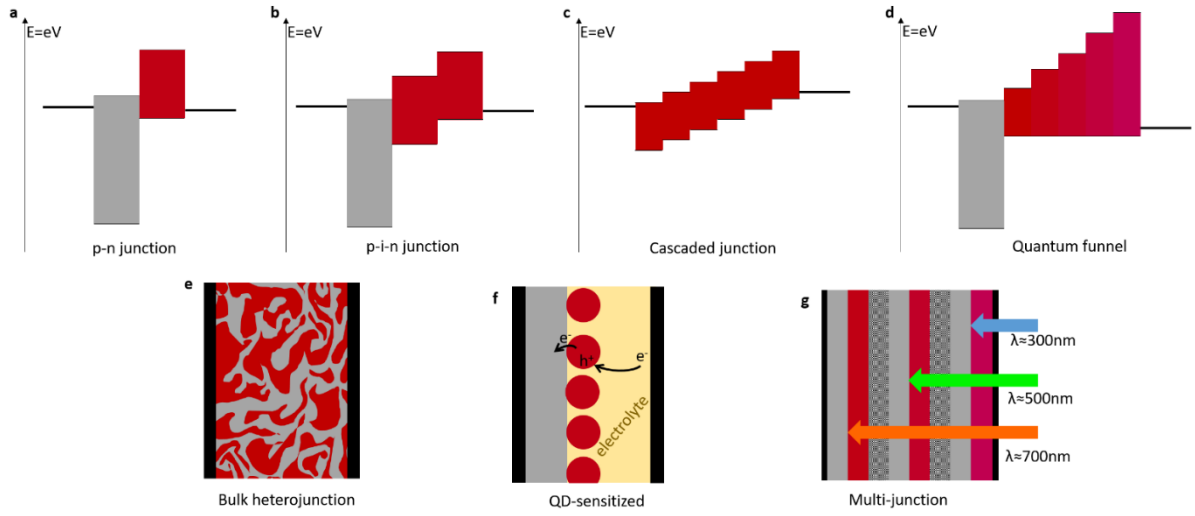


Figure 1.7 - Representation of a) p-n junction, b) p-i-n junction, c) cascaded junction and d) quantum funnel band positions. Band gaps have been colored red for p-type and i-type materials, n-type material band gaps have been colored grey. Color shift in quantum funnel band gaps represents the increasing band gap size. Other uses of quantum dots are e) bulk heterojunction, f) QD-sensitized and g) multi-junction tandem cells.

Quantum dot photovoltaic research has been predominantly focused on the deposition of quantum dot thin-films in layers to build photovoltaic devices, primarily using lead sulfide (PbS) quantum dots and metal oxide nanoparticles in a p-n junction formation[42]–[44]. Here, the PbS is used as the p-type material due to its higher fermi level and conduction band relative to the metal oxide, which in turn has a much deeper valence band relative to the quantum dot layer. The configuration leads to extreme band-bending when the junction forms, leading to the p-n behavior. Careful consideration of the metal oxide n-type material is critical to device performance; metal oxides of zinc, tin, or titanium garner the most research attention [45]–[50]. The p-i-n junction is a common variant of the p-n junction. Here, the p- and n-type regions are separated by a thicker light absorbing layer with intermediate band positions. Due to its intermediary nature, this absorber layer is placed fully within the depletion region of the p- and n-type junction, effectively extending the width of the junction[51], [52]. Another way of contextualizing this device architecture is the use of electron and hole blocking layers. The absorber layer generates the exciton, and charges are prevented from travelling to the wrong contact by way of an energetic barrier, the transport layers. In these kinds of devices, optimization of both the material and the layer thicknesses in relation to one another are key [53], [54].

The concept of charge-blocking layers in p-i-n junctions through band engineering can be expanded beyond three layers, to create cascaded junction devices. This architecture employs multiple layers of semiconductor materials of nearly identical band gaps arranged from highest to lowest valence band position [55], [56]. This provides a gradual but constant electric field pushing dissociated charges to their respective collection electrodes. This architecture is unique to quantum dots due to the precise tuning of quantum dot band positions due to ligand dipole effects [55]–[57]. A variant of the cascaded junction is the quantum funneling device. By varying the size of the

quantum dots in each successive layer, and therefore the band gap, devices can be used to funnel specific charges towards an acceptor [58]–[60].

Because charges separate across material interfaces, the surface area of that interface becomes a critical parameter in the design of the solar cell. Nano-structuring of the system dramatically improves the surface area of different layers. Subtractive patterning uses a removable scaffold, to create a micro- or nanoscale structure which is later removed thermally or chemically [61], [62]. Additive patterning involves the growth of patterned structures directly, often using either preferential crystal grain growth or molecular interactions [63]–[66].This is taken to an extreme by the concept of a bulk heterojunction device. In this system, n- and p-type materials are blended together and cast as one film, forming a highly disordered region as phase separation occurs between the materials that dramatically increases the junction area [67]. The increased junction area increases the size of the depletion region in the device and allows for a thicker absorber layer, which improves the conversion of light into excited charges. However, the complex mix of phases can lead to a lower mean free path for charges as a result of frequent recombination within the cell [63], [66].

The high surface area requirements for p-n junctions can also be exploited through the use of quantum dot sensitization. Here the surface of a scaffold material, typically a wide-bandgap semiconductor like titanium dioxide (TiO_2), is coated in quantum dots to improve the material's ability to absorb of photons. When the quantum dot absorbs a photon that would otherwise not be absorbed by the scaffold, the exciton is immediately dissociated by the band alignment and built-in electric field between the quantum dot and scaffold material. Charge balance is restored to the dot through an electrolyte, which can take the form of an organic polymer or a liquid electrolyte[68]–[73].

As shown in discussion of the Queisser limit, a single band gap cannot efficiently convert the entire solar spectrum due to sub-bandgap and thermalization losses. By combining multiple band gaps within the same device, it is possible to surpass the single-junction Queisser limit. Tandem cells are the simplest approach to doing this. Tandem cells have two or more separate junctions with different band gaps arranged in a stack by sequentially decreasing band. Sub-bandgap light passing through one cell is absorbed by the cell below it in the stack. The control over band gap size and position makes quantum dots especially attractive for use in tandem solar cells, particularly with respect to their infrared absorption in conjunction with silicon or perovskite cells [74]–[76]. Intermediate band gap solar cells are an attempt to create a mid-gap state capable of absorbing lower energy light, effectively creating a tandem cell within a single junction[77]. This enables an increased photocurrent without the associated decrease in voltage across the device [78]. Quantum dots have been singled out as a viable absorber material due to the possibility of combining dots of differing size in the same absorber layer [79], [80].

1.4 Charge Transport in and Transfer between Semiconductors

Improvements to solar cell efficiency can be aided by an understanding of the movement of charges through a material. By examining the mechanisms of how electrons and holes move through a material, bottlenecks to optimized transport can be removed, leading to improved device performance. Charges in a quantum dot solar cell must move between quantum dots to be collected by the electrode, with different and overlapping mechanisms each dominating different length scales. As the aim of this thesis research is to improve charge transport properties in quantum dot thin films by using an organic semiconductor, discussion of charge transport methods in these materials are also important, as well as the transfer of charge between quantum dots and organic semiconductors.

1.4.1 Charge Transport in bulk semiconductors

As previously stated, a crystalline inorganic semiconductor is composed of a large number of repeating atoms, which can be modelled as near-infinite. This forms a periodic arrangement of the electron potential wells discussed in section 1.3.1, giving rise to the density of states distribution in three dimensions. Charges can be transported by moving between available energy states that are energetically similar. This happens in the conduction band, which becomes partly filled upon the excitation of one or more electrons from the valence band. Each excitation also leaves behind a hole in the conduction band. Additionally, radiative transfer can occur where an atom in an excited energy state relaxes and produces a photon, which is absorbed and excites an electron on the acceptor atom to a higher state. The highly ordered, repeating pattern of potential wells also results in the wavefunction of confined particles overlapping, across adjacent potential wells. These waves, known as Bloch waves, spread throughout the material and provide another form of charge transport, with high charge mobility.

1.4.2 Charge Transport in Quantum Dot Semiconductors

A quantum dot thin film is composed of a series of 0D confined semiconductors, each with a discrete density of states. These densities of states will overlap, forming a Gaussian distribution of discrete energy states. In an ideal scenario, all quantum dots in the thin film would be identical in size and shape, arranged in a repeating lattice similar to atoms in a crystalline bulk inorganic semiconductor[81], [82]. This would allow for the overlapping wavefunctions of the quantum dots to form extended band-like states similar to Bloch waves [83], [84]. However, a real system will typically have quantum dots of different sizes arranged in a disordered fashion. Additionally, poor control over the surface chemistry of the quantum dots can lead to isolated energy levels within

the band gap, known as trap states. This inhibits the formation of the band-like states as individual quantum dot wavefunctions no longer overlap favorably.

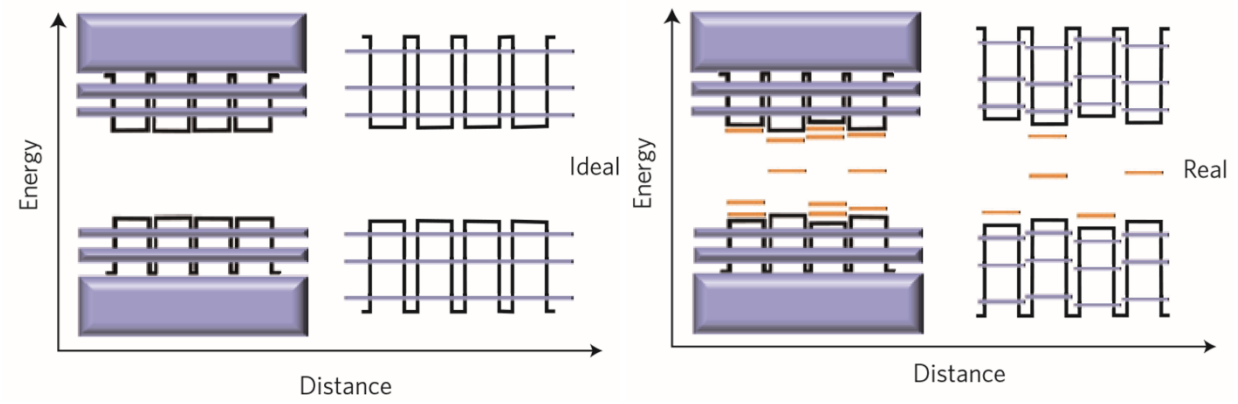


Figure 1.8 – Left: an ideal quantum dot crystalline film results in the overlap of quantum dot wavefunctions (black) forming extended band-like states (purple). Right: size dispersity, poor packing structure, and poor passivation of trap states (orange) leads to a loss of wave function overlap. Reprinted with permission from Kagan, C., Murray, C. Charge transport in strongly coupled quantum dot solids. Nature Nanotech 10, 1013–1026 (2015).

In the absence of these overlapping wavefunctions, charges move by tunneling to the nearest available energy level in the Gaussian distribution of states. This process is known as incoherent hopping. The rate at which this process happens ($k^{(a)}$ where a is +/- depending on the charge) is spontaneous if the energy level the charge moves to (ε_j) is lower than the energy level it hops from (ε_i). The probability of hopping to a higher energy level, k_{ji} is dependent on the temperature, T, of the system, is shown in equation 18 [85]:

$$k_{ji}^{(a)} = k^{(a)} \, exp\left(-\frac{(\varepsilon_j - \varepsilon_i)/2}{k_b T}\right); \; \varepsilon_j > \varepsilon_i \qquad \text{Eq. (18 a)}$$

$$k_{ji}^{(a)} = k^{(a)} \qquad ; \; \varepsilon_j \leq \varepsilon_i \qquad \text{Eq. (18 b)}$$

Where $k^{(a)}$ is the phenomenological base rate of a free charge carrier and k_b is the Boltzmann constant. This incoherent hopping happens at small length scales due to the probability of finding

a charge carrier outside its potential well decaying exponentially with distance.

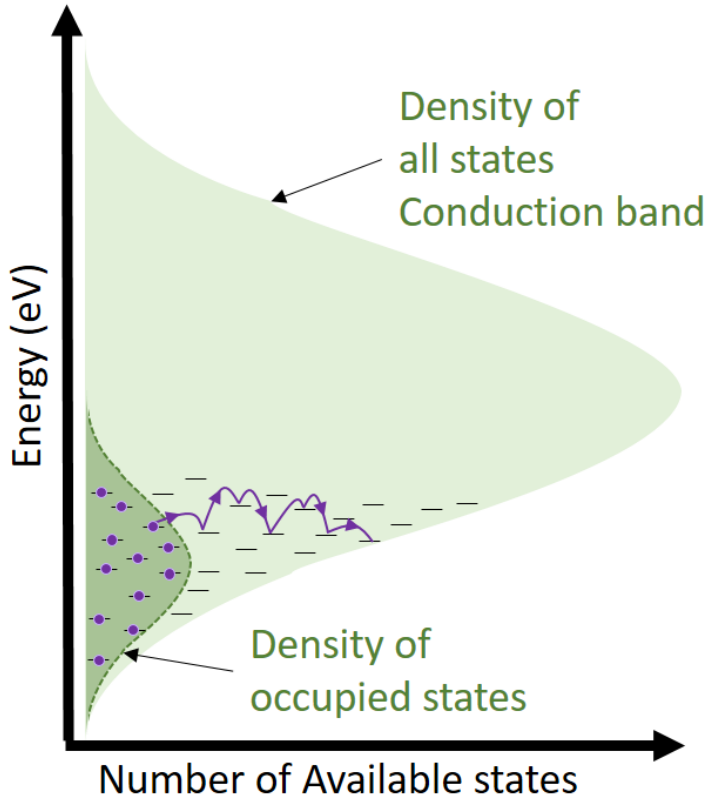


Figure 1.9 – Gaussian Density of Sates (DoS) in the conduction band of a quantum dot thin film (light green). Electrons (purple circles) populate a given number of occupied states within the conduction band (dark green) populating the band can move to nearby unoccupied energy levels (black lines) by randomly hopping (purple arrows). Adapted from Baranovskii et al. [86].

Charges will not necessarily jump to the nearest available energy state, giving rise to the concept of Variable Range Hopping (VRH). The relationship between conductance G and temperature T varies according to the relation [87]:

$$G \propto e^{(-B/T^{\frac{1}{v}})} \qquad \text{Eq. (19)}$$

where B is the critical temperature and v is an integer dependent on the temperature. At low temperatures, coulombic interactions give to Efros-Shklovskii regime where $v = 2$. Above a critical temperature however, this coulombic barrier can be ignored and the VRH changes to a Mott regime, where $v = 4$. This critical temperature can be determined by:

$$B = \frac{e^4 a g_0}{k_B(\varepsilon\varepsilon_0)^2} \qquad \text{Eq. (20)}$$

where k_B is the Boltzmann constant, ε and ε_0 are the permittivity of the material and free space, respectively, g_0 is the density of states for the material, a is the localization length, and e is the elementary charge constant [88].

At slightly larger length scales, Dexter Energy Transfer is observed. Dexter Energy Transfer involves the direct exchange of electrons in different energy states [89]. An electron in an excited state of a donor is exchanged with an electron in the ground state of an acceptor. After the exchange, the acceptor now has the excited state electron while the donor has only ground-state electrons. The excited electron will hop from the donor to the acceptor, with a ground-state electron of the same spin moving in the opposite direction. The rate of charge transfer is governed by the equation:

$$k_{DET} = \frac{2\pi}{\hbar K^2 e^{\frac{-2r_{DA}}{r_D + r_A}}} \int_0^\infty F_d(\omega) G_A(\omega)\, \partial\omega \qquad \text{Eq. (21)}$$

where r_{DA} is the distance between the donor and acceptor, r_D and r_A are the Van der Waals radii of the donor and acceptor, K is a constant related to the energy of the system, and $\hbar$ is the reduced Planck constant. The integral gives the spectral overlap of the donor emission $F_D(\omega)$ and the acceptor absorption $G_A(\omega)$. The exponential dependence results in Dexter energy transfer working only over short distances, with the rate rapidly dropping off above 1 nm separation between donor and acceptor. [90].

Förster Resonance Energy Transfer (FRET) arises from the relation between the dipoles of a donor and acceptor species [91]. Photoexcitation induces an oscillating dipole in the energy donor. This in turn can induce an oscillating dipole in an energy acceptor [92]. To preserve the conservation of momentum, any increase in the oscillation amplitude by the acceptor causes a corresponding

decrease in the donor, until the energy state has been transferred and the acceptor has an excited electron instead of the donor [93], [94]. The rate of transfer is dependent on the distance between donor and acceptor *d*, the radiative lifetime of the donor τ_r, the spatial orientation of donor and acceptor relative to each other κ, and the spectral overlap of the donor and acceptor [92], [95]:

$$R_{ET} = \frac{9c^4\kappa^2}{8\pi n^4 \tau_r} \cdot \frac{1}{d^6} \cdot \int_0^\infty \frac{f_D(\omega)\sigma_A(\omega)}{\omega^4} \partial\omega \qquad \text{Eq. (22)}$$

where *c* is the speed of light and *n* is the refractive index of the medium hosting donor and acceptor. The integral gives the spectral overlap of the fluorescence spectrum of the donor f_D and the absorption spectrum of the acceptor σ_A across all wavelengths ω. The most important FRET variable is the relationship to distance, which allows for energy transfer at greater length scales than Dexter energy transfer. However, the overall length scale of these is still short, in the range of 1-100 nm donor-acceptor distance.

Beyond this distance, the dipole interactions between donor and acceptor no longer happen simultaneously. Instead, radiative transfer occurs when an exciton recombines in the donor and emits a photon, which is then reabsorbed by the acceptor to produce another exciton. Energy is lost during this process, as the excitation process in the acceptor quantum dot will be affected by carrier cooling effects. The probability of this phenomenon occurring is dependent on the overlap of the donor quantum dot's emission and the acceptor's absorption spectra, as well as the concentration of acceptors in the film and the film thickness.

1.4.3 Charge Transport in Organic Semiconductors

An atom's electrons will form in shells around the atom governed by the Pauli Exclusion Principle. The shape and number of electrons in each shell is governed by the Schrödinger Equation. In the atoms that predominantly form organic compounds, the most common valence shells are the s-orbital, shaped like a sphere, and the p-orbitals, shaped like three dumbbells pointing in different

directions. To achieve a lower overall energy, the s and p orbitals in organic compounds will often combine to form hybridized orbitals, combinations of the s- orbital and either one, two, or all three of the p orbitals - noted as sp, sp_2 and sp_3 hybridization, respectively. In sp- and sp_2- hybridized atoms, orbitals with an s-component exist on the same plane to which remaining p-orbitals lie perpendicular. Overlap of neighbouring p-orbitals results in a delocalized π-bond and a π^* anti-bond to maintain the conservation of energy. A large number of near-identical energy levels from the delocalized π-systems will form a density of states with a highest occupied molecular orbital (HOMO) and lowest unoccupied molecular orbital (LUMO). As the molecules in organic semiconductors are generally disordered, charge transport dynamics in this system can be understood as charges hopping between a large number of discrete energy levels in a Gaussian distribution [96]. Photo-excited charges will thermalize from the high energy levels to the lowest possible energy level, with each carrier having a probability of thermal activation to a higher energy level at temperatures above absolute zero. Where there is an equal probability of thermalization and thermal activation, the charge is said to be at the transport energy E_{tr}, and is the minimum energy at which "band like" transport occurs. If a charge drops below E_{tr}, it is considered immobile until a statistical thermal activation back up to E_{tr} occurs. In this way, transport in organic semiconductors can be described as a "multiple trap and release" or MTR mechanism[96], [97].

The rate of hopping between from state *i* to state *j* can be described by Marcus equation gives the rate of hopping between states v_{ij} as a function of the localization length of the charge carriers α, the spatial distance r_{ij} and energies $\varepsilon_{i,j}$ of states *i* and *j*, the temperature *T*, the transfer integral J_0, and the activation energy E_a as follows [97], [98]:

$$v_{ij} = \frac{J_0^2}{\hbar}\sqrt{\frac{\pi}{4E_a k_B T}}\, exp\left(-\frac{2r_{ij}}{\alpha} - \frac{E_a}{k_B T}\right) \times exp\left(-\frac{\varepsilon_j - \varepsilon_i}{2k_B T} - \frac{(\varepsilon_j - \varepsilon_i)^2}{16 k_b T E_a}\right) \qquad \text{Eq. (23)}$$

where k_B is the Boltzmann constant and $\hbar$ is the reduced Planck constant. The activation energy has been found to be dependent on two factors, the disorder of the system and the polaron activation energy. A polaron is a charge carrier (electron or hole) on a molecule. The net charge of the carrier warps the molecule on which it exists itself, forming a cloud of dipoles on neighbouring molecules called a polarization cloud. This cloud must be accounted for when considering the movement of the carrier [99]. Interestingly, it has been shown by Lu *et al* that the polaron activation energy does not linearly affect the overall mobility of charges in organic semiconductors, with an optimal value of around 0.15 eV giving the highest mobilities [100].

A simpler alternative to the Marcus equation is the Miller-Abrams equation, which uses a different set of parameters. Here, the hopping probability v_{ij} is determined by the energies ε_i and ε_j of states i and j, respectively, and the spatial distance between them r_{ij} as described by the equation [96], [101], [102]:

$$\mathrm{v}_{ij} = \nu_0 \exp(-u) \qquad \text{Eq. (24 a)}$$

$$\text{where } u = 2\gamma r_{ij} + \left\{ \begin{array}{cc} \frac{\varepsilon_j - \varepsilon_i}{k_B T} & \text{for } \varepsilon_j > \varepsilon_i \\ 0 & \text{for } \varepsilon_j \leq \varepsilon_i \end{array} \right\} \qquad \text{Eq. (24 b)}$$

The Miller-Abrams approach introduces the tunnel probability through potential walls, γ, and the attempt-to-escape frequency ν_0, which defines the dynamic of trap emission and maximum rate of de-trapping cycles [103], [104].

1.4.4 Lead-site trap states

As discussed in section 1.1 the lifetime of charges is adversely affected by the rate of recombination in the material, such as Shockley-Reed-Hall (SRH) recombination pathways. In PbS quantum dots, there are three main pathways for SRH recombination: unpassivated surface bonds, surface lattice vacancies, and structural dislocations [105]. Of these, unpassivated lead surface atoms are responsible for the majority of trap states that lead to recombination[106], [107].

It has been shown that there is an increased stoichiometric ratio of lead to sulfur ions on the surfaces of the nanocrystals. While dominant theory and supporting models note that the presence of surface lead as directly unpassivated atoms does not induce trap states, co-ordination with the wrong ligand can lead to in-gap or sub-gap recombination sites [108]. For example, atomic oxygen coordinating to lead surface atoms will produce tap states near the valence band. [109]. Similarly, the presence of hydroxyl groups on the surface of the dot are formed due to incomplete passivation of quantum dot surfaces during ligand exchange and typically form on lead surface atoms [110]. Additionally, unpassivated surfaces are more likely to fuse with neighboring quantum dots, forming dimers. The formation of these dimers creates a new wavefunction for a much larger quantum dot, leading to incomplete overlap of the wavefunctions and an additional mid-gap state [111], [112].

Two different methods have been the focus of research for passivation of these surface lead atoms. The most common method is the development of ligands that can more effectively passivate these trap states. Ligand passivation can be used in concert with synthetic techniques to control the number of lead surface atoms present on the quantum dot, thereby limiting the number of trap states that can form. Increasing the ratio of sulfur precursor in synthesis can alleviate some of the imbalance, but does not directly stop the formation of sensitive lead-rich surfaces[113]. As quantum dots grow, the two dominant surfaces that form are the (001) and (111) lattice planes, the former being an exclusively lead surface. However, hydroxyl groups predominantly form on the (111) plane. Control over this kinetic-thermodynamic tradeoff can dictate the prevalence of (001) surfaces, reducing the number of lead surface atoms [114].

Ligand exchange presents another avenue for the formation of lead-site trap sates, with the number of unpassivated bonds can increasing to triple their original count[111]. These unpassivated bonds

produce energy levels, often in the middle of the band gap or within the conduction or valence bands. An exciton can be "trapped" by these states, use them as recombination sites, or both [115], [116]. As a result, unpassivated bonds lower both the lifetime of the charge carriers and the mean free path, severely reducing the mobility of charges in the cell. As such, a strong understanding of both the types of trap states and the ways to passivate them is crucial in developing high-mobility systems[117].

1.4.5 Charge Transfer between Quantum dots and Organic Semiconductors

Knowledge of the mechanisms of charge transport in sections 1.4.2 and 1.4.3 can be used to understand the ways in which charges transfer between quantum dots and organic semiconductors. This is critical, as improvements in charge transfer rates can improve the short circuit current, open circuit voltage, and fill factor of the final photovoltaic device. [118], [119].

The method of charge transfer depends on the distance between the quantum dot and organic semiconductor, while the direction of charge transfer is dependent on their band alignment [120]. When sufficiently close, Dexter energy transfer pathways have been shown to occur between donor quantum dots and acceptor organic molecules [121]–[123]. However, the majority of reported charge transfer between quantum dots and organic semiconductors proceeds via the Förster resonance energy transfer (FRET) pathway [124], [125]. A system that suppresses recombination will promote dissociation and therefore charge transfer. Thus, charge transfer between organic and inorganic species is largely affected by distance between the donor and acceptor, the density of mid-gap trap states, and band alignment between donor and acceptor [126], [127].

By passivating mid-gap states, ligands can tilt the balance between relaxation and charge transfer pathways towards the latter process [119], [128]. Dipoles in the ligand have also been shown to stabilize charge transfer between quantum dots and other semiconductors, with the imbalanced distribution of charge in the ligand hindering recombination after separation [129], [130]. The effective range of charge transfer pathways remains an important consideration, however, with large, opto-electronically inactive ligands suppressing charge transfer by increasing the distance between donor and acceptor beyond the limits of Dexter or Förster energy transfer [119], [131], [132].

Energy level alignment is another critical aspect of charge transfer between quantum dots and organic semiconductors. Quantum dot size plays a significant role given their size-dependent band gaps and easily modified density of states [132]–[134]. Charges can also be trapped at the interface between donor and acceptor due to improper band alignment [135]. Further, the strong localization of charges, particularly electrons, on quantum dots can make charge transfer pathways less favorable, hindering the movement of charges [133].

Ligands again play a role, as electroactive ligands can introduce energy levels resulting in a favorable band alignment for charge transfer to organic semiconductors [136]. However, ligands can also introduce mid-gap states which can dramatically increase the rate of SRH recombination, suppressing charge transfer [137].

1.5 Mobility and Lifetime of charges

The mobility of quantum dot thin films is dependent on a range of factors and shows surprising independence to the bulk material mobility constraints [117], [138]. This is due to the different charge transport mechanisms suggests that several key factors not present in the bulk material determine the mobility and therefore transport properties of the film.

The idealized quantum dot film is difficult to achieve in practice. While long synthetic ligands keep quantum dots far enough apart to remain stable in a colloidal suspension, they often keep quantum dots too far apart to observe variable range hopping or Dexter Energy Transfer as solid films. This reduces the number of pathways for exciton movement through the film, and leads to a higher rate of exciton recombination. In addition, synthesized quantum dots are not a single monodisperse collection. This adversely affects the packing structure of the quantum dots, as they are not able to form the repeating patterns over large length scales necessary for long range order. Further, the differing sizes of quantum dots in the film makes it much harder for wave functions to overlap as the confinement effects on the excitons differ between neighbors. All of these effects negatively impact the mobility of the film, reducing both the lifetime and the mean free path of charge carriers in the film [139].

2 Literature Review

Having detailed the broad physical concepts behind photovoltaics and quantum dots, the following section turns outward to the vast body of scientific literature. This chapter examines the conception, advancements, and current state of quantum dot photovoltaic research as pertaining to the aims of this thesis. Detailed exploration of the literature provides a strong contextual basis for how the work of this thesis complements recent scientific discoveries and unlocks exciting new potential fields of research. Whilst many compounds exhibit the quantum confinement effects necessary for quantum dot photovoltaic applications, the majority of research has focused on the chemistry of lead sulfide (PbS) quantum dots, including the work presented in this thesis. As such, the majority of literature presented in this section will be related to quantum dots made of lead sulfide and other similar crystal structures such as lead selenide (PbSe), broadly referred to as lead chalcogenides.

First, the synthetic routes to quantum dots are discussed, followed by the different permutations of quantum dot solar cell device structures. This is followed by an in-depth look at the passivation methods for quantum dot solar cells used in literature, focusing on the use of ligands to passivate defects and improve charge mobility, resulting in better photovoltaic device performance. Subsequently, a brief summary of diacetylene polymers and their use in photovoltaic systems will be given. The literature review concludes by placing the aims of the thesis in the context of the discussed body of literature and highlighting the contributions to scientific understanding that will be made.

2.1 Principles of Quantum Dot synthesis

Quantum dots can be made through deposition or colloidal methods [140], [141]. In deposition, precursors are applied directly on to a substrate, forming nanocrystals [142]. This can be done through vapor deposition or electrodeposition techniques [143]. For vapor deposition techniques, conditions such as the flow rate of gases, selective patterning, substrate temperature, and deposition time all play a role in determining the size, shape, and composition of the quantum dots[144], [145]. In electrodeposition, the current, voltage, type, and concentration of the electrolyte all play a role in the eventual size and shape of the nanocrystals [45], [143], [146]–[148]. However, both these deposition methods are more suited to forming quantum dot monolayers and offer little control over the surface chemistry after deposition. As such, vapor deposition and electrodeposition are unsuitable fabrication methods for the work presented in this thesis.

Colloidal synthesis generally involves creating quantum dots in solution from two or more precursor compounds. This method is used to produce the dots in solution or as a powder (after removal of the solvent), which can then be cast on a substrate to form a film. As the quantum dots

are formed prior to deposition, their high surface area can make them unstable outside of an inert environment. To counteract this instability, quantum dot surfaces are coated to improve stability in colloidal systems. This can either be a thin shell of an inert material, or a ligand. Ligands are small molecules or atomic ions that coordinate to the unpassivated states present on the quantum dot surface. Cation exchange uses previously formed nanoparticles as a scaffold for the formation of the desired quantum dot by swapping metal cations in solution with those in the nanoparticle scaffold. The scaffold is then dissolved after a desired size is reached [149], [150]. Hot injection synthesis of II-VI chalcogenides proceeds by combining two separately prepared reaction precursors. The metal precursor is usually made by mixing the metal oxide, acetate, or halide with a long-chain ligand such as oleic acid or oleylamine to form a new metal complex [29], [151], [152]. Group VI precursors vary widely, with their toxicity and reactivity playing central roles in their eventual use. Common examples include hexamethyldisilathiane, thiourea, and elemental sulfur[153]–[155]. For PbS quantum dots, the method in which the sulfur precursor is prepared can also have a profound impact on the shape of the nanocrystal [154].

The reagents are then rapidly combined, usually at elevated temperature, to produce a maximum number of nucleation points from which the nanocrystals can grow[29], [152], [156]. Nanoparticle growth can follow a thermodynamic or kinetic approach, depending on the temperature[114]. Nanocrystal growth will proceed as long as the reaction mixture remains above a certain temperature, without the formation of new nucleation points[151], [157]. The long-chain stabilizing ligands from the metal precursor ensure the dots do not aggregate whilst forming and remain attached to the nanocrystals after their formation, stabilizing them in solution[29]. Once the desired size has been reached, the reaction can then be quenched by rapidly lowering the temperature and concentration of reagents. This is usually achieved by cooling the reaction flask

or quenching the reaction in a cold solvent [29], [152], [158]. Additional stabilizing ligands can also be added to improve the degree of surface passivation, a key concept explored later in this review [159]. This “hot injection” method can happen at a variety of temperatures, with hotter reactions leading to larger nanocrystals [155]. In the absence of temperature variance, quantum dot size and polydispersity can also be changed by varying the ratios of the reagents relative to each other [160]. Reaction time, reagent concentration, and even length of the stabilizing ligand can also play a role in the final synthetic outcome [153].

2.2 Improving Quantum Dot Solar Cell Performance

This section will show how the bottlenecks to charge transport and transfer discussed in section 1.4 have been minimized, improving device performance over time. Control over the trap states, packing structure, and proximity of quantum dots is vital to the optimization of photovoltaic devices [161], [162]. As much of this is dictated by surface effects, effective passivation of the quantum dot surfaces is critical to controlling charge transport in the quantum dot film. This can be achieved in two ways: core-shell passivation and ligand passivation. Passivation via ligands has generally proceeded through either or both of two main approaches. The first approach is accurate and complete passivation, which aims to minimize the interdot distances within films. This uses short chain optically inactive ligands to reduce steric hindrance on the surface of the quantum dots, thus maximizing ligand coverage and trap site passivation. The second approach focuses on improving the electronic structure around the quantum dots by incorporating an opto-electronically active ligand into the film, providing alternative pathways for charge transport.

Discussion begins by looking at the upper branch in Figure 2.1, giving a brief summary of core-shell methods to offer a more in-depth examination of ligand passivation [163], [164]. The review then looks at the lower branch of Figure 2.1 and the passivation of the surface with ligands. This

branch itself can be split into two themes, and this review will start by examining approaches to short organic ligands meant for effective surface passivation, culminating in the record efficiency photovoltaic. From here, the review follows the final branch of Figure 2.1, the approach of π-conjugated ligands that directly participate in the charge transport properties of the material to improve the electronic landscape in quantum dot thin films. The new science presented in this thesis takes the approach of this last branch to improving efficiency of quantum dot solar cells.

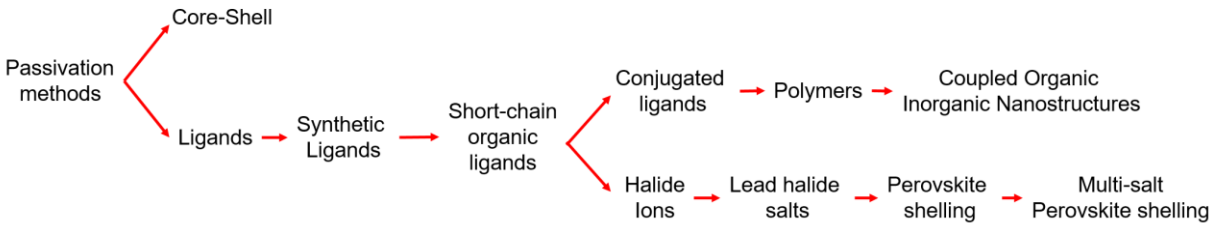


Figure 2.1 - Guide to the literature review of quantum dot surface.

2.3 Core-Shell Passivation

Coating the nanoparticle in a second material passivates bonds on the surface of the nanoparticle, this is known as core-shell passivation. The core of the nanoparticle maintains its quantum confinement effects, and the shell acts as both a passivating layer and a buffer between dots [163]–[169].

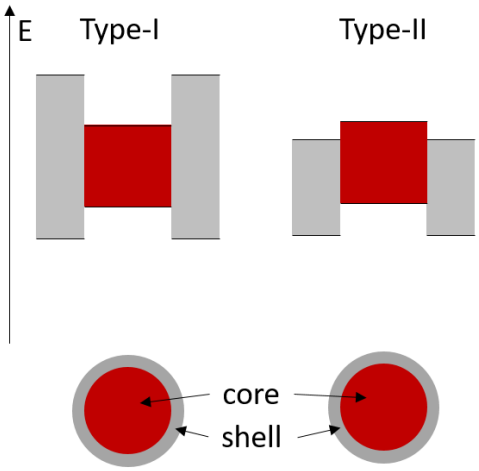


Figure 2.2 – Core shell passivation can have two different kinds of band architectures, type-I and type-II.

There are two key approaches to constructing the core-shell architecture. Cation exchange is a process typically used when creating a shell of the same mineral class, for example PbS/CdS core-shell dots. In this method, surface metal atoms are replaced by cations in solution to form a shell around the now smaller core, as some of the atoms used to comprise the original quantum dot have been replaced and a new material made. Because of this, cation exchange increases the band gap of the quantum dots, making precise control over the process a requirement [170]. Direct growth of the shell material on the surface of the quantum dots allows for a much wider range of shell materials and does not change the size of the core, but challenges persist in growing uniform layers. As the shell material is usually a similar semiconducting material, the band alignment between the core and the shell can give additional properties to this method of passivation that are difficult to obtain in ligand-based passivation systems. These can be broadly categorized into Type-I and Type-II structures, as shown in Figure 2.2. Type-I structures are used due to their ability to effectively passivate surfaces whilst remaining mostly optically inactive, within certain thicknesses of the quantum dot. Type-II core-shell structures have also been shown to increase the rate of exciton dissociation, which is of particular use for photocatalytic purposes and sensitizing agents [80].

2.4 Ligand Passivation

To reiterate from section 1.3.2, Ligands are small molecules or atomic ions that coordinate to the unpassivated states present on the quantum dot surface. The ways in which these ligands bind are governed by metal complexation as noted by Green and summarized in Figure 2.3[171]. There are

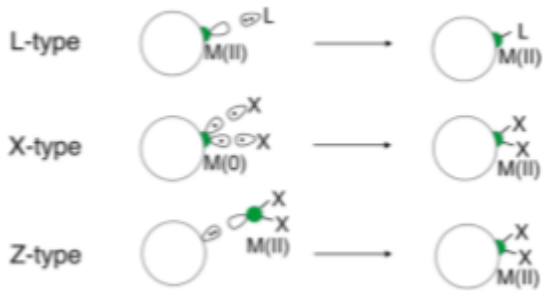


Figure 2.3 - Visual representation of the L-type, X-type, and Z-type ligands and their co-ordination mechanisms to metal surface atoms on quantum dots. Reprinted with permission from Chem. Mater. 2017, 29, 2, 752–761, copyright 2021, American Chemical Society

three key types of ligand binding mechanisms to metal complexes, which Houtepen *et al*. extends to surface metal ions on chalcogenide surfaces [108], [171]. These can be classified based on whether the ligand or the metal provided the electrons. L-type ligands coordinate by forming a dative bond with the metal, donating both electrons. These electrons occupy a shared orbital between the ligand and the metal. X-type ligands donate one electron to the formation of a covalent bond, with the metal donating the other. Z-type ligands form a dative bond with the metal, where the metal donates both electrons to the formation of the bond.

The work of the Giansante research group provides a wider framework for understanding ligands as a whole by separating the molecule into two different parts: an anchor and a pendant. This pendant can be further split into a backbone and substituent [172]. In this model, the role of the ligand can be summarized in three main categories. Firstly, the ligand must passivate surface states on the quantum dot through co-ordination or covalent bonding to a surface atom, as seen in Figure 2.4. Secondly, the ligand mediates the interaction of the quantum dot with its environment, for example its solubility or its packing structure [173]–[175]. Thirdly, the ligand changes the charge density around the quantum dot, affecting its band structure and interactions with charges without sacrificing quantum confinement effects [55], [56], [176]. This was systematically studied by

Brown *et al*., demonstrating the band position can be altered by nearly 1eV relative to the vacuum level simply by changing the coordinating ligand [55].

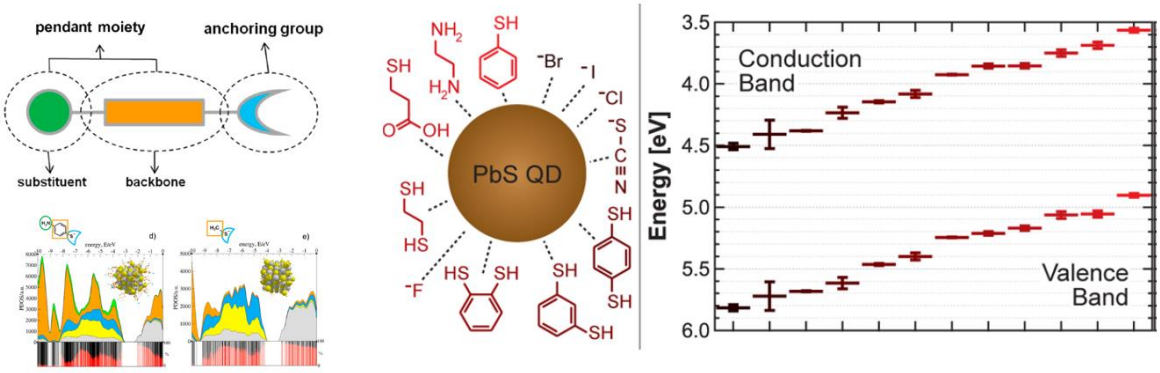


Figure 2.4 - Organic ligands can be divided into three general sections – anchoring groups, backbones, and substituents. Addition of ligands increases the density of states, with the location and number of states changing depending on each section of the ligand. Reprinted with permission from J. Am. Chem. Soc. 2015, 137, 5, 1875–1886 and ACS Nano 2014, 8, 6, 5863–5872, copyright 2021, American Chemical Society

2.4.1 Synthetic Ligands for Devices

Originally, synthetic ligands such as oleic acid and oleylamine were chosen for their ability to effectively passivate quantum dot surfaces and to keep the colloidal solutions within which the quantum dots were formed stable. The long-chain hydrocarbon pendants effectively passivate the quantum dot surface, and mediate interaction with the environment by stabilizing nucleation and growth. After synthesis, these ligands are also useful for storage as the long pendant moieties prevent aggregation and loss of quantum confinement effects. For device manufacturing, such separation becomes detrimental to the performance of the cell, and the ligands must be altered to better satisfy the third criteria of ligand selection [177]. Turo & MacDonald demonstrated the concept of a cleavable synthetic ligand, where addition of a base to the colloidal suspension cleaves the stabilizing long-chain hydrocarbon. This preserves the initial passivation regime and allows for suspension in polar solvents whilst reducing the interdot distance considerably [178]. Despite this inventive approach, the majority of literature has proceeded by replacing the synthetic ligand entirely in a process call ligand exchange.

2.4.2 Ligand Exchange

Ligand exchange happens in either in solid state or solution. Solid state methods deposit a solution of ligand onto a preformed quantum dot film, removing and replacing the ligand that was previously coordinated [139], [179]. Film thickness can be increased by repeating the process with a new layer of quantum dots, known as a layer-by-layer approach[53]. Solution phase ligand exchange mixes two immiscible solutions of quantum dots and target ligand, forming a concentrated ink after the phases separate [51], [177]. The stability of these inks also depends on the electrostatic interaction of the ligand and the solvent.

The co-ordination method of the ligand is crucial in understanding the type of surface states it will passivate. Certain anchor groups have two different coordination regimes depending on the plane of the exposed surface. Carboxylic acids have been shown to coordinate as both L- and X-type ligands, with X-type coordination requiring trap-inducing hydroxide ions to achieve a balanced charge [110], [180]. Each coordination method serves a different passivation role. In chalcogenide quantum dots, X-type ligands are used predominantly to correct charge imbalance on the surface of the dot and prevent fusion of quantum dots [112]. L-type ligands act as reducing agents for surface atoms, removing or preventing the oxygen mid-gap trap states [109]. Z-type ligands can be thought of as oxidizing agents, and there is disagreement within literature as to their effects on trap passivation. Density Functional Theory calculations show the use of Z-type ligands can increase trap states through oxidation of group VI surface atoms like sulfur or selenium [108]. Experimentally, Huang *et al*. demonstrated mildly oxidizing Z-type ligands have been found to passivate trap states responsible for lower open circuit voltages, as well as hydroxyl ions on surface metal atoms [181], [182].

2.4.3 Small Organic Ligands

The anchor is used to coordinate the ligand to chalcogenide quantum dots and can be considered the main functional group of the ligand. Depending on the type of chalcogenide used, amines and carboxylic acids have also been poplar ligands. Amines were originally preferred by the field of research due to the nonbonding electron pair being an ideal candidate for L-type coordination, with butylamine and pyridine seeing the most use. In lead sulfide quantum dots thiols are the most popular class of organic ligand anchor, receiving extensive research attention.

Bifunctional ligands are molecules where the pendant moiety can act as a second anchor. This allows the ligand to passivate an additional trap site, often on a second quantum dot forming a closely packed network. One of the most studied compounds is ethanedithiol (EDT), first used by McDonald *et al*. [183]. Shortly thereafter, Klem *et al*. reported a 50x increase in power conversion efficiency compared to the native synthetic ligands, attributed to shorter interdot distances and a reduction in surface oxides [184]. Further work by Klem *et al*. showed that by annealing EDT ligand exchanged films, oxide concentration could be reintroduced without sacrificing mobility leading to a more heavily p-doped material [185]. The degree to which interdot distance influences charge transfer was studied by Nakazawa *et al*., determining the maximum interdot distance at which bi- or tri-excitons can dissociate before recombining [186]. The Sargent group has demonstrated the resilience of thiol coordination in both solid and solution ligand exchange methods, with corresponding increases in passivation [138], [180]. More recent advances on thiol ligand design have been the use of lead thiolates in ligand exchange, wherein the lead cation binds to the surface sulfur atoms on the quantum dot as a Z-type ligand [187]. Ethanediamine (EDA) has also seen considerable use as an amine analog to EDT, though there is dispute over its efficacy in coordinating, especially in polar, protonated solvents [55], [188], [189]. Bifunctional ligands such

as EDT have also been shown to not fully passivate the PbS surface in comparison to halide ligands, which can lead to oxidation of the quantum dot and subsequent losses in performance [190].

2.4.4 Halide and Pseudo-halide ligands

Halide ligands are solitary anions of the group VII elements fluorine, chlorine, bromine, and iodine. These act as L-type ligands and passivate the metal surface atoms on chalcogenide quantum dots. Following Giansante's ligand framework, they can be considered an anchor group with no pendant moiety, leading to exceptionally short interdot distances.

Direct use of halide compounds has been shown to remove trap states associated with open circuit voltage reductions in the solar cell. Halide sources first took the form of bulky organic salts, shown to prevent quantum dot fusing during the ligand exchange [51], [180]. The organic cation of this salt is most commonly some form of alkylammonium. However, along with incomplete ligand passivation in the solid state relative to solution processing methods, the bulky alkylammonium part of this ligand can leave organic residues in the film that become optically active, inhibiting charge transport through radiative recombination [42]. This led to the use of smaller alkylammonium cations such as methylammonium or imidazolium in solution exchanged inks, as well as the development of post-exchange halide treatment to improve passivation coverage [42], [191]. The small size of the halide ions allows them to be used in concert with other passivation techniques, principally organic ligands [192]. Sun *et al*. showed that thiocyanate ligands act in a similar way to halide ions, and so coordinate well when used in conjunction [43]. Halides have also been introduced during the synthetic process to more effectively passivate between the bulky synthetic ligands, and are not removed during other ligand exchange steps [114], [159].

Halides and short chain organic ligands have also been used in concert to target different mobility-reductive effects. Pradhan *et al*. report the use of zinc iodide salts in conjunction with 3-mercaptopropionic acid to reduce the open circuit voltage deficit in bulk heterojunction quantum dot devices[67]. Similarly, Oh *et al*. showed that pseudo-halides can improve diffusion length by shortening inter-dot distances, while more traditional organic ligands can more effectively passivate trap states though X-type or L-type coordination, improving carrier lifetime[193].

A shift in the conceptualization of halide passivation by Lan *et al* in 2016 described the halide co-ordination as a redox reaction with the surface metal ion [52]. This expanded into the use of metal salts as the halide source. The metal, commonly chosen to match the metal in the chalcogenide quantum dot, coordinates as a Z-type ligand to remove hydroxyl groups from the surface while the halide coordinates to the surface metal in L-type configuration[194], [195]. Combining organic halides and metal halides has led to the concept of "perovskite shelling", where metal organic halides such as methyl-ammonium lead triiodide are used to shell the quantum dots in a metal organic framework, leading to excellent passivation and high mobilities [48], [196]–[198]. Whilst many approaches to perovskite shelling use a single halide type, such as the popular methylammonium lead triiodide ($MAPbI_3$), Albaladejo *et al*. and Han *et al* showed that multiple combinations of halides can be used to made a composite perovskite shell, resulting in the current record efficiency cell at 16.1% [149], [199]. A new champion device at 18.1% using fully perovskite quantum dots has been recognized by the National Renewable Energy Laboratory in Colorado, USA, however the fabrication process has yet to be published at time of writing [200]. While this performance is significantly lower than record efficiencies for perovskite and silicon PV technologies, it is important to remember from section 1.1.4 that quantum dots offer a unique possibility of breaking the Queisser limit for single-junction solar cells, on top of low-cost

processing, compatibility with flexible substrates, and excellent compatibility with other PV technologies in the area of tandem solar cells.

2.4.5 Conjugated Ligands

As discussed at length previously, passivation of quantum dot trap states through organic ligands is crucial to suppressing recombination pathways [201]. Moving beyond the role of the anchor, the backbone of a ligand can strongly impact the charge density around a quantum dot and therefore influence its optoelectronic properties. This is largely achieved by using conjugated backbone structures. Simple substituted benzene derivatives were shown to affect the charge density around quantum dots by Brown *et al*., leading to a shift in the band positions relative to the vacuum level [55]. This was expanded upon by Kroupa *et al*. demonstrating a tunable band gap by modifying the functionalization of cinnamate ligands, changing the dipole moment around the quantum dots [176]. Conjugated ligands can also be used to change the interaction of quantum dots with their environment. The conjugated π-systems in conjugated small molecules will preferentially align with other π-systems in parallel, a concept known as π-stacking [202]. Byosi and Kumar demonstrated elemental gold quantum dots as large as 20nm can be influenced by this self-assembly of small molecules such as liquid crystals [203]. Later, Giansante *et al*. showed that this can be used to change the packing structure of the quantum dots in solar cells [204].

2.4.6 Coupled Organic Inorganic Nanostructures (COINs)

Combining the self-assembly nature of conjugated ligands with the coupling of electronic states, large ordered systems interlaced at the nanoscale can be created. Broadly, the inorganic component of COINs is not limited to quantum dots but can also be applied to 2D materials such as single layer transition metal dichalcogenides and 2D perovskites [205]–[207]. Similarly, the range of organic materials is not limited to directly coordinating ligands but also small molecule and

polymeric organic semiconductors[208]–[210]. These coupled organic-inorganic nanostructures display emergent properties unavailable to pure inorganic or purely organic systems [211]. Of particular interest are directed optoelectronic phenomena such as singlet fission or hot electron harvesting [105].

In a small molecule organic semiconducting packing structure, π-stacking can occur in multiple configurations. These different offsets between adjacent molecules, known as H- and J-aggregates, change how their orbitals overlap according to the Franck-Condon principle [212]. As such, organic semiconductors composed of small molecules must make sure that these molecules pack in combination with an inorganic component such that the right aggregate packing structure is maintained. Zhang *et al*. initially demonstrated in 2007 that dipole-dipole interactions between cyanine dye J-aggregates and quantum dots induced a rapid FRET-like energy transfer between organic and inorganic phases, effectively increasing the quantum dot absorption cross section by a factor of ten [125]. Walker *et al*. expanded on this concept by directly coordinating J-aggregates of cyanine dyes to quantum dot surfaces. This work achieved 98% charge transfer efficiency, improving the absorption coefficient of the film in the J-aggregate range whilst maintaining tunable emission of the quantum dot [213], [214].

The extension of COINs into truly 3-dimensional structures by Scheele *et al*. in 2014 marked an important development in the field. This was achieved by creating a tetrathiafulvalene ligand, with molecular design ensuring good band-matching the HOMO of the ligand to the valence band of the quantum dots [136]. Scheele was able to produce an extended band-like state for hole-transport, whilst maintaining quantum confinement of the conduction band for electrons. This band architecture was later inverted by André to produce extended states for electrons [81]. In both cases, the rigid structure and π-stacking of the conjugated organic ligands led to increased long-

range order in the quantum dot films, further improving mobility despite the increased interdot distance.

2.4.7 Hybrid Polymer-nanostructure devices.

As mentioned previously, the concept of coupled organic inorganic nanostructures can be expanded from small molecule organic semiconductors to larger molecular weights, such as oligomers and polymers. Wide bandgap polymers such as poly(3-hexylthiophene), abbreviated to P3HT, have been shown by Giansante and Mastria to hinder the population of quantum dot mid-gap trap states, leading to reduced recombination and improved charge transport [215], [216]. This was determined to occur due to the band alignment between polymer and quantum dot resulting in charge transfer to band-edge states being more favorable than mid-gap states, while the opposite was seen with low-band-gap polymers. This was also found to be independent of charge mobilities in the polymer. Further, Wang *et al*. observed the onset of hole transport from quantum dot to P3HT after ligand exchange of the quantum dots to shorter, optically inactive ligands [201]. An explanation for this is provided by Xue *et al*., wherein polymers with systematically modified side-chains were shown to have increasing hole mobilities. When used as hole-transport materials in hybrid solar cells, band alignment that was more favorable for hole-transport form inorganic to organic phases. This efficiency is explained by the band alignment resulting in charge transfer via band-edge states instead of mid-gap states, suppressing trap-assisted Shockley-Reed-Hall (SRH) recombination pathways at the polymer-quantum dot interface [217]. P3HT has also been shown to promote dissociation in the relaxation pathways of hot excitons, leading to both hot and relaxed hole transport from PbS quantum dots to the polymer [127]. The choice of organic semiconducting polymer is important. In specific PbS cases, improved short-circuit current densities and fill factors of the devices employing thiophene-rich polymers as hole transport layers indicate thiophenes are

important for efficient charge collection [218]. Ren *et al*. showed that P3HT nanowires and CdSe quantum dots can be grafted together using a ligand exchange process, greatly increasing electronic coupling between organic and inorganic phases. This resulted in devices with high V_{oc}, J_{sc}, and fill factor [70]. Similar effects were also observed by Zhang *et al*. by using a bulk-heterojunction of organic polymer and acceptor molecule as a combined hole-transport layer [219]. Reaching beyond polymers, COINs utilizing graphene and carbon nanotubes have been demonstrated by Neo *et al*., and Tazawa *et al*., respectively [220], [221].

As in the case of small molecule COINs, the nature of mechanical coupling and its effect on the electronic coupling of the organic and inorganic components is key to understanding and optimizing material performance [105]. Whilst examples above show good stability between otherwise separate organic and inorganic phases, more direct mechanical coupling can further improve the electronic coupling of the two components. In addition, long-range order of quantum dots is lost upon the disordered introduction of these highly extended organic semiconducting states. End-functionalization of polymer chains has shown increased phase stability and as a result higher electronic coupling using a variety of anchoring groups [71], [118], [222]. However, attempts to polymerize *in-situ* with initiators or metal catalytic centers to achieve high molecular weights compete make colloidal dispersions of the COINs unstable [223], [224].

The use of *in-situ* polymerization to achieve high coupling of organic and inorganic phases was recently reported by Ortiz-Cervantes *et al*. using a polydiacetylene. By incorporating a diacetylene substituent into the organic component of a 2D perovskite layer, topochemical polymerization digitated monomers produced a conjugated polydiacetylene backbone and a high degree of electronic coupling. Conductivity of the resulting thin film subsequently improved by three orders of magnitude relative to comparable 2D perovskite materials [225].

2.5 Diacetylenes

Diacetylenes (or diynes) are a class of organic molecule characterized by two adjacent carbon-carbon triple bonds spread over 4 sp-hybridized carbon atoms in a row, also known as a butadiyne [226]. Diacetylenes are the simplest of the oligoynes, a class of organic compounds wherein 4 or more sp-hybridized carbons are connected in a line. This sp-hybridized backbone is a remarkably rigid and inert functional group, and has found uses ranging from liquid crystal displays to antiretroviral medicine. One of the diacetylene's key features is that of topochemical polymerization, the ability to polymerize in the solid state under relatively mild conditions. Poly (diacetylene) has a π-conjugated backbone consisting of alternative double, single, triple, and single bonds. It has found applications in polychromic liquid crystal displays, sensors, and thanks to its unique chemical signature, forensic fingerprint identification [227]–[231].

Diacetylenes are most commonly formed through the well-established coupling of terminal alkynes, molecules where there is a carbon-carbon triple bond followed by a hydrogen. This coupling mechanism was first shown by Carl Glaser in 1869 making symmetrical diacetylenes [232]. The reaction proceeds under atmospheric conditions, phenylacetylene reacts with copper (I) chloride to form copper phenylacetylide, which then dimerizes to form the diacetylene. Oxygen is consumed in this dimerization, forming water and reforming the copper chloride [233].

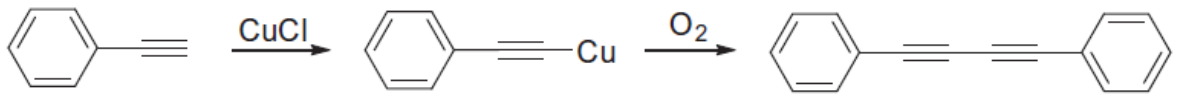


Figure 2.5 - Reaction pathway for homo-coupling of terminal acetylenes as discovered by Glaser in 1869. Reprinted with permission from Shi & Lei, 2014 [233].

This was improved upon to include the formation of macrocyclic compounds by Eglinton, Hay, and Sondheimer in the mid-20th century with the discovery that amines performed well as a ligand to the copper, reducing the amount of copper (I) chloride needed [234], [235]. Catalysis was

improved by using other trace amounts of catalytic metals like gold and palladium [236]–[238]. Later studies showed that the organometallic intermediate can be made with other metals, opening the reaction to other metals and metalloids such as tellurium, silicon, and iron [239]–[241]. The reaction is mostly done using aromatic or aliphatic terminal acetylenes, and has proven to be highly versatile in this regard [242]. Functional groups such as carboxylic acids have been shown to also undergo this reaction, forming end-functionalized diacetylenes directly [243], [244].

Heterocoupling of terminal alkynes to produce asymmetrical terminal alkynes is possible via this method, but as coupling is not controlled the products follow a statistical distribution of probability and yield. Targeted heterocoupling can be done via the Cadiot-Chodkiewicz reaction wherein a terminal alkyne is coupled with a 1-haloalkyne, this has been the main synthetic route since its discovery [245]. More complex methods such as specific reagents in the Fritsch-Buttenberg-Weichell or the Negishi coupling require more expensive catalytic agents, but offer milder conditions and a wider variety of end functionalization compared to just haloalkynes [246]–[249].

2.5.1 Topochemical polymerization

Polymerization of oligoynes in the solid state is a unique property almost exclusive to this group of organic compounds. As this thesis will exclusively use diynes, diynes will be used throughout the rest of this thesis in illustrative and descriptive examples, though other molecular systems exhibiting this solid state polymerization exist [250]. The phenomenon was first documented by Seher upon irradiation with ultraviolet light, higher wavelength radiation, or annealing below the melting point of the monomer [251], [252]. The polymerization proceeds without initiators and in the solid state as a result of the monomer's packing structure in the solid state.

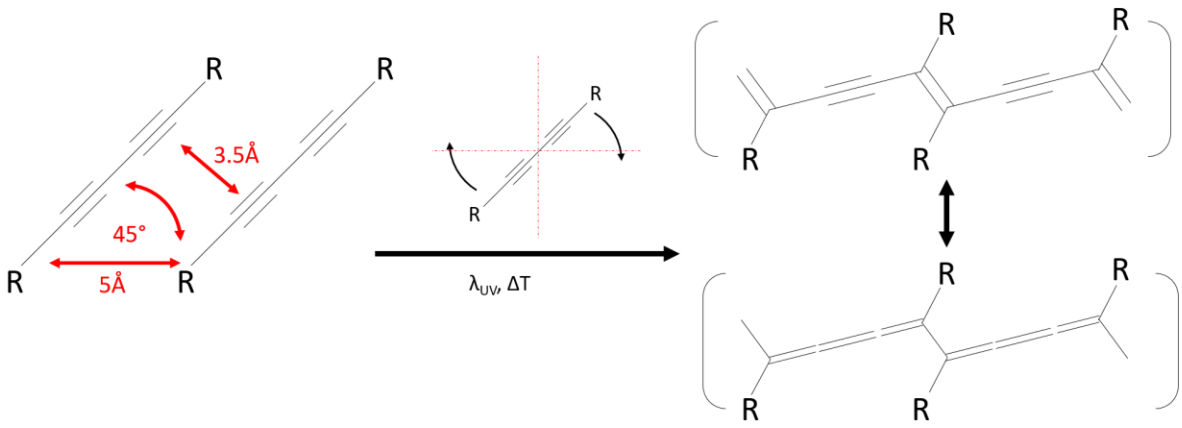


Figure 2.6 - Topochemical polymerization conditions and 1-4 addition mechanism, showing the movement of the monomer crystal in a "turnstile" fashion. The conjugated polymer has two resonance structures.

Ideal conditions require the monomer to be aligned such that identical carbons in neighboring molecules are 5Å ($5x10^{-10}$m) apart and oriented at a 45° angle. In this configuration, neighboring diacetylene bonds are 3.5Å apart. Excitation with ultraviolet light induces a rotation in the molecular crystal, wherein the monomer will undergo a 1-4 addition polymerization with its neighbor [251], [253], [254]. This forms a conjugated network of alternating double-single-triple-single bonds, a conjugated network [255]. The network is able to form a resonance structure wherein the single-triple-single bonds are converted entirely to double bonds, as shown in Figure 2.6.

Topochemical polymerization of diacetylenes and oligoynes has two key applications. In synthesis, it can become a useful step in linking small molecule systems together, in particular as part of a route towards functionalized carbon allotropes such as graphene or nanotubes [256]–[258]. Additionally, small changes in strain on the conjugated backbone can lead to changes in its absorption profile due to conjugated π-systems being knocked out of alignment. This allows functionalized polydiacetylene to be used as a chemical sensor [227], [259], [260]. The highly regular packing of diacetylene monomers and their subsequent *in-situ* polymerization has seen use in functional nanocomposites as well. Liquid crystals formed from long-chain diacetylenes can be

used to align silica nanocrystals. Patterning of the liquid crystal array via topochemical polymerization can then lead to functionalized nanocomposite materials [261], [262]. Further to this, it has been shown that nanocrystals can interact with the polydiacetylene, inducing polymerization through photoluminescence of TiO_2 and ZnO [263]. The surface of polydiacetylene has also been used as a substrate to grow highly ordered arrays of PbS quantum dots through chemical vapor deposition, demonstrating the chemical resilience of the polymer and its favorable lattice matchup with PbS [264].

2.5.2 Diacetylene Photovoltaics

The conjugated backbone of poly(diacetylene) gives it a HOMO-LUMO gap that can be adjusted based on its side chain functionalization[253], [265], [266]. The band gap is typically in the region of 2.2eV wide, with a HOMO level relative to the vacuum of -5.5eV [267], [268]. In addition, the charge carrier mobilities of solid state polydiacetylene have been reported to be several orders of magnitude above other organic polymer materials [253], [269], [270]. This has garnered interest in the use of polydiacetylene for organic photovoltaic applications. In these cells, the diacetylene monomer is functionalized with organic molecules and primarily incorporated as part of a bulk heterojunction [268], [271]–[274].

2.6 Summary of concepts

Quantum dots are interesting photovoltaic materials due to their tunable band properties, ease of processing, and unique potential to achieve efficiencies beyond the Queisser Limit. However, quantum dot thin films struggle with low mobilities due to low wavefunction overlap and surface area defects, resulting in devices with low fill factor, short circuit current, and open circuit voltage. Band-like states can be induced through the coordination of certain conjugated ligand systems and directed self-assembly through π-stacking. Conversely, extended states can be introduced through

the incorporation of organic semiconductors or carbon allotropes, though the size of these added systems inhibits the formation of long-range order in the cells. All of these approaches have been shown in isolation to produce the improvements in fill factor, short circuit current, and open circuit voltage, but have not been attempted in combination.

The work presented in this thesis will use π-stacking diacetylene monomers to passivate lead site trap states in PbS quantum dots, then polymerize the ligand *in-situ* in a separate step. Due to the novelty of *in-situ* polymerization in quantum dot systems, this work is intended to serve as a proof-of-concept, demonstrating that *in-situ* polymerization of the ligand within a precast film is both possible and advantageous, and recommends improvements to the process based on the findings detailed in subsequent chapters.

In-situ polymerization of ligands to produce extended π-conjugated systems combines three key aspects of thin film mobility: extended states, long range order, and effective passivation. This is anticipated to produce higher device efficiencies relative to established techniques due to the combination of all three aspects. The relatively wide bandgap of polydiacetylene formed by the polymerization of the monomer ligands should suppress hole-trapping mid-gap states as seen in other commonly used organic semiconductors such as P3HT. The band alignment of polydiacetylene with PbS shown in Figure 2.7 suggests that the polymer will serve as a hole transport system, with electrons benefitting from the long-range order induced by the self-assembling monomers. This is expected to lead to an increase in the external quantum efficiency of the device with corresponding increases in the fill factor, short circuit current, and open circuit voltage.

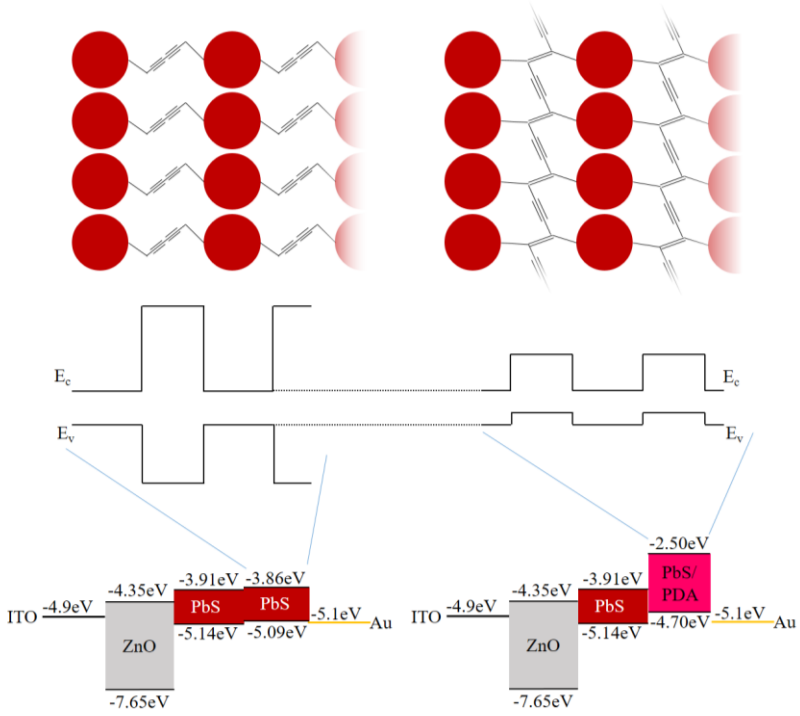


Figure 2.7 - Top: visual representation of the change in ligand structure from monomer (left) to polymer (right) after in-situ polymerization. Middle: nanoscale band alignment shows the ligand changes from a type-1 heterostructures with the quantum dot to a type-2 structure upon polymerization. Bottom: expected band alignment of the final devices before (left) and after (right) in-situ polymerization.

3 Methods

The methods described in this chapter are general methods for the preparation of common materials and control devices. Unless otherwise stated, all chemicals were purchased from either Merck or Fisher Scientific and used without further purification. In addition, unless otherwise stated, material synthesis and device fabrication are performed in air. Beyond fabrication of materials, films, and devices, the characterization of samples is critical in determining material and device properties. As such, characterization methods have also been detailed alongside any data analysis and processing methods to ensure transparency and reproducibility.

3.1 PbS Nanoparticle Synthesis

0.92 g PbS [Sigma Aldrich] was added to a three-necked round bottom flask (flask A), followed by 20 g of 1-octadecene [Sigma Aldrich] and 2.85 g of Oleic Acid [Sigma Aldrich]. To a second

flask (flask B), 10 g of 1-octadecene was added. Both flasks were magnetically stirred under reduced pressure for 1h at 110 °C. Flask B was brought under a nitrogen atmosphere and 0.42 ml Hexamethyldisilathiane (TMS) was added. After 15 further minutes, flask A was placed under an inert atmosphere. The contents of flask B were removed via syringe and injected into flask A. The reaction was left to run for 2 minutes before flask A was placed in cold water to quench the reaction. Both flasks were then exposed to room conditions and left in the fume hood for 90 minutes to let excess TMS decompose.

After 90 minutes, the contents of the flasks were equally distributed between 4 separate 50 ml centrifugation tubes of known weight. To each tube, 35 ml acetone was added, and the remaining volume of the tube was filled with methanol. The tubes were then centrifuged at 9000 rpm for 20 minutes. The supernatant was discarded and the process repeated. Once the quantum dots had been fully precipitated, the following cleaning cycle occur:

- 5 ml hexane is added to each tube and the tubes are sonicated for 10 minutes
- 35 ml methanol is added to the tubes to precipitate the quantum dots
- The tubes are centrifuged at 9000 rpm for 10 minutes
- Supernatant is discarded

After discarding the supernatant for the third time, the centrifuge tubes are left to dry in an oxygen free atmosphere overnight. The tubes are weighed to determine the yield, and a colloidal suspension of 75 mg/ml in octane is prepared. This is filtered with a 0.45 μm pore size polytetrafluoroethylene (PTFE) filter, then the suspension is brought to 50 mg/ml concentration for storage. The colloidal suspension can be stored at room temperature for up to 3 months.

3.2 ZnO Nanoparticle Synthesis

Two flasks are labelled A and B. For flask A, 2.92 g $ZnAc_2 \cdot 2H_2O$ [Sigma Aldrich] was added to 125 ml of methanol. For Flask B, 1.51 g of potassium hydroxide [Sigma Aldrich] was added to 65 ml of methanol. Both flasks were magnetically stirred and heated to 65°C. Flask B was then added dropwise to a continually stirred flask A. During the process, a precipitate formed then disappeared in flask A. After 2h, the precipitate returned. The solution was separated into 3 centrifuge tubes of known weight and centrifuged at 4000 rpm for 15 minutes. The supernatant was discarded and the nanoparticles were stored in a methanol: chloroform (1:1 ratio) colloidal suspension at 40 mg/ml concentration. This was stored at -8 °C for up to 3 months.

3.3 ITO substrate preparation and Cleaning

ITO-coated glass substrates were purchased from Delta Technologies in 150 x 150 mm sheets of 1.5 mm thickness. The substrates were cleaned by sonicating in de-ionized (DI) water with a surfactant, DI water, Acetone, and isopropanol for 20 minutes. A mask was prepared by cutting a mask from a vinyl adhesive sheet and laid over the ITO in strips 3mm wide, separated by 9 mm and running the length of the substrate sheet. After ensuring no air pockets were present under the mask, the substrate sheet was etched in piranha solution (Nitric acid and sulfuric acid 3:1 ratio) for 2 hours. The substrate sheet was then washed three times with DI water and dried in air for 1 hour. The mask was then removed by hand. Substrates were then cut into 11.8 x 11.5 mm device substrates using diamond saw of 0.5 mm thickness.

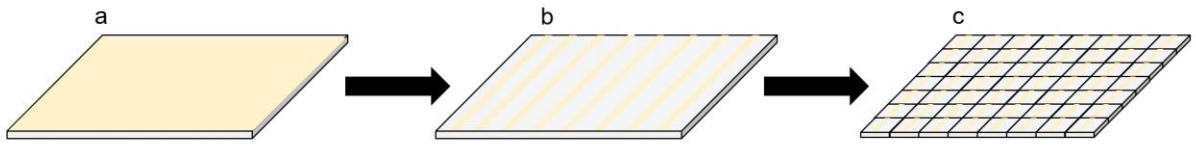


Figure 3.1 - Process for preparing ITO substrates. A sheet of glass coated in Indium Tin Oxide – ITO – (a) is masked and then etched in a 3:1 mixture of Hydrochloric acid and Nitric acid, respectively, at 60°C for 8 minutes. The mask is then removed to leave uniform strips of ITO on the glass surface (b). The glass is then cut to 11x12mm

substrates, with the ITO strip centered along the middle f the shorter edge, running the entire 12mm length of the substrate (c).

Prepared ITO device substrates were manually washed with an ethanol-soaked cotton swab for 30 seconds each side. The substrates were then sonicated for 20 minutes in each of DI water with a surfactant, DI water, Acetone, and then IPA. Substrates were dried under a stream of compressed nitrogen and then an ozone treatment of the ITO surface is applied for 10 minutes before device fabrication. When depositing films directly on glass, ozone treatment is not used to improve PbS adhesion.

3.4 Solid State Ligand Exchange Process

The solid-state ligand exchange process is detailed below using tetrabutylammonium iodide (TBAI) and ethanedithiol (EDT), due to their use in the control device. A solution of TBAI [Sigma Aldrich] was prepared at 17.5 mg/ml in methanol. An EDT solution was also prepared, as a 0.02% ratio by volume with acetonitrile. The substrate was placed on a spin-coater chuck and 85 µl of the 50 mg/ml PbS quantum dot colloidal suspension was added. The substrate was then spun at 2000 rpm for 15 seconds and brought to rest. The substrate was then flooded with 85 µl of the ligand solution and left to sit. After 60 seconds, the substrate was spun at 4000 rpm for 10 seconds, after which the surface was flooded with the pure solvent at rest and then spun to 4000 rpm for 10 seconds to wash the surface. The washing step was performed two to three times. This entire process, summarized below, was repeated a further 5-8 times to achieve the desired thickness:

- 85 µl PbS suspension in octane added to substrate
- Substrate spun 2000 rpm for 15 seconds
- 85 µl of ligand solution added to substrate for 60 seconds
- Substrate spun at 4000 rpm for 10 seconds
- 85 µl of ligand’s solvent at 0 rpm then removed at 4000 rpm for 10 seconds (twice)

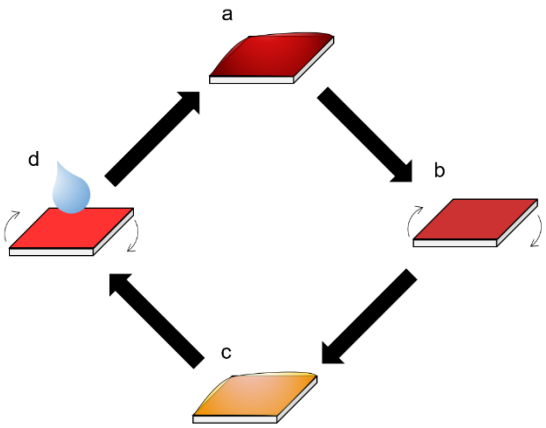


Figure 3.2 - Spin coating layer deposition for solid state ligand exchange (LX). In solid state LX, a suspension of known concentration PbS quantum dots is deposited on the substrate first (a). this is then spun to remove excess material and leave a film of near uniform thickness (b). To this film, a solution of known concentration ligand in an orthogonal solvent to that of the PbS is deposited, and left to perform LX for a defined period of time (c). The substrate is then spun at high speed to remove the ligand solution, and washed with the same pure solvent thrice more (d).

3.5 Solution Ligand Exchange Process

To a vial, 2 ml of a 2 M solution of 2-butynoic acid [Sigma Aldrich] in acetonitrile [Fisher Scientific] was added. 4 ml of the 50 mg/ml colloidal PbS quantum dot suspension was added on top of the acetonitrile. The mixture was shaken for 30 s by hand and then left to phase separate. The octane phase was removed by decanting with a pipette and 3 ml fresh octane was added. After shaking by hand again for 30 s and leaving the phases to separate, the octane was once again decanted and the acetonitrile phase was applied to a cleaned substrate. The substrate was then spun at 2000 rpm for 30 s.

3.6 Gold top-contact evaporation

Substrates were placed in a mask and loaded into an evaporator. After reducing pressure to 10^{-7} bar, 150 nm gold was deposited on the substrate rotating at 33 rpm.

3.7 Synthesis of dodeca-5,7-diynedioic acid

A 50 ml round bottom flask was filled with 10 ml of de-ionized (DI) water. To this, 3.585 g ammonium chloride was added. After magnetically stirring until fully dissolved, 1.9785 g of copper (I) chloride was added and the flask was heated to 60 °C. Separately, 737 µL of 5-hexynoic

acid was dissolved in 10 ml of DI water, and the solution was added to the heated flask with a syringe. Air was bubbled through the reaction and the water level carefully monitored, with additional DI water added if the level dropped. After 2 hours, a white precipitate had formed. The reaction was removed from heat and 11 ml of concentrated hydrochloric acid was added. This produced a brown solution around the white precipitate. The precipitate was removed through vacuum filtration and washed with a 1:1 volume ratio of DI water and concentrated hydrochloric acid. The precipitate was then dissolved in acetonitrile, dried over $MgSO_4$, and transferred to a vial for storage.

3.8 Work-up recrystallization method for Dodeca-5,7-diynedioic acid

Subsequent to the procedure described in Section 3.7, further recrystallization of the product was possible. 10 ml of the Methanol solution was added to 1 liter of 0.05 M hydrochloric acid in DI water. The solution is cooled to 1 °C for 3 hours and then vacuum filtered. The resulting white powder is then dissolved in acetonitrile, dried under $MgSO_4$ and stored in a 100 mg/ml solution that can be diluted for ligand exchange.

3.9 FTIR spectroscopy

Quantum dot thin films of glass substrates were analyzed using a Varian Excalibur FTS 3500 FTIR spectrometer. After cleaning the stage with isopropanol, the machine was calibrated before substrates were introduced by running a background scan from 1-8000 cm^{-1} a total of 64 times. The sample was then loaded into the machine and secured over the detector. As the detector is on the floor of the stage, thin films were place film-side down. Solid powders and liquids were also analyzed by depositing a small amount on the detector stage. A total of 64 scans were taken from 500-4000 cm^{-1} and averaged to produce the final spectrum. This spectrum was converted from

absorbance to percentage of light transmitted (%transmission) by the native data collection software, and the final result was reported with no further processing.

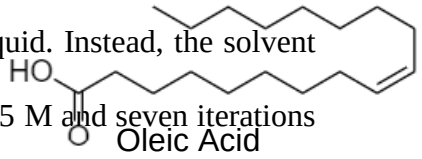
3.9.1 FTIR spectrum of Quantum dot thin films with propargylamine

PbS quantum dots were produced according to the standard procedures outlined in methods section 3.1. The ligand exchange from oleic acid to propargylamine was first attempted in solution phase, similarly outlined in section 3.5, and is based on the procedure from Liu *et al.* [42]. To this end, a 0.5 M solution of propargylamine in acetonitrile was created, 2 ml of which was combined in equal volume with a 50 mg/ml suspension of PbS quantum dots in octane. The mixture was shaken to form an emulsion and then left to stand while the phases separated. For successive phase mixings, small amounts of propargylamine were added to the solution slowly increasing the molar concentration of the propargylamine in the acetonitrile to 2 M. The experiment was then repeated with fresh PbS Quantum dots and pure propargylamine.

Solid state ligand exchange proceeded in an iterative layer-by-layer approach outlined in section3.4. PbS quantum dots in octane at a 50 mg/ml concentration were used for PbS layer deposition, and propargylamine was used as the ligand in a 0.5 M solution with acetonitrile. For each iteration, the propargylamine solution was left to rest for 1 minute, and the film was then washed with pure acetonitrile. The concentration of the propargylamine solution was increased to 0.75 M, 1 M, 1.5 M and 2 M in subsequent cycles. No film formation was observed after 5 iterations. In a separate experiment, a 1 M solution of propargylamine in methanol was used for the ligand exchange solvent instead of acetonitrile.

The starting concentration for ligand exchange of propargylamine was set as 0.5 M, the same concentration and solvent used in literature to coordinate ethanediamine (EDA) to the quantum dots [55], [188]. Solid state ligand exchange was conducted in a layer-by-layer approach as

outlined in section 3.4, up to 7 iterations. Due to the high toxicity and rapid absorption through the skin of propargylamine, it was deemed unsafe to spin-coat as a pure liquid. Instead, the solvent was changed to methanol and the concentration of acetonitrile reset to 0.5 M and seven iterations of the layer-by-layer solid state ligand exchange were conducted to produce a film.



Oleic Acid

The ligand-exchanged films of propargylamine from both acetonitrile and methanol were characterized using Fourier Transform Infrared Spectroscopy, and compared against pure propargylamine spectra as well as a film of PbS with oleic acid ligands. Propargylamine ligand exchange in acetonitrile gave only a background reading, indicating no presence of organic materials on the glass substrate. The results when using methanol as a solvent suggest that the oleic acid has been removed; the peaks in the 3000-3300 nm^{-1} range characteristic of C-H stretching vibrations have reduced in intensity, shown in Figure 3.3. These peaks are clearly visible in the oleic acid coordinated film due to the ligand's high number of C-H bonds.



Propargylamine

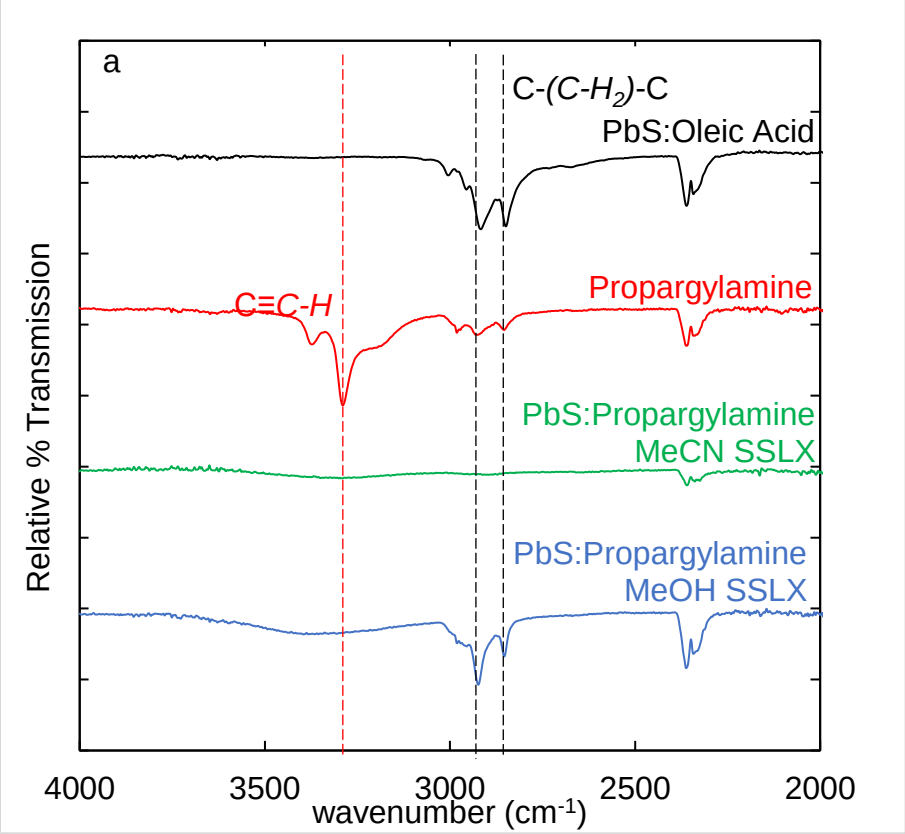


Figure 3.3 - FTIR spectra of propargylamine ligand exchanged film (blue) in comparison with pure propargylamine (red) and a film using the synthetic oleic acid ligand (black). The dotted lines show peak position for the terminal alkyne C-H stretch (red) and the alkane C-H stretch (black). Peaks at 2300 cm^{-1} are due to atmospheric CO_2 and are not labelled. Chemical structures (right) show oleic acid and propargylamine ligands.

The absence of the amine's symmetric and asymmetric stretching peak at 3300 cm^{-1} is encouraging, given that the co-ordination of the non-bonding electrons in nitrogen to the surface lead of the quantum dot would be expected to shift this N-H peak substantially. However, for propargylamine this peak corresponds not only to the primary amine stretching but also the terminal alkyne C-H stretch, which is expected even after ligand exchange.

3.9.2 FTIR spectra of 2-butynoic acid quantum dot thin films

FTIR spectra of each film was taken, alongside that of an oleic acid film, and pure 2-butynoic acid powder, these spectra are shown in Figure 3.4. The C-H stretching peaks at 2850-3000 nm^{-1} in the oleic acid peak are not present in the 2-butynoic acid films, indicating an absence of oleic acid in the ligand exchanged film. Additionally, the characteristic C-C alkyne bond stretch at 2240 nm^{-1} in the pure 2-butynoic acid spectrum is also present in the exchanged films. As the films were washed layer-by-layer during solid state ligand exchange to remove excess 2-butynoic acid, this further indicates a successful ligand exchange.

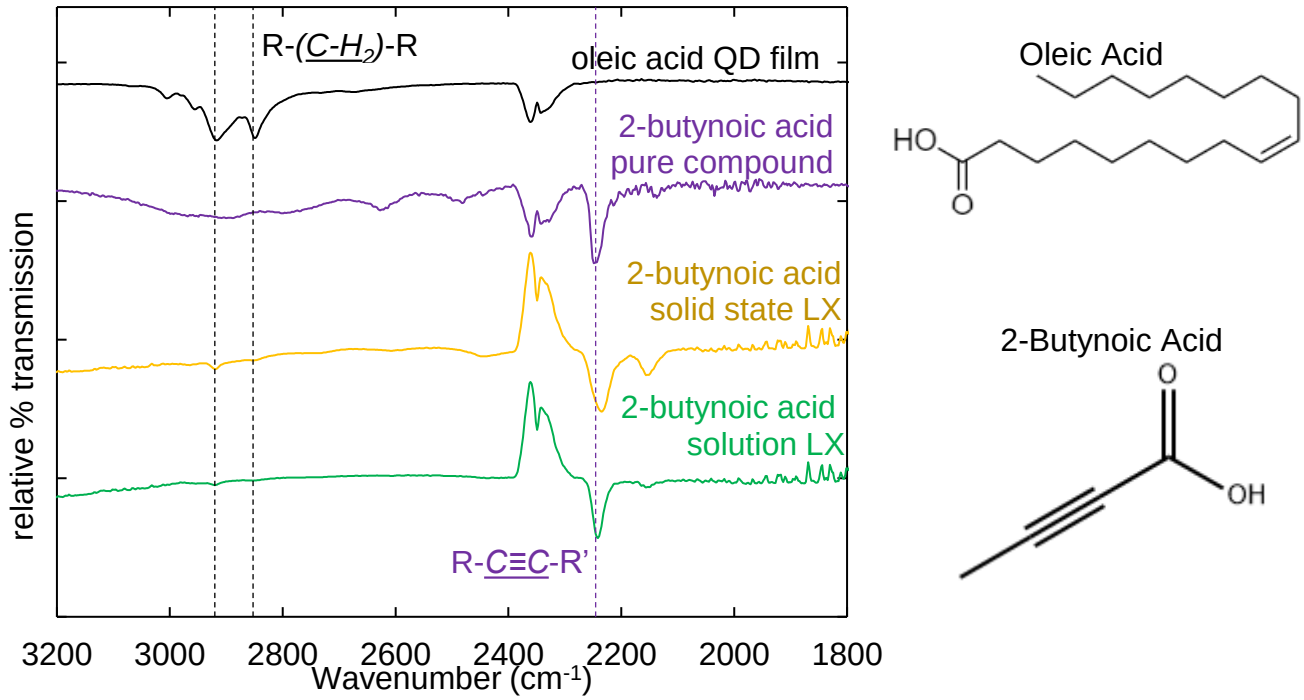


Figure 3.4 - FTIR spectra of oleic acid capped PbS films (black) compared to 2-butynoic acid ligand exchanged films (yellow, green.) The doted lines represent alkane C-H bonds in the oleic acid (black) and the alkyne triple bond in 2-butynoic acid (purple). Peaks at 2300cm-1 are atmospheric CO_2 and have not been labelled. Chemical structures of the ligands have been included (left) for clarification.

3.9.3 FTIR spectra of UV-cured Dodeca-5,7-diynedioic acid quantum dot thin films

Figure 3.5 shows that there is a peak at 2900 cm^{-1} as expected, confirming the presence of the polymer in some films. This is detectable in a bulk spectroscopic characterization tool like FTIR, where the penetration depth of the IR signal is several hundred nm, meaning there is enough polymer to quantify that the material does contain the polymer and the PbS.

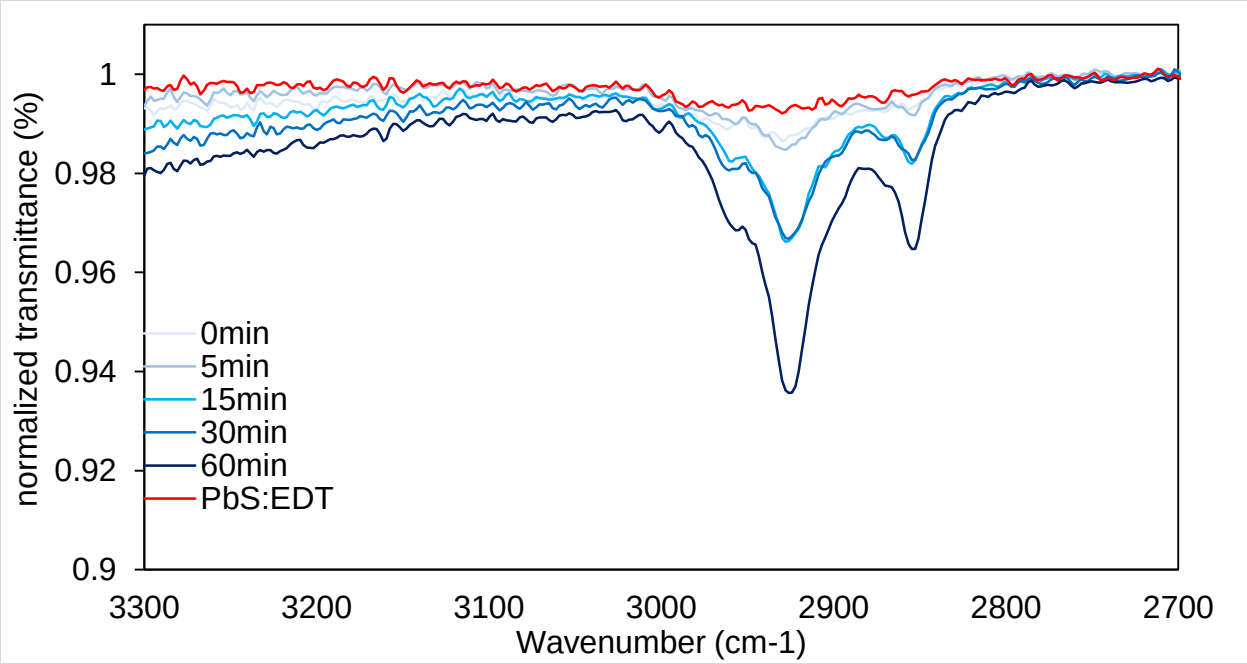


Figure 3.5 -A portion of the FTIR spectrum collected from PbS films after ligand exchange with dodeca-5,7-diynedioic acid and curing after q defined number of minutes per deposited film layer. Transmittance data has been normalized to the average value at 1900-2200 cm^{-1} so that the intensities of the peaks can be directly compared. The peak at 2950cm-1 indicates the presence of the backbone. As the curing time increases, the peak increases in magnitude, suggesting a higher degree of polymerization.

3.10 UV-vis Spectroscopy

Samples were characterized using a Varian Cary 5000 UV-visible-NIR spectrometer. The spectrometer was turned on and the sample holder for either solid films (on glass) or liquid solutions/suspensions (in cuvettes) was placed in the beam line. The machine was then calibrated by running two scans over the desired wavelength region; one scan with 100% transmission and one scan with 0% transmission (blocked beam.) Samples were then loaded into the machine along with a clean reference substrate. Scans of both sample and reference were taken simultaneously and the reference scan was subtracted from the sample scan by the data collection software to remove the substrate signal. The final spectrum was then used without further processing to determine the absorption profile (e.g.: the optical band gap) of the sample.

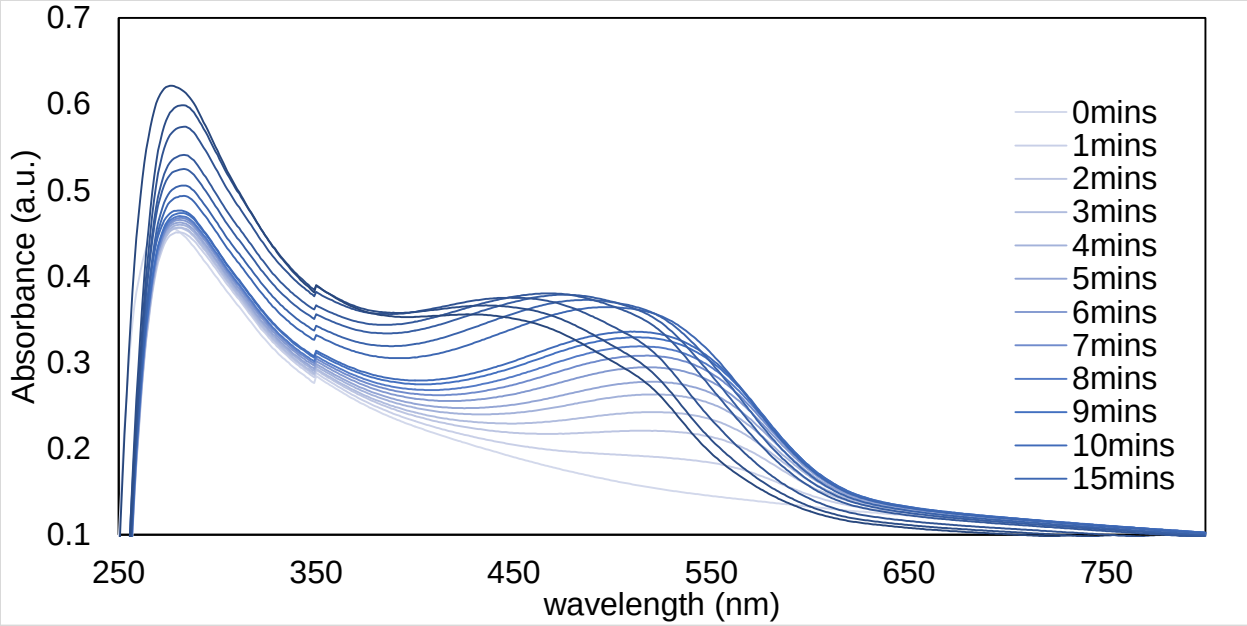


Figure 3.6 - UV-vis spectroscopy of dodeca-5,7-diynedioic acid polymerizing over the course of 60 minutes. The formation of a peak at 540nm indicates the formation of a conjugated pi-system with a bandgap of 2.2eV as expected.

3.11 Raman Spectroscopy

Samples were characterized using a JY Horiba LabRAM ARAMIS Imaging Confocal Raman Microscope. The Raman spectrometer was first calibrated using a clean silicon substrate, with the light source focused on the surface of the material. Lasers of 532 nm and 632.8 nm as well as diffraction gratings of 1200 nm or 1800 nm were used for the calibration. After calibrating, the sample was loaded and the light source was focused on its surface. Several factors were modified to fit the needs of the sample and prevent degradation during data acquisition. Laser light intensity was reduced or increased by applying filters, the spot size of the light incident on the sample was also changed according to the stability of the sample under laser light. As the spectra were collected in 400 cm^{-1} segments, the acquisition time and number of scans accumulated per segment were controlled. The spectrum was then displayed without further processing.

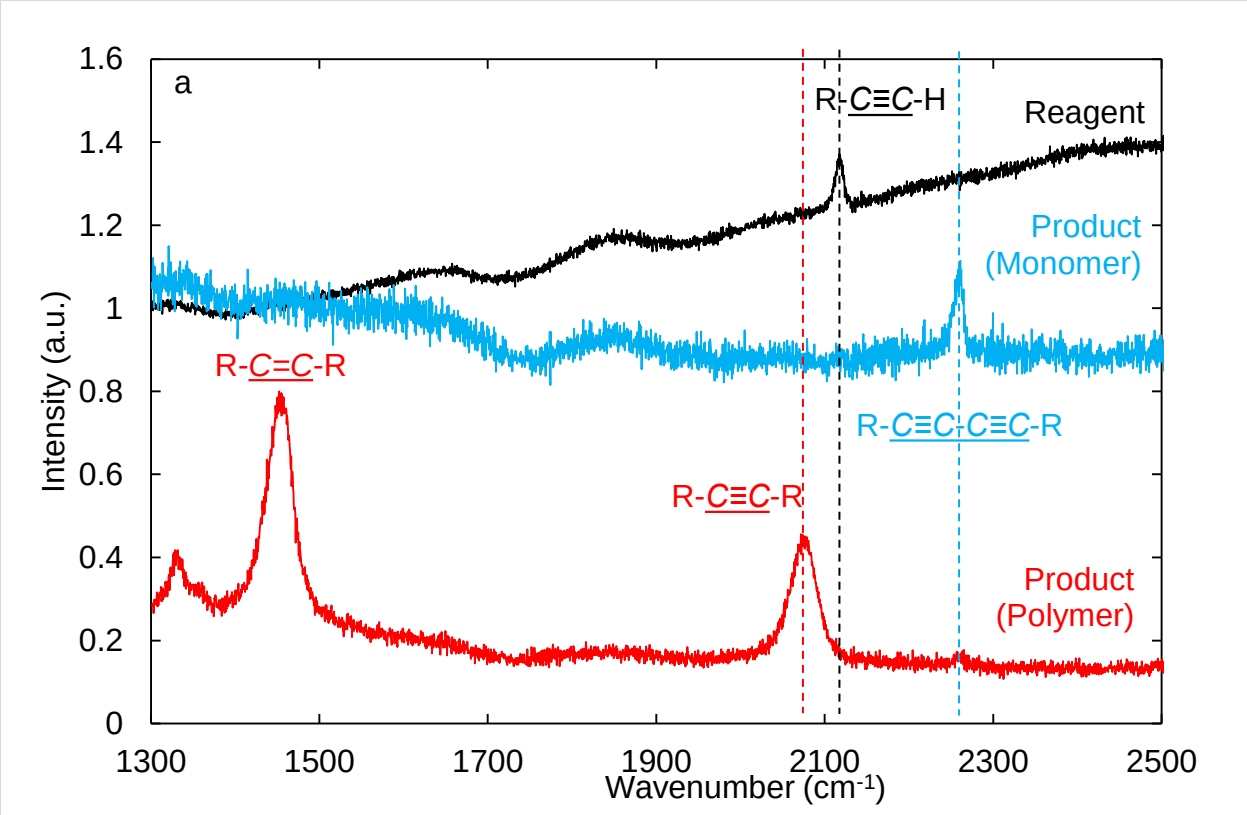


Figure 3.7 - Raman spectra of the terminal alkyne reagent (black), reaction product (blue) and reaction product after exposure to λ=254nm UV light for 10 minutes (red). Peaks corresponding to specific carbon-carbon bonds for each spectrum have been labelled in the respective color.

Raman characterization of the reagent and final precipitate is shown in Figure 3.7. Interpretation of these spectra centers on the 2000-2200 cm^{-1} region, where the characteristic alkyne bonds can be found. For the terminal alkyne reagent, the peak resides at 2120 cm^{-1}. This shifts to 2250 cm^{-1} upon completion of the reaction, indicating a change in the environment of the sp-hybridized carbons. The position of this shifted peak is characteristic of diyne molecules, indicating the desired product was formed [231], [260]. When polymerized, this alkyne peak shifts again as the diyne is converted into an internal alkyne unit, with a corresponding peak shift to 2080 cm^{-1}. In addition, the conversion of one sp-hybridized bond to the sp_2 hybridization regime, linking the monomers together with a double bond, can be seen clearly in the emergence of a peak at 1480 cm^{-1}.

3.12 Nuclear Magnetic Resonance (NMR) Spectroscopy

NMR samples were prepared by dissolving a small amount of the material in question in a compatible deuterated solvent, such as acetonitrile-d3 or chloroform-d. This solution was sealed in an NMR tube and characterized in a Bruker AVG400 NMR instrument. H^1 NMR spectra were sampled at 50 MHz and C^{13}NMR were sampled at 100 MHZ.

Analysis of the spectra was done using Mestrenova (v14.1.1). For each H^1NMR spectrum, solvent peaks were removed using the built-in solvent peak removal tool. Following this, automatic peak picking was used to identify all peaks in the spectrum. The selected peaks were then manually checked and reassigned to artefacts, product, or contamination. After removing non-product peaks, automatic multiplet analysis was used to determine which peaks were part of multiplets, and the product's target structure was loaded into the software. A built-in feature was used to automatically assign each hydrogen from the structure to an environment, which proved to be consistent with the expected result thus no manual adjustment was required. The spectrum was also compared directly to a predicted spectrum generated from an online database, as well as reported peaks from the literature [243].

C^{13}NMR peaks were loaded into the software and peaks were picked using the automatic peak picking tool. After manual checking of the peaks to reassign solvents and contaminants, the product's structure was loaded and peak assignments were automatically generated. The assignment tool showed good matching with the expected outcome and thus no manual adjustment was required. The spectrum was also compared directly to a predicted spectrum generated from an online database, as well as reported peaks from the literature.

Atom Position			Peak Shift (ppm)		
			Observed	Predicted	Literature
H^1 - NMR		O=C-C$\underline{H_2}$	2.46	2.45	2.45
		C$\underline{H_2}$-C	2.31	2.33	235.00
		CH2-C$\underline{H_2}$-CH2	1.79	1.85	1.81
C^{13} - NMR		$\underline{C}H_2$-C	18.53	18.59	18.20
		CH_2-$\underline{C}H_2$-CH_2	23.88	23.3	23.70
		O=C-$\underline{C}H_2$	32.52	2.6	32.90
		$\underline{C}$-$\underline{C}$	65.99	66.38	66.00
		CH_2-$\underline{C}$	77.6	79.03	77.90
		$\underline{C}$=O	174.36	177.06	174.30

Table 3.1 results of the NMR spectroscopy showing peak positions. Observed experimental values are compared to predicted NMR spectra and the reported values from the paper originally documenting the procedure. Original procedure published at Macromolecules 2009, 42, 7, 2609–2617.

NMR spectra were collected using chloroform-D. Table 3.1 shows the H^1 NMR and C NMR peaks from the predicted spectrum, the observed spectrum, and the original paper's results. The peaks are in good agreement with each other. Most importantly the presence of two peaks at 77 and 66 ppm in the C^{13} NMR spectrum from sp-hybridized carbons are characteristic of a symmetrical diacetylene.

3.13 Kelvin Probe

Samples were characterized on glass substrates using a KP Technologies Kelvin Probe. The machine was switched on 30 minutes before use, to reach steady-state conditions. An aluminum thin film on glass was then loaded into the machine as a reference, and grounded. The probe was

brought close to the sample and 1 run taking 25 measurements of the relative work function were taken at different points in the sample. The results were stored, and two more runs of the reference sample were taken in different locations, for a total of 75 measurements. This was then repeated for a second gold reference, and then the samples.

As the relative work function was measured, the absolute work function must be calculated from the raw data. The reference samples were metals with known absolute work functions, as such these were used to calibrate the measurement. Each reference sample's 75 measurements were averaged and the standard deviation is calculated. These relative work function values were plotted against the absolute work function values to produce two points connected by a straight line. The equation of this line was calculated using the average relative work function. Maximum positive and negative errors were calculated by using the line from the greatest difference between the two references, and the smallest different between the references, respectively. Average relative work functions of the sample were then calculated, along with the standard deviation. These values were applied to the line equations to give the final absolute work function of the sample, as well as the error values from the standard deviation. These were then used for further calculation of the material's band structure.

3.14 X-ray Photoelectron Spectroscopy (XPS)

Samples were prepared using the spin coating methods outlined in section 0, and placed in a Thermo Scientific K-Alpha XPS Instrument, equipped with a microfused monochromated aluminum X-ray source. To neutralize charging effects, a low energy ion flood source was used and a gold reference was included in the data collection. This gold reference was also used to calibrate Fermi level positions of quantum dot thin film samples. The source operates at 12 keV

with a 400 µm spot size. The analyzer operated at a constant analyzer energy for 50 eV for detailed elemental scans.

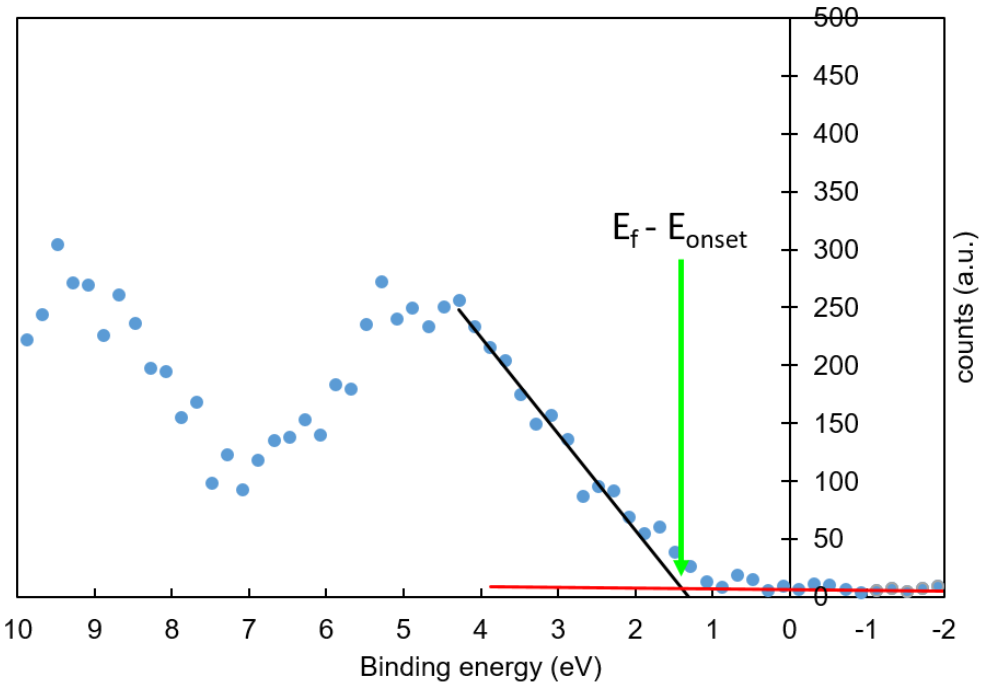


Figure 3.8 - Methodology for determining Valence band maximum position from X-ray Photoelectron Spectroscopy (XPS). After correcting for charging effects using the gold reference in the same sample holder, a baseline level of counts is established during the band gap below the Fermi level, at negative binding energies (red line). The linear portion after initial photoelectron count onset is also established (black line). The two linear regions are extrapolated until intersecting (green arrow). The difference between the intersection and the Fermi level at 0eV is the energy difference between the Fermi level and the valence band maximum.

To calculate the Fermi level offset, methods described by Brown and Kroupa were adapted[55], [74], [153]. A valence scan of each sample (binding energies of -5 to 40 eV) was taken, as well as for the gold control substrate. The photoelectron onset occurs at a noticeable point in the spectrum, typically before 5 eV. For each sample, the first and second derivatives of the data are computed analytically, and plotted against the binding energy alongside the raw data. The raw data is then fit linearly at the first inflection point, going from concave-up to concave-down. This is determined as the first positive point where the first derivative lies at a maximum and the second derivative is zero. As the data is collected in 0.02 eV increments, the closest datum to the turning

point and two points either side are used for the linear interpolation of the onset. A baseline is then calculated from the raw data, all points from -4 eV to -2 eV are fitted linearly. These values are chosen as a large range within the baseline that is not affected by the onset, nor influenced by the initial readings of the valence scan. These two linear fits are extrapolated until they cross, with the binding energy of the crossing point being the Fermi level of the material. Figure 3.9 demonstrates this process using a PbS quantum dot thin film sample, to provide a visual representation of the processing.

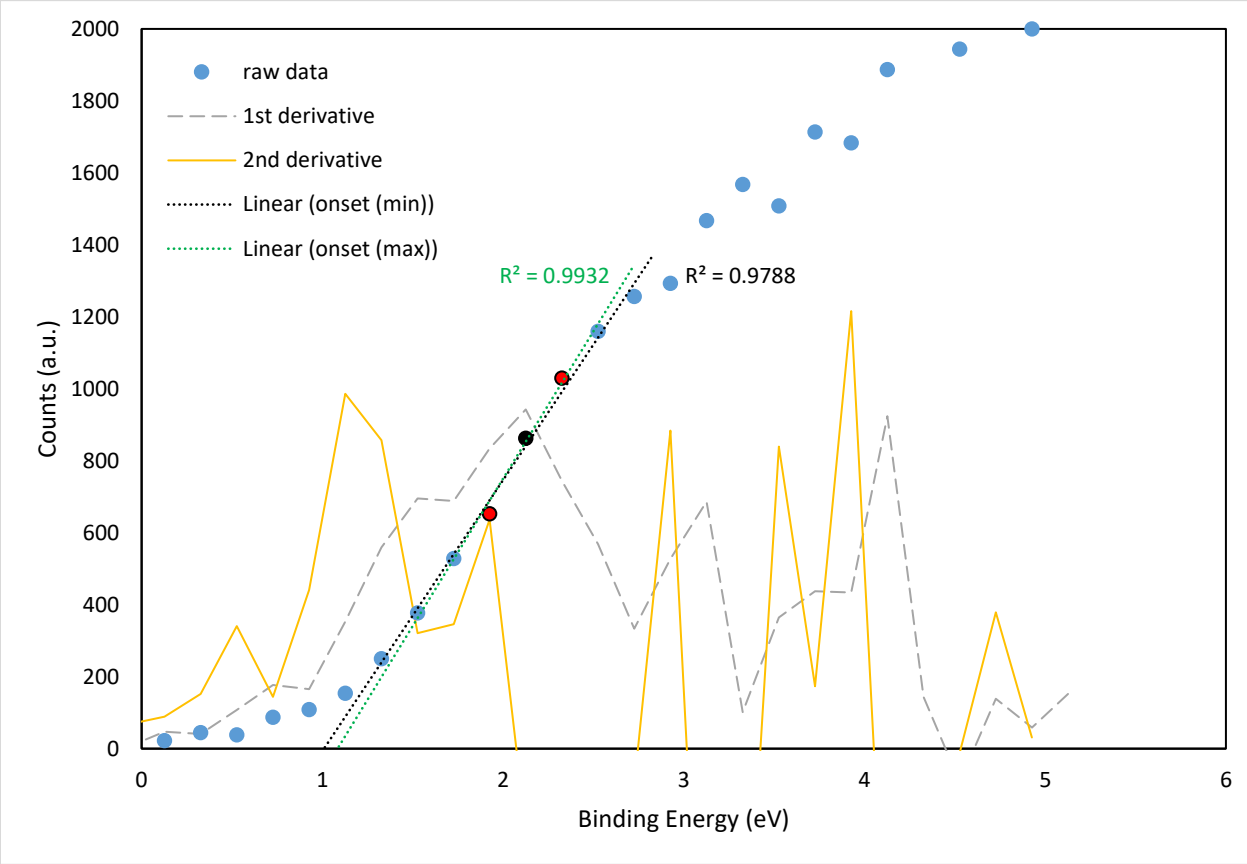


Figure 3.9 – Slope onset is calculated by taking the raw data (blue dots) and calculating the second derivative (yellow line). The first point where the second derivative intercepts the x-axis is determined to be the valence band onset (black point). The slope at this point extrapolated to the x-axis, giving the binding energy of the valence band. To account for noise in the reading, this process is repeated for points either side of the onset value (red) to give a maximum and minimum error value (slopes shown in black & green).

For the gold reference, this was assumed to be 0 eV as gold is a conductive metal with the Fermi level lying within the valence band. Deviation from this in the gold reference sample is

acknowledged as error due to sample charging and corrected for as a calibration step. All spectra were shifted such that the gold reference's photoelectron onset was at 0 eV to be in line with the Fermi level of gold. The process of best-fit line extrapolation was repeated for each sample to give the onset energy. To account for noise in the reading, this process is repeated for points either side of the onset value to give a maximum and minimum error value. This process was used for gold calibration and for calculating the valence band onset of samples, with errors compounded across gold calibration and sample calculation.

As the Fermi level resides within the band gap, and positive nonzero value obtained is interpreted as the energy level difference between the Fermi level and the valence band of the material. However, as Kroupa *et al*. describe, the onset energy itself is not the valence band position, due to the low density of states close to the valence band edge in PbS quantum dots [176]. As such, the authors state an empirically calculated correction must be applied, taking into account the band gap of the material. This takes the following form:

$$E_F - E_{VBM} = (E_F - E_{onset}) - \left(0.382 - 0.226\left(E_g\right)\right)$$

Where E_f is the valence band, E_{VBM} is the valence band maximum, E_{onset} is the onset energy of the XPS data, and E_g is the band gap of the material. Further detail on the nature of the correction is not elaborated upon in the source or its cited material, as such the correction was used as presented. To find the band gap, results from the UV-vis spectroscopy can be used, adding the material's exciton binding energy to the optical band gap as shown below:

$$E_g = E_{opt} + E_{bind}$$

Where E_g is the band gap, E_{opt} is the optical band gap from the UV-vis spectrum, and E_{bind} is the exciton binding energy of the material. For this analysis, an exciton binding energy of 0.09 eV was

used. This was taken from the Kroupa paper, as the exciton binding energy of PbS is not assumed to be size- or ligand-dependent.

Following from this, the band structure can be fully constructed by combining results from various analytical and spectroscopic techniques. Having used Kelvin Probe measurements to determine the work function, the energy of the Fermi level relative to the vacuum level is known. By adding E_F-E_{VBM} from XPS analysis as described above, the valence band energy is known. Finally, through the use of UV-vis spectroscopy and the band gap correction, the band gap of the material is known and the conduction band level can be calculated.

Deconvolution of XPS peaks to gain information on the chemistry of the sample is a complex task. Prior knowledge of the chemistry of the material is required to accurately interpret the spectra. For example, the C1s peak from an XPS spectrum will include emissions from each carbon 1s orbital in a distinct chemical environment. These different environments will have slightly different binding energies and as such will be shifted slightly relative to each other. Thus, the final peak will be a superposition of all these different chemical environments, and deconvolution will require an estimate to the number of distinct environments in each sample.

Detailed scans of the C1s peak region were analyzed in CasaXPS. Each sample was normalized and calibrated to a carboxylic acid peak at 289.3 eV, as determined theoretically by Zuilhof *et al* [275]. Subsequently, an analysis region was defined across the detailed scan and a spline Tougaard background was applied. Component peaks were then fitted using the default peak fitting algorithm in CasaXPS, with the number of components correlated to the number of different hybridization regimes expected in the sample. The spectra were then recalibrated to the sp3 peak component 285 eV and fitted again. Standard deviation of residual values was kept below 0.05 to ensure an accurate fit.

3.14.1 XPS elemental scans with peak fitting of amine-passivated PbS quantum dot films

Figure 3.10 shows a detailed scan of the N1s, C1s, O1s, and Pb4f regions for all amine-exchanged films. The N1s peak in each sample is nearly negligible and cannot be fit with more than one component. Additionally, there are no discernible differences between any of the high-resolution spectra apart from minor differences in the full-width-half-maxima of certain peaks and the positioning of the overall envelope. These minor differences can be attributed to increased scattering given the power of the incident x-rays and sample charging during characterization, respectively.

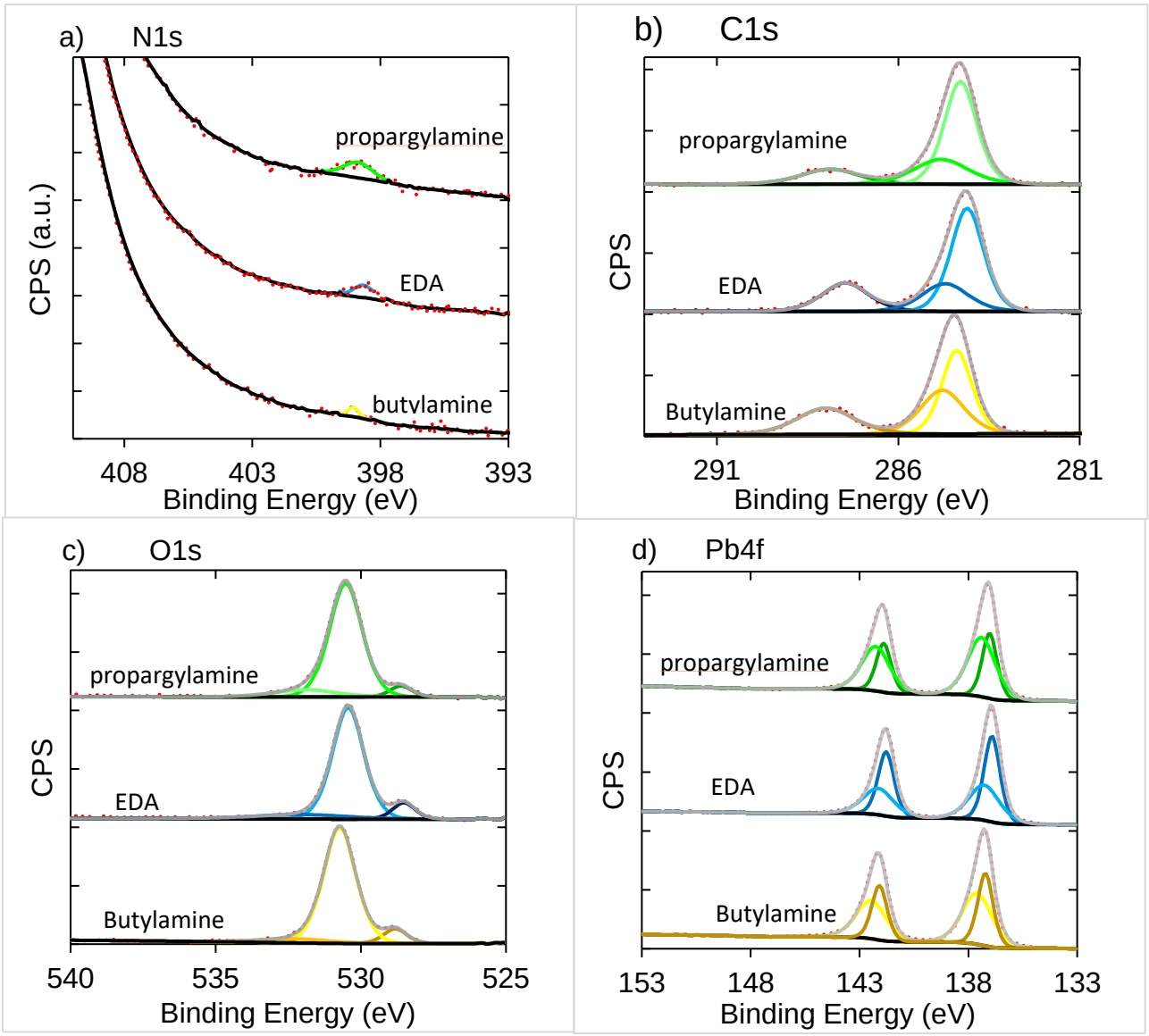


Figure 3.10 - High resolution XPS scans of a) nitrogen, b) carbon, c), oxygen, and d) lead for PbS quantum dot thin films after ligand exchange with propargylamine (green), ethanediamine (blue), and butylamine (yellow). The high degree of similarity between the spectra despite ligand differences suggests that the same ligand species have been coordinated in all films. The lack of a strong nitrogen peak despite supposed co-ordination of amine ligands also suggests the amine is not present in any of the films.

3.14.2 XPS elemental scans with peak fitting of 2-butynoic-passivated PbS quantum dot films

Figure 3.11 shows the XPS a detailed C1s elemental scan of PbS films passivated with oleic acid and 2-butynoic acid via solution and solid ligand exchange processes. The main peak is composed of two components: sp3 hybridized carbon and a lower hybridization regime dependent on the ligand. In oleic acid, this sp^2 hybridization is the ethyl kink on the 10^{th} and 11^{th}

carbons, whereas in 2-butynoic acid it is the sp hybridized alkyl bond directly following the carboxylic acid. In addition, the acidic carbon exists in a third, distinct chemical environment. In the oleic acid film, the sp3 hybridized carbon is the main component of the peak as oleic acid is primarily sp3 hybridized. Around this, the hybridization components in the main carbon peak changes as a result of ligand exchange. After ligand exchange, the component at 284.38 eV disappears and a new component at 285.31 eV appears. In addition, the presence of carboxylic acid peaks at higher binding energy further indicates that ligand exchange has occurred. Before ligand exchange, the carboxylic acid peak at 287.78 eV is negligible, as the ratio between it and the rest of the carbon in the ligand is 17:1. In the ligand exchanged 2-butynoic acid films, the ratio of anchor- to pendant-carbon is much closer at 4:1, and as a result the carboxylic acid peak at 288.51 eV is much larger comparatively.

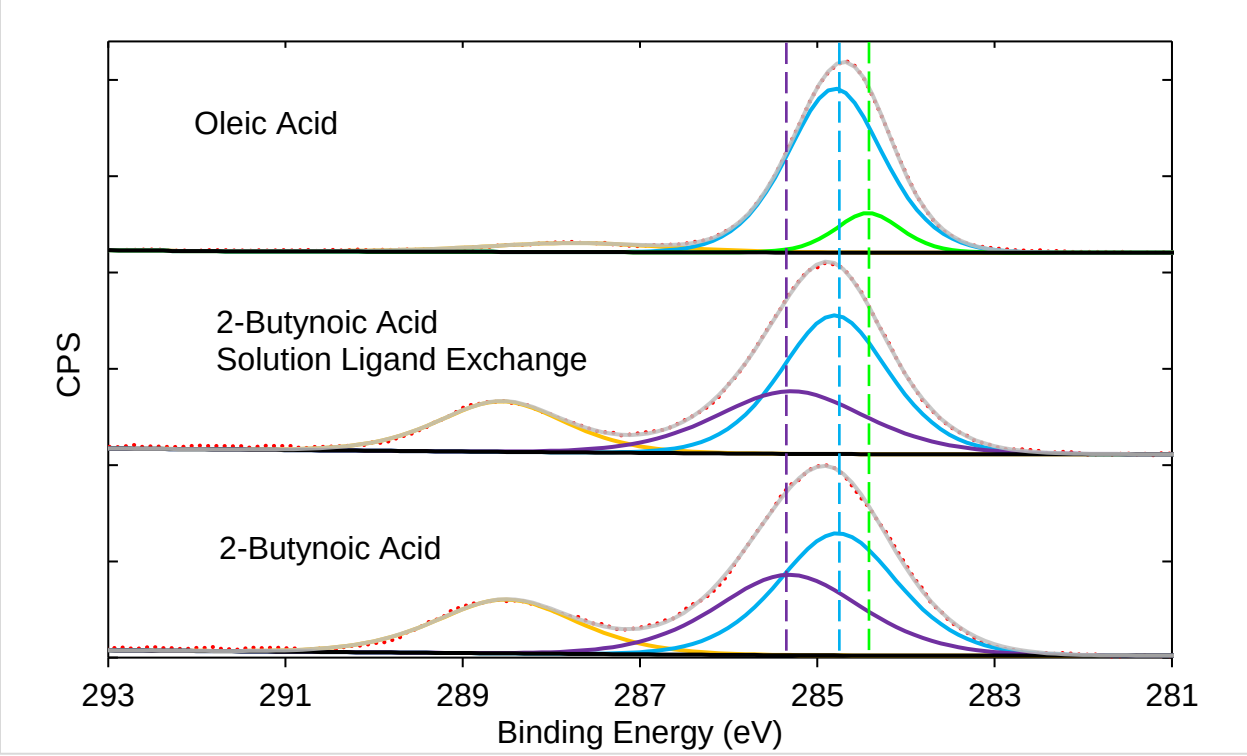


Figure 3.11 – XPS spectra showing the carbon C1s peak of oleic acid (a) and 2-butynoic acid exchanged through solution (b) and solid state (c) methods. The sp3-hybridized peak component (blue) is smaller after ligand exchange and the sp2- component (green) is replaced with a larger sp- component (purple), indicating the presence of an alkyne bond. The carboxylic acid peak (yellow) is much more prominent after ligand exchange, suggesting a ligand with a smaller pendant is present. Raw data (red dotted line) and background (black) are included.

3.14.3 XPS elemental scans with peak fitting of dodeca-5,7-diynedioic acid passivated films

Figure 3.12 shows the C1s elemental scans of PbS films coordinated with dodeca-5,7-diynedioic acid and exposed to UV-irradiation for a set period of time. Before UV exposure, the component peaks are primarily the sp and sp_3 hybridized peaks, as these are the two hybridization regimes present in the ligand. Upon UV irradiation, the ligand begins polymerizing, forming a novel sp_2 hybridized environment which is detected at higher binding energy to the sp_3 component.

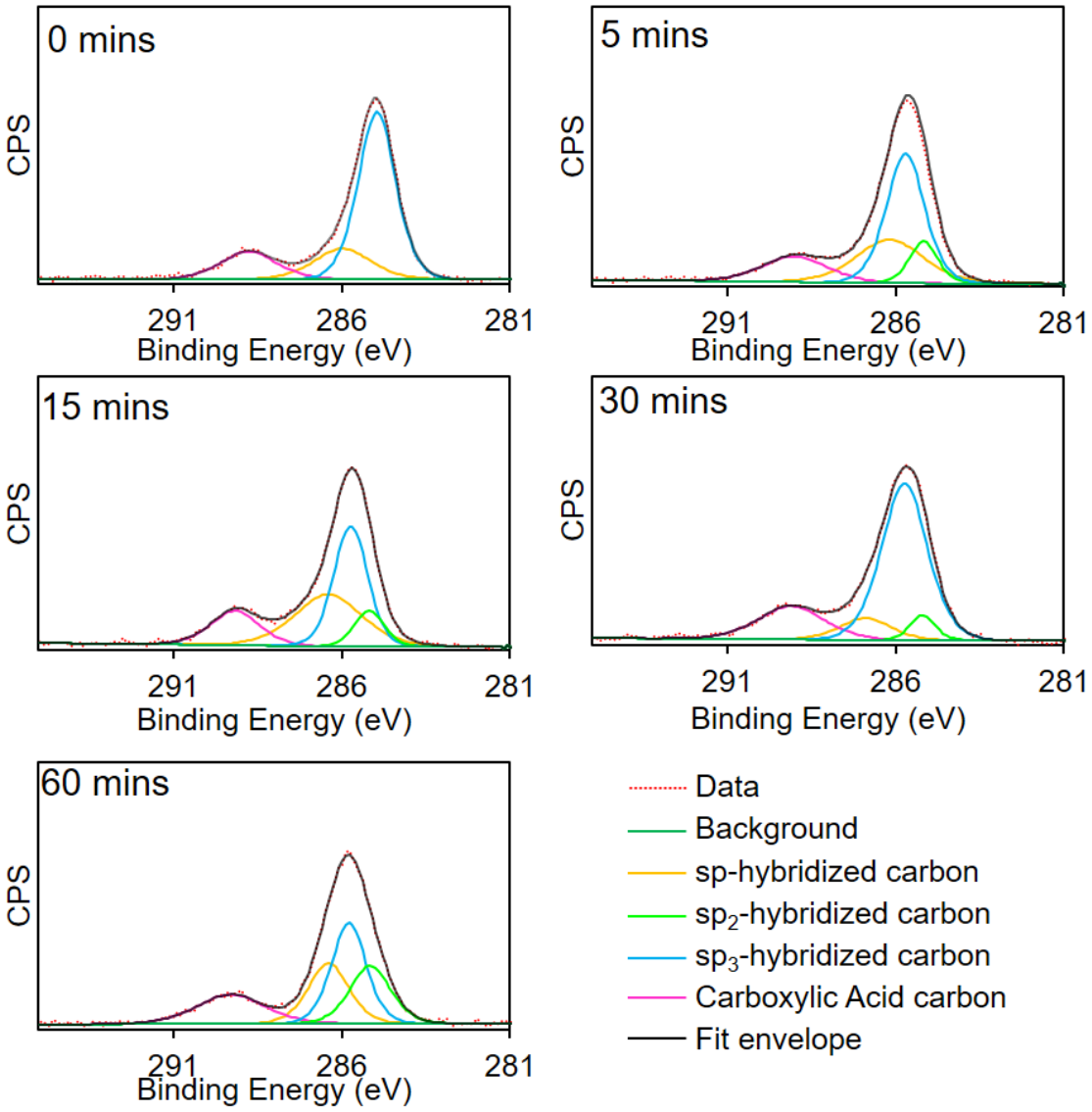


Figure 3.12 - X-ray photoluminescence spectroscopy C1s spectra of PbS quantum dot films coordinated with dodeca-5,7-diynedioic acid, with UV irradiation for five defined times between layer depositions. The alkyne carbon peak (yellow) is present in all films, however the alkene component (green) is only present in the UV-treated samples, indicating the formation of the expected polymer

3.15 Transmission Electron Microscopy (TEM)

Samples for TEM were prepared using Ultra-thin carbon grids on a lacey carbon background (UTC on LC on 300-mesh gold, EMResolutions). These grids were dipped in a 0.1 mg/ml solution of oleic acid capped quantum dots for 15 seconds. The grids were left to dry in air before being submerged in a 1M solution of propargylamine in a given alcohol solvent (one each of methanol, ethanol, and butanol) for 30 seconds, and left to air dry for 2 minutes. Finally, the films were washed by being dipped in methanol for 20s and left to dry under ambient conditions. The samples were observed using a JEOL 2100 transmission electron microscope running at 200 kV probe voltage. Pictures were taken at 80,000x magnification using the built-in CCD camera for all samples.

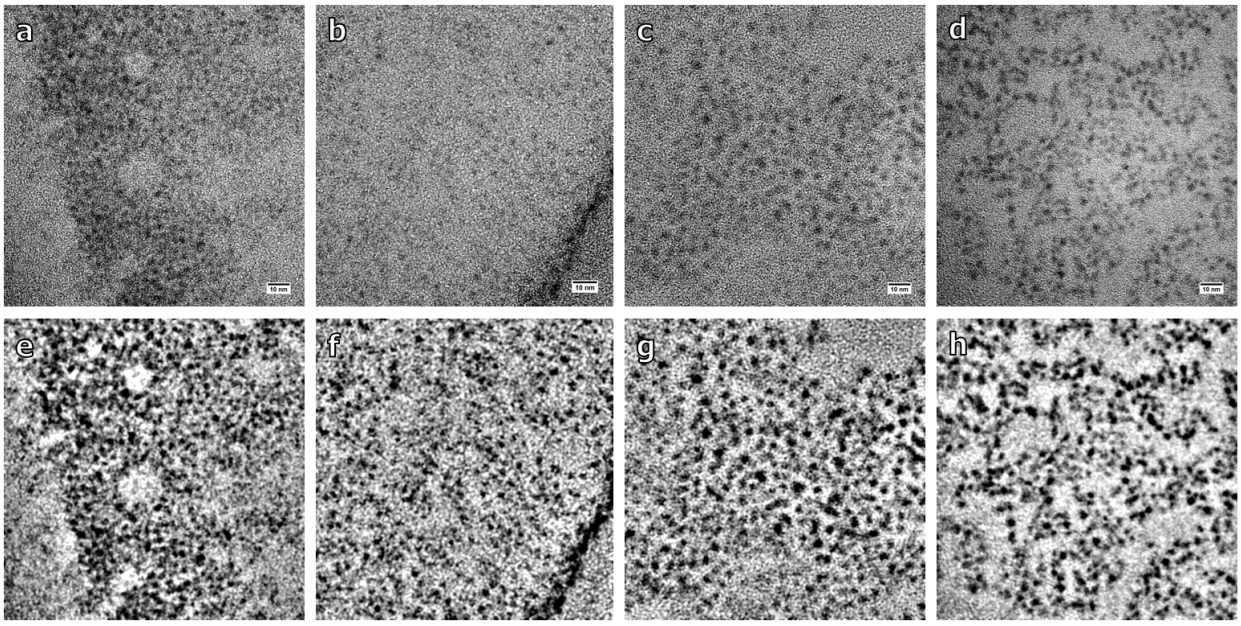


Figure 3.13 - Raw images from TEM (a-d), the scale bar indicates 10nm. Images after processing (e-h) show how quantum dot edges are enhanced relative to the background.

The sample images were identically processed in ImageJ. First, a Fourier transform of the image was created as a bandpass filter. The contrast of the original image was then enhanced by 10%, and the bandpass filter was applied. Finally, the image's contrast was enhanced a further 5%. This processing sequence produced a sharper contrast between the darker quantum dots and the lighter

background relative to the virgin image. For each interdot distance, a measurement line was drawn and the brightness value of the pixel, ranging from 0 to 255, was plotted along that line. Here, an assumption was made that changes in brightness of 2 orders of magnitude or more was determined to be the edge of the quantum dot, with the lower value designated the edge. The distance between pixels was thus taken as the gap between two such changes in pixel brightness. A minimum of 35 measurements were made on each image to ensure statistical significance. These data were then plotted as a box-and-whisker plot in Chapter 4.

3.16 Cyclic Voltammetry Measurements

Cyclic voltammetry was collected using an Ossila Potentiostat and a three-electrode cell consisting of a platinum working electrode, a graphite counter electrode, and a platinum reference electrode. A 0.1 M solution of tetrabutylammonium hexafluorophosphate in dry dimethylformamide (DMF) was prepared under an argon atmosphere as the electrolyte, totaling 10ml.

As an internal reference, 50 mg of ferrocene was dissolved in the electrolyte. The solution was swept from 0 V to 1.5 V, then in reverse to -1.5 V before returning to 0 V, all at a scan rate of 50 mV/s. After collecting the scan, the solution was discarded, and the electrodes as well as the electrochemical cell were cleaned and dried under an argon atmosphere at reduced pressure. Fresh electrolyte was reintroduced into the cell, and 50 mg of poly(dodeca-5,7-diynedioic acid) was dissolved in the solution. An identical scan was run to the ferrocene reference.

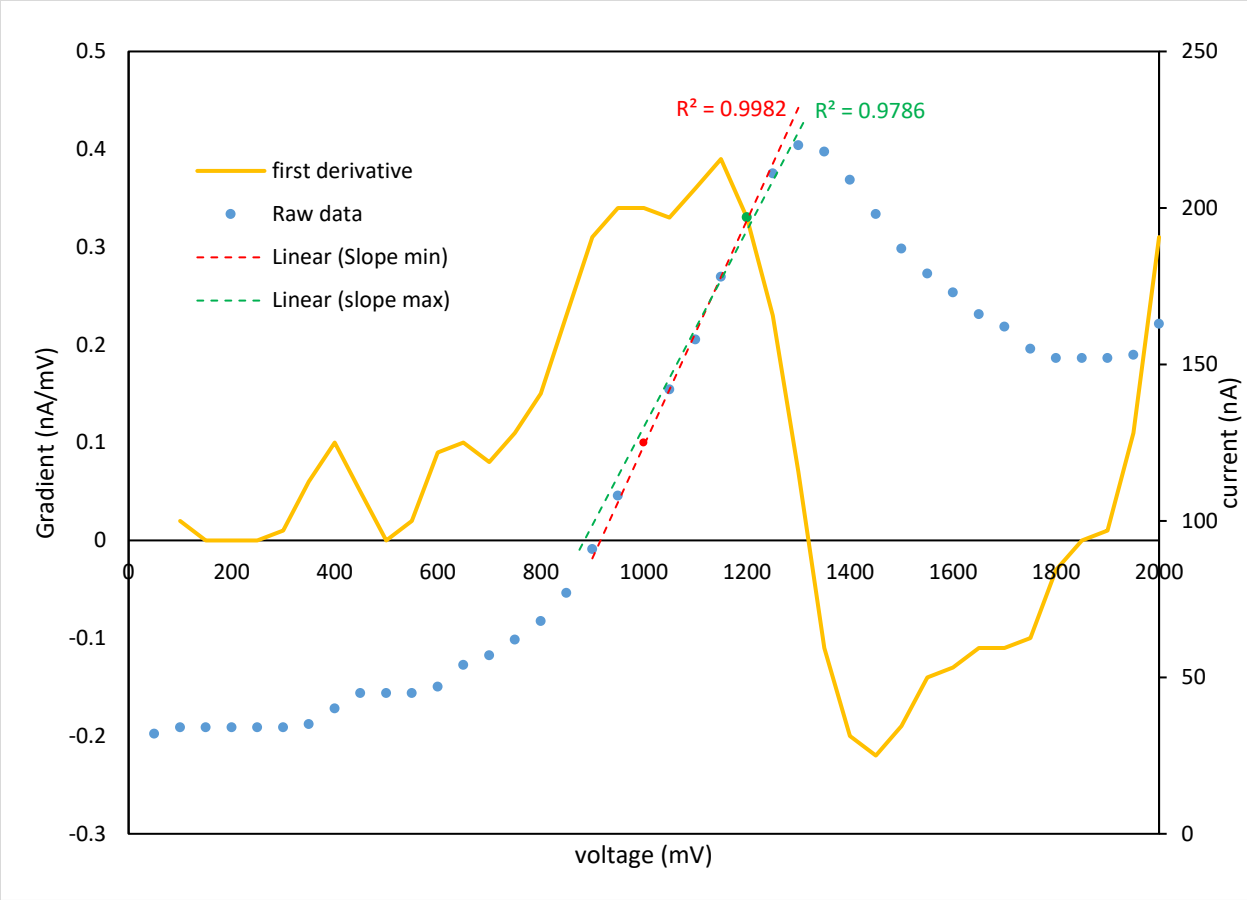


Figure 3.14 – Calculation of the oxidation potential from cyclic voltammetry raw data (blue dots). The first derivative is calculated (yellow line) and the local maximum related to the oxidation peak is found. The slope of the raw data at this point is calculated and extrapolated to the x-intercept to give a reading in mV. Points either side of the oxidation onset (red, green dots) are used to calculate error, compensating for the resolution of the scan. Red and green lines show the maximum and minimum onset potentials, respectively.

The scan results were processed using Microsoft Excel according to the method outlined by Shafiee *et al*. [276]. The oxidation potentials of the ferrocene and the polymer were calculated from a scan's onset of the oxidation peak, located by finding the first derivative's local maximum on the raw data's oxidation peak, as shown in Figure 3.14. A linear fit to the raw data at the oxidation potential was extrapolated to zero current, and the voltage at this intercept was used as V_{ox} or $V_{1/2\ ferrocene}$, respectively, to find the HOMO value in electron volts using the equation:

$$E_{HOMO} = \left[\left(V_{ox} - V_{\frac{1}{2}ferrocene}\right) + 4.8\right] eV \qquad \text{Eq. (25)}$$

Errors were calculated by deriving the slope from points 100 mV on either side of the oxidation onset, then recalculating the HOMO using the minimum and maximum differences between intercept voltages for ferrocene and the polymer.

3.17 Current-Voltage characterization

Fully-fabricated devices were characterized using a home-built setup under ambient conditions. After gold contacting, devices were gently scraped with a razor blade to expose the ITO contact and then masked with vinyl adhesive to produce three 0.015 cm^2 pixels per substrate. These substrates were then loaded into a custom-built contacting rig where each pixel could be isolated for measurement. IV sweeps were performed using a Keithley 2401 sourcemeter controlled by a custom built Labview program. Scans were conducted from -0.5 V to 1 V, starting and ending at 0 V, with a scan rate of 50 mV/s. Measurements in the dark were run by covering the custom-built rig with a fitted metal cap. AM 1.5 G illumination was provided by a Xenon bulb solar simulator after warming up for 30 minutes to reach steady-state operating conditions.

3.17.1 Illuminated J-V characteristics of D57DDA passivated PbS in different device layers

Devices were prepared according to the procedures outlined in sections 3.1-3.6. Three devices were prepared in total; a control device using PbS passivated with TBAI as an absorber layer, and PbS passivated with EDT as a hole-transport layer. The two other devices replaced one of these layers with a PbS layer passivated with D57DDA and irradiated with UV light for 15 minutes per layer deposition as defined by section 3.4. The thicknesses of each layer have been matched, with the D57DDA passivated PbS forming a 7-layer absorber film and a 2-layer hole-transport film. Figure 3.15 shows the J-V sweep of all three devices under 1-sun illumination.

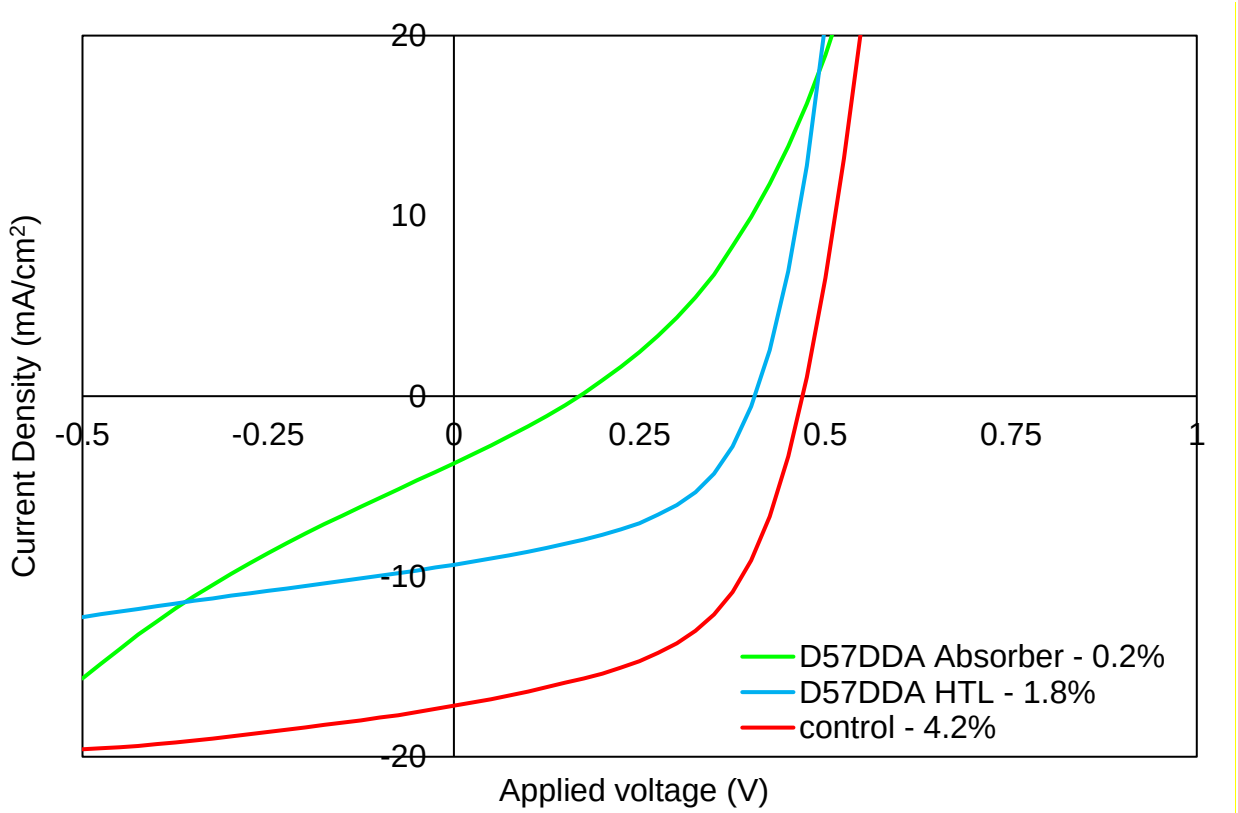


Figure 3.15 - Current-voltage curves showing performance of various cell architectures under 1 sun illumination. Using PbS quantum dots passivated with dodeca-5,7-diynedioic acid (D57DDA) as an absorber layer (green) has a low short circuit current and shunt resistance. Using D57DDA as a ligand for the hole transport layer (blue) has similar shunt resistance and fill factor to the control device (red) but lower overall short circuit current, limiting its power conversion efficiency.

3.17.2 Illuminated J-V characteristics of different hole-transport layers incorporating D57DDA

Devices were made to test the performance of different hole-transport layers in an otherwise standard device architecture. On a TBAI intrinsic layer above the ZnO electron-transport layer and ITO transparent electrode, hole transport layers of PbS coordinated to EDT, *ex-situ* polymerized D57DDA, and PbS coordinated to D57DDA were applied as respective hole transport layers, each totaling 2 depositions thick. An additional cell was made using 1 layer of PbS coordinated with D57DDA, followed by 1 layer of *ex-situ* polymerized ligand. The *ex-situ* polymerization time as well as the UV irradiation time for the ligand exchanged layers were 15 minutes. *Ex-situ* polymerized material was deposited as a polymer in a DMF suspension at approximately

100mg/ml. As before, all D57DDA monomer for both the ligand coordination and isolated polymer layer was produced using the 1-step work up procedure.

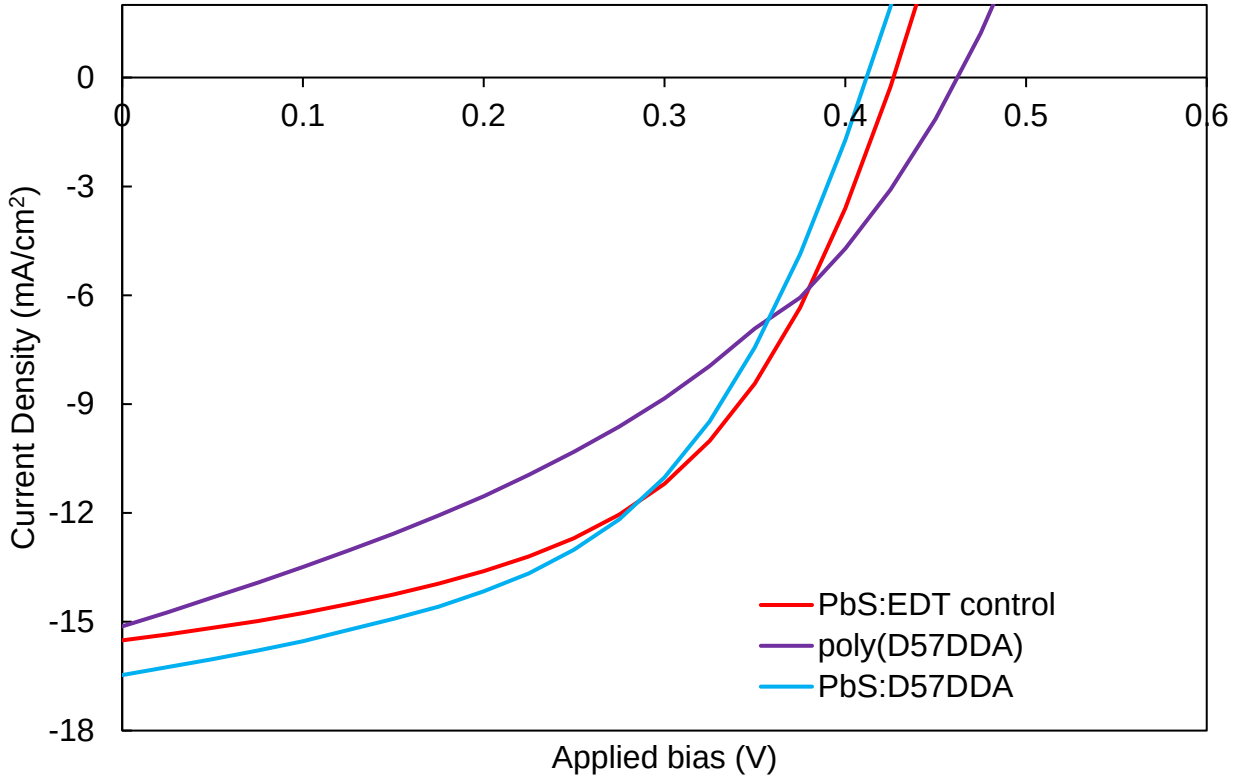


Figure 3.16 - Performance of PbS quantum dot solar cell devices with different hole transport layers (HTLs). Using dodeca-5,7-diynedioic acid (D57DDA) coordinated directly to PbS as a HTL (blue) performs comparably to the EDT control cell (red). The use of poly(D57DDA) as a HTL (purple) has a slightly lower fill factor.

3.17.3 Illuminated J-V characteristics of devices with respect to UV irradiation time

The synthesis of dodeca-5,7-diynedioic acid in Chapter 5 resulted in two separate workup processes used for device fabrication, a 1-step recrystallization and a 2-step recrystallization. To determine the differences in the work-up methods, devices were fabricated with both 1-step and 2-step processes of D57DDA work-up. For each process, separate devices were subject to UV curing times of 0, 5, 15, 30, and 60 minutes. Separate devices with hole-transport layers of EDT passivated quantum dots were UV-cured under the same conditions to control for the effects of UV-curing in air on the quantum dots themselves. J-V sweeps were collected under 1-sun

illumination using the process outlined in Section 3.17. Figure 3.17 shows the J-V plots for all device structures.

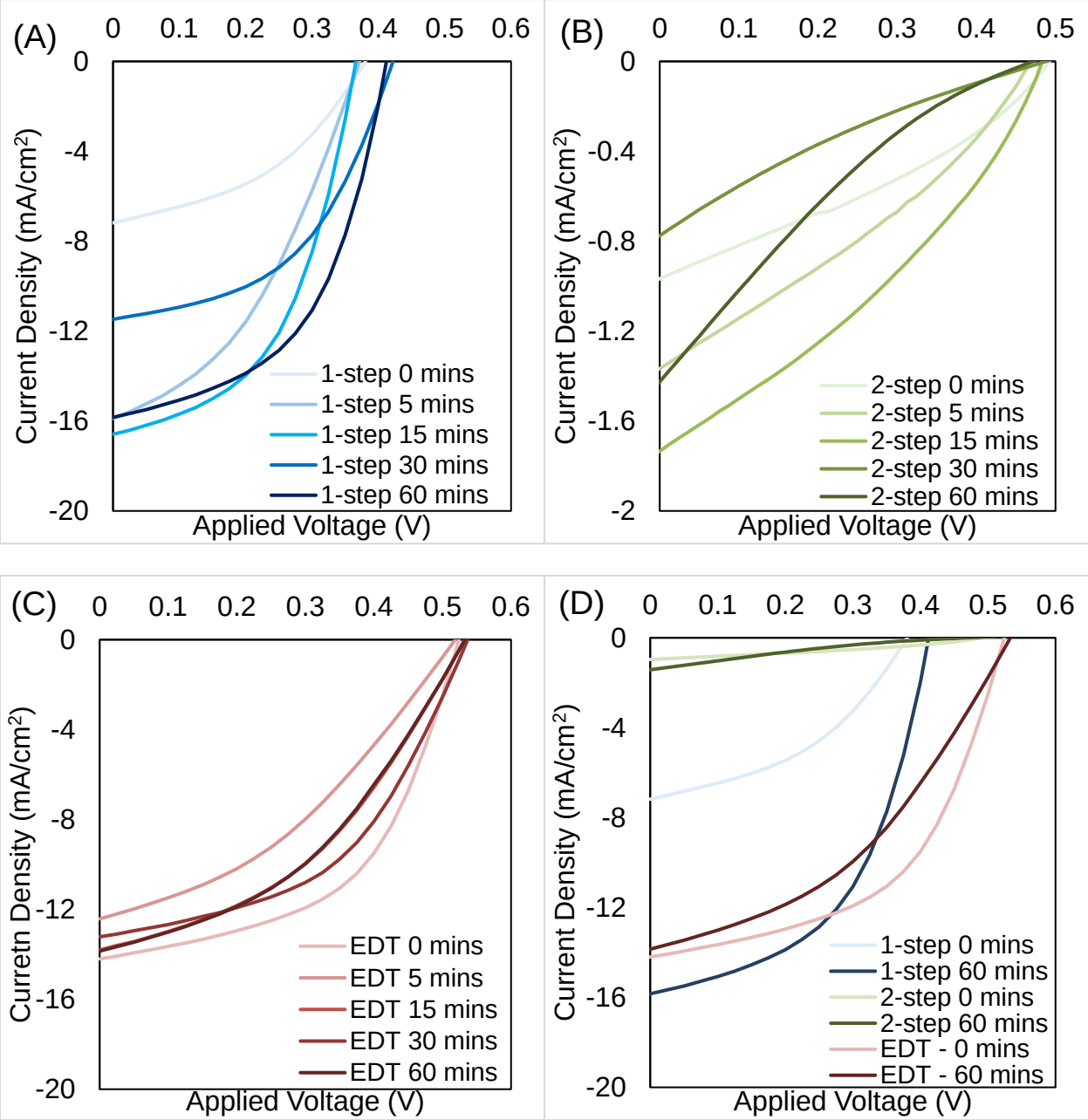


Figure 3.17 – J-V sweeps under illumination of devices after differing times exposed to UV irradiation. (A) shows devices using D57DDA produced using the 1-step work-up method as the hole-transport layer. (B) shows identical devices, using D57DDA produced form the 2-step work up method. (C) shows EDT devices with no polymerizing ligand present in the hole-transport layer. (D) serves as a visual reference comparing devices from all hole-transport layers with before and after 60 minutes of UV irradiation.

4 Coordination of alkyne-based ligands to the quantum dots.

4.1 Introduction

Colloidal quantum dots use ligands to maintain stability in liquid phases, preventing aggregation, and in solid films to maintain their quantum confinement effects. As summarized in chapters 1 and 2, a quantum dot ligand's structure also overwhelmingly dictates its effect on the electronic structure of the film after coordination [277][117], [277]. The ligand's anchor influences its coordination to the quantum dot surface in either an X-type, L-type, or Z-type regime. The level of passivation achieved by a ligand then determines the level of p-doping in the final film [108], [171]. At the other end, the backbone and substituent contribute to the dipole moment of the ligand, shifting the band structure relative to the vacuum level[55], [81], [176]. On rare occasions, the ligand can provide sufficient electron density to n-dope the quantum dot film, however vanishingly few examples of this exist in literature[30], [176], [278]. The substituent also controls how the ligand interacts with its environment, for example, changing the self-assembly properties of the quantum dot or the stability of suspensions in different solvents. One particular class of anchors, terminal amines, have created considerable discussion in literature over their role in lead chalcogenide surface passivation. Conflicting reports show experimental data indicating coordination that run counter to theoretical mechanisms ruling out the possibility of such coordination [55], [108], [188], [189], [279].

The overall aim of this thesis is to produce a proof-of-concept quantum dot thin film with ligands that polymerize *in-situ* to form a conjugated π-system, and then test this material in a solar cell [81], [204], [280]. This chapter works toward the overall goal by examining the ligand exchange dynamics between different anchor groups in the presence of sp-hybridized carbons. Three types of anchor are assessed: the terminal amine, the carboxylic acid, and the terminal alkyne. X-ray

photoelectron spectroscopy is used as a surface analysis technique to examine the bonding regime of carboxylic acids, terminal amines, and terminal alkynes alongside FTIR as a bulk characterization technique and electron microscopy to examine packing structure and chemical composition of films, resulting in a clear picture of the bonding regime and effects on the doping profile of the passivated quantum dot thin films.

4.2 Terminal Amine Ligand Exchange Dynamics

The initial decision to use amine groups was motivated by their use on diacetylene molecules used in biosensor applications and liquid crystals [230], [261], [281]. This indicated that the amine anchor would not react with the diacetylene backbone in the expected final ligand design. Reactivity with the diacetylene backbone is a concern, as demonstrated by the thiol anchoring group. Thiol groups have demonstrated excellent surface passivation ability and improved charge transfer out of the quantum dot experimentally, making them an ideal candidate for the anchor moiety [180], [218]. However, thiol has been shown to react with alkyne groups in a mechanism known as thiol-yne click chemistry, which would destroy the environment required to create extended π-states after ligand polymerization [282]–[285].

Examining the ligand exchange dynamics and surface passivation of terminal amines also presented an opportunity to provide substantial evidence towards the discussion on amine coordination to lead chalcogenide quantum dots in literature. By directly characterizing the coordinating species on the quantum dot using XPS, and using FTIR to examine bulk chemical bonding regimes within the film, strong observational evidence could be added to the open question.

4.2.1 Results

Solution ligand exchange of PbS quantum dots propargylamine was carried out according to the procedure outlined in section 3.5. It was observed that the quantum dots had not aggregated or changed phase to the acetonitrile after phase separation. Subsequently, solution ligand exchange using pure propargylamine was attempted. Propargylamine is a liquid at 25°C and sufficiently polar to stay phase-separated from the octane. The same result was observed, as shown in Figure 4.1. Solid state ligand exchange methods were subsequently attempted according to the methods outlined in section 3.4 using methanol as the solvent for propargylamine. Film deposition was observed after 5 iterations. The subsequent film was characterized using FTIR spectroscopy as outlined in section 3.9 and the resulting Figure 3.3. In addition to the propargylamine film, identical solid state ligand exchange procedures were followed to produce two more films of butylamine and ethanediamine, respectively, as a 1M solution in methanol. X-ray photoelectron spectroscopy (XPS) was used in conjunction with kelvin probe and UV-vis spectroscopy to determine the electronic structure of all three films: propargylamine, butylamine, and ethanediamine. Characterization methods for XPS, UV-vis spectroscopy, and kelvin probe measurements, along with data analysis methods used to produce Figure 4.2 below, are outlined in Chapter 3.



Figure 4.1 - Solution phase ligand exchange with PbS Quantum dots in octane (top) and propargylamine (bottom). The Quantum dots are not moving into the propargylamine phase, or reacting with the propargylamine, suggesting no ligand exchange is occurring.

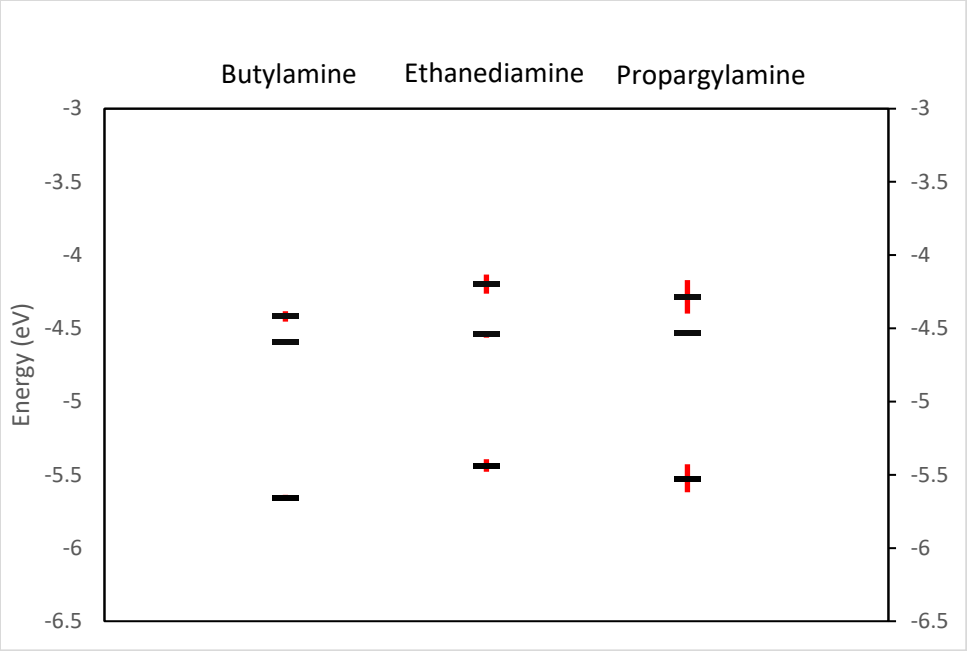


Figure 4.2 - Band positions of PbS quantum dot thin films after ligand exchange from oleic acid to different amines. Kelvin probe measurements to find the work function are layered with XPS to find the valence band position and UV-vis to find the band gap. Error bars, presented in red, are calculated as described in section 3.14.

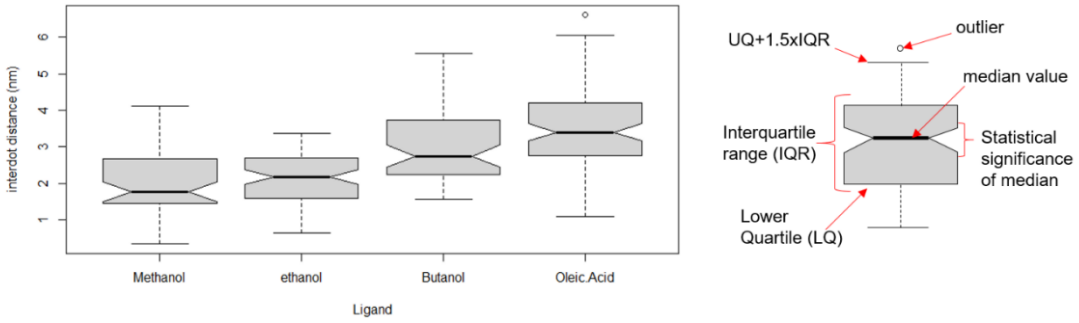


Figure 4.3 - Box and whisker diagram showing the distribution of interdot distances after ligand exchange using propargylamine in different alcohol solvents. Notches that do not overlap show the median value of the two boxes is significantly different.

Figure 4.2 shows that the fermi levels of each film remain nearly constant, however the valence band positions of the films change by up to 0.2eV, a substantial change for such an electronic structure [55], [176].

In support of the previous experiments, three TEM grids of quantum dots after solution ligand exchange with propargylamine in either methanol, ethanol, or butanol were prepared according to the principles outlined in section 3.5. A fourth grid of quantum dots with the native oleic acid

ligand was also prepared using the methods outlined in section 3.15. TEM images were then taken and the distances between adjacent quantum dots calculated according to the procedures detailed in section 3.15. Figure 4.3 shows the distribution of interdot distances across each film as a box-and-whisker plot.

4.2.2 Discussion

Propargylamine was selected as a model terminal amine with an alkyne bond due to it being the shortest alkynylamine. This encourages close packing of the quantum dots and ensures any changes in mobility or band structure would be comparable to other reported short-chain organic ligands.

Solution ligand exchange results strongly suggest that the ligand exchange was unsuccessful, as the quantum dots would be expected to change phase to the acetonitrile phase, or aggregate due to insolubility should the oleic acid be stripped from the surface. It was thus concluded from these observations that solution ligand exchange in acetonitrile between propargylamine and oleic acid was not possible. Similarly, successful solution ligand exchange with pure propargylamine would either cause quantum dots to fall into the propargylamine phase or precipitate out of solution entirely, as the propargylamine-terminated surface would not allow for suspension in the octane phase.

Solid state ligand exchange with methanol yielded thin films that were washed and then characterized by FTIR are shown in Figure 3.3. The figure shows a reduction in the oleic acid's alkyl C-H peak at 2800-3000 cm^{-1} after ligand exchange which indicates oleic acid has been removed from the quantum dots. However, the absence of the terminal alkyne C-H peak at 3100cm^{-1} suggests that the propargylamine is also not present in the film. The ligand's apparent absence from quantum dot thin films is surprising, as there are no other ligands present in the solid-

state ligand exchange system by design. This would suggest that the quantum dots have been stripped of ligands, a suggestion at odds with literature reporting a change in the band positions of quantum dot thin films after ligand exchange with EDA in methanol [55], [286]. Nozik *et al.* suggest amines decouple oleic acid from the PbSe quantum dot surface in methanol, leaving behind a methoxy- group attached to the Pb^{+} site and a lone hydrogen passivating the selenium as shown in Figure 4.4 [188].

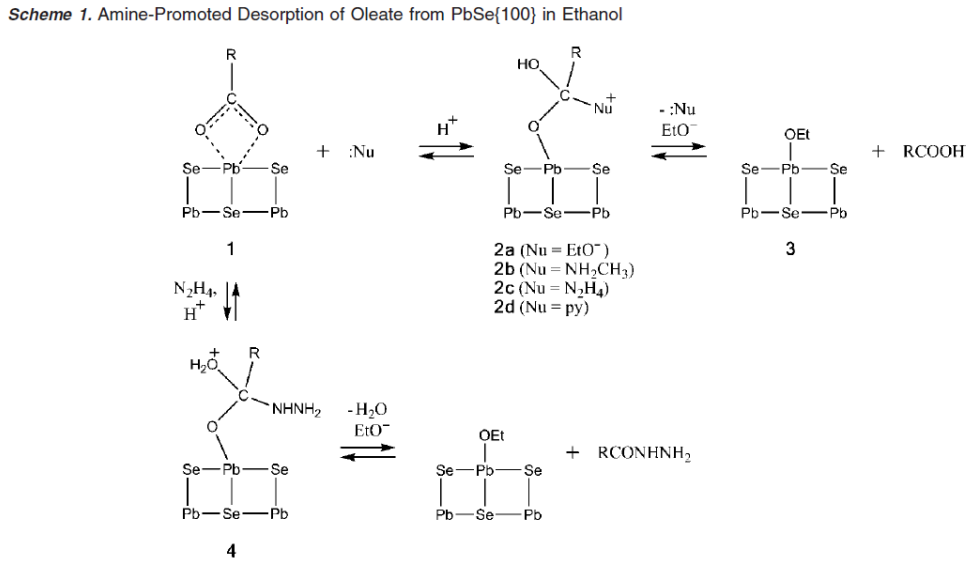


Figure 4.4 - Possible pathways by which amines can coordinate alcohol solvents to the surface of PbSe quantum dots. Given the similar chemistry, experiments were designed to determine the coordination of amines or alcohols on PbS quantum dot surfaces. Reprinted with permission from J. Am. Chem. Soc. 2008, 130, 18, 5974–5985, copyright 2021, American Chemical Society.

Building on this, Hassinen *et al.* report the ability of short-chain alcohols to strip X-type ligands from the surface of PbS quantum dots [189]. Due to these papers and experimental results observed to that point, a new hypothesis was formed. Primary amines were acting as a catalyst to coordinate the alcohol solvent to the PbS quantum dot, as seen in the analogous PbSe work by Nozik *et al.* This hypothesis was supported with previous experiments; no observation of solution ligand exchange would be expected given no alcohols were present in the system. Films were only observed to form during solid-state ligand exchange whilst using alcohol solvents, aprotic acetonitrile did not produce films.

As the amine ligand is hypothesized to be coordinating the alcohol solvent to the quantum dots, the use of different amines would be expected to have overall similar results as long as the alcohol solvent remained constant. Similarly, the same amine coordinated in different alcohol solvents would be expected to yield different results. From this basis, the remaining experiments outlined in section 4.3.1 were planned and executed. As shown in Figure 4.2, the band structure of films ligand exchanged in solutions of different amines in methanol show variances in the conduction and valence bands by 0.2 eV, and significantly smaller variance in the fermi levels. Further, these variances are all within the reported error of the propargylamine band structure data presented, indicating no significant difference within the precision of the measurements. This suggests that the quantum dot surfaces on the different films are similarly passivated and doped. While variation in the band structure could be due to the different amine ligands coordinated to the surface, any small difference observed could be explained due to differing levels of ligand exchange completion with the methanol solvent in the film preparation, leading to different ratios of oleic acid and methoxy groups on the surface and therefore slightly different band positions. Bringing in detailed XPS elemental characterization, the N1s peaks shown in Figure 3.10 would be expected to have different and substantial values for surfaces coordinated with different nitrogen containing ligands. As the N1s peaks are negligible in size and fit to a single peak, it is reasonable to conclude the only one nitrogen environment is present in the films. This is proposed to be diatomic nitrogen adsorbed to the surface of the quantum dots or adventitious carbon. Further, the identical Pb4f, O1s, and C1s peaks in Figure 3.10 all suggest that the environment is not substantially different across the ligand exchanged films with different amines. This strongly suggests that the different amines are not present in the final washed films, and in fact the surfaces are passivated with the identical methanol solvent.

The proposed hypothesis is only strengthened by the TEM image analysis described in section 4.3.1. The interdot distance reported for propargylamine ligand exchange in different alcohol solvents increases with increasing alcohol solvent length. This suggests that a different solvent is coordinated. As the amine remained constant throughout the sample preparation, the solvent must be coordinating to the quantum dots instead, increasing the interdot distances.

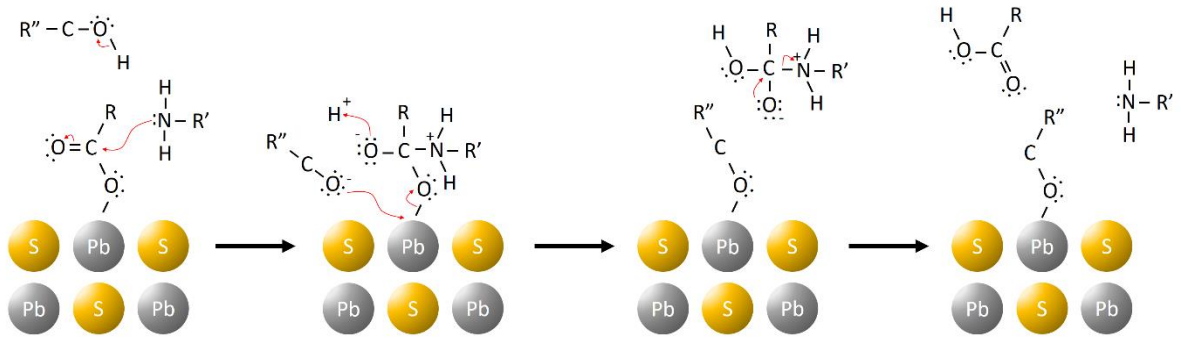


Figure 4.5 - Example pathway by which nucleophile bases assist in the co-ordination of alcohol groups to the surface of PbS quantum dots. Adapted with permission from J. Am. Chem. Soc. 2008, 130, 18, 5974–5985, copyright 2021, American Chemical Society.

Based on the results of the XPS and TEM experiments, it was concluded that amines assist in the coordination of alcohols to the quantum dot surface as X-type ligands. This represents the first time surface analysis and packing structure have been used to arrive at this conclusion, considerably strengthening the argument proposed by Nozik *et al*. [188], [189]. A speculative mechanism for this has been adapted from that work and shown in Figure 4.5. Acting as a nucleophile, the amine initiates the ligand exchange though a backside attack on the acidic carbon. To conserve charge parity, the carbon pushes electrons from its double bond onto the oxygen, which gains a negative charge. Additionally, an alcohol solvent dissociates in the vicinity into a proton and its conjugate base. In the next phase of the ligand exchange, the alcohol's conjugate base then directly attacks the lead surface atom, displacing the oxygen bond of the carboxylic acid and becoming the quantum dot ligand. The recently exchanged oxygen atom picks up a negative

charge. The proton from the dissociated alcohol neutralizes the charge on the other oxygen atom, forming a hydroxyl group. In the final stage, the remaining negatively charged oxygen atom forms a double bond with the carbon, restoring the carboxylic acid and freeing the amine.

It is important to stress that the above mechanism is speculation, and only a representation. For example, after ligand exchange the proton could form a bond with either of the negative oxygen atoms in the second or third stage. Further corroboration of this mechanism is left to future work, where techniques such as cryo-NMR could show the formation of the intermediate complex.

4.3 Carboxylic Acid as an Anchor Moiety for alkyne-based ligands

As the inability of terminal amines to coordinate was experimentally determined, the use of carboxylic acid as an anchor group was subsequently attempted. As oleic acid is also a carboxylic acid and often used as the ligand during PbS quantum dot synthesis, it was concluded that carboxylic acids work as an anchor moiety for PbS quantum dots. Additionally, oleic acid has been used as an anchor for both small organic ligands and large molecules in coupled organic-inorganic nanostructures [136], [137], [287]. As such, it was hypothesized that a small organic molecule featuring a carboxylic acid end group and alkyne-containing backbone would successfully coordinate to the quantum dots in a polar, solvent. Suspension in a polar solvent would be based on the strong dipole moment of the ligand. Maintaining an aprotic solvent would also reduce the chance of the solvent coordinating to the quantum dot, as there would be no dissociation of the solvent into a proton and its conjugate base. 2-butynoic acid was used as the ligand due to its relatively inexpensive cost and small size, to retain some similarity with common ligands in the literature.

4.3.1 Results

Solution ligand exchange proceeded as described in section 3.5 using a 2 M solution of 2-butynoic acid in acetonitrile. Solid state ligand exchange also produced sufficiently thick films for characterization, following the procedure outlined in the section 3.4. Both solid-state and solution ligand-exchanged films were subjected to FTIR spectroscopy, UV-vis spectroscopy, kelvin probe measurements, and XPS surface analysis as detailed in section 3.14. During XPS analysis, detailed scans of the carbon C1s peak were collected to determine changes in the carbon hybridization of the ligands, as described in the methods section and shown in Figure 3.11.

4.3.2 Discussion

The movement of quantum dots to the acetonitrile phase strongly suggests coordination of the new ligand at the expense of oleic acid, which would have rendered the quantum dots insoluble in the polar acetonitrile. That this is seen in solution and solid-state also indicates the exchange happens readily, likely due to the reduced steric hindrance of the 2-butynoic acid on the surface of the dot relative to the oleic acid. This work also speculates that the higher pKa value of butynoic acid leads to a substitution with the oleic acid, though further work on this subject is encouraged to confirm or refute this hypothesis.

FTIR analysis of the ligand exchanged films confirms that the oleic acid has been removed, as the alkyl peak is reduced. An alkyne triple bonded carbon peak emerges, however, it is possible that the quantum dot thin films merely contain the ligand without it being coordinated. Additionally, the effect on the band structure of the alkyne moiety has to be assessed, as there are strong arguments to be made towards both the n-doping and p-doping of the film due to the alkyne. Expectation of n-doping is based on the inclusion of the alkyne bond on the carbon adjacent to the acidic carbon in the ligand, which shifts electron density into the lead surface atoms and

passivating mid-gap trap states. This would move the fermi level closer to the conduction band, n-doping the material via electron donation. However, movement of the work function could be considered to p-dope the material relative to an intrinsic film, as the ligand's strong dipole reduces the work function, raising the entire band structure closer to the vacuum level.

Ligand exchange can be seen when comparing the detailed C1s scan of the different films' XPS spectra shown in Figure 3.11. The ratio change of the sp^3 hybridized component from 17:1 to 2:1 indicates that oleic acid has been removed. Further supporting evidence comes from the removal of the sp^2 hybridized peak and formation of the sp-hybridized peak. The shift in binding energy can also be attributed to the different pendant moiety of the exchanged ligand. As the alkyne bond pulls valence electron density from the acidic carbon coordinating to the quantum dot, this carbon atom in turn pulls electrons further from the influence of this surface lead atom. This lowers the energetic requirement of exciting an electron to the conduction band of the system, making it more n-type in character.

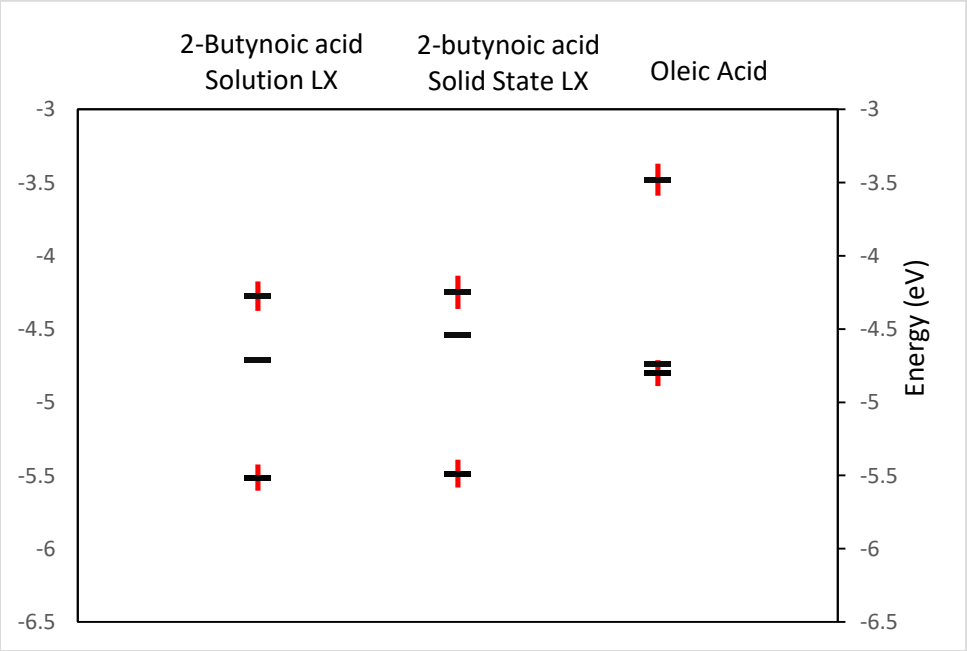


Figure 4.6 - Energy levels of the valence band, Fermi level, and conduction band (bottom to top) of Quantum dot thin films. 2-butynoic acid solid state and solution ligand exchanged (LX) films (left, center) have deeper valence bands

and higher Fermi levels than films using the synthesis ligand oleic acid (right). Uncertainty in the measurements is represented by vertical error bars (red).

Further, detailed valence energy scans were collected to calculate the change in valence band position with respect to an oleic acid film. Figure 4.7 shows the valence band, fermi level, and conduction band positions of each film. The results show that the target alkyne ligands produce a significant shift in the band positions of the film relative to oleic acid, further indicating successful ligand exchange. Further, the position of the fermi level relative to the valence band and the vacuum level in the 2-butynoic acid coordinated film indicates the relative strength of the conflicting mechanisms hypothesized above. The proximity of the fermi level to the conduction band shows that the ligand exchanged film is of n-type nature, as opposed to the p-type nature of oleic acid. This is speculated to happen via the following mechanism: Electron density is high in the triple bond, due to the high number of electrons involved and the short bond length relative to sp^3-hybridized carbon bonds. As such, electrons will look to spread into the oxygen-lead bond of the ligand via the acidic carbon in the carboxylic acid, as the hybridization of the alkyne and acidic carbons means there are orbitals in the same plane above and below the bonded atoms. Increased electron density at lead sites on the quantum dot surface would then fill trap states in the quantum dot band structure, making it more likely that an electron is found closer to the conduction band as a result. As this is represented by the fermi level moving closer to the conduction band, the resulting film develops an n-doped profile.

This result is significant as it expands the library of n-type ligands available, and invites future research into the use of alkyne bonds and conjugated systems as an integral component of ligands designed to deepend the valence band position.

4.4 Coordination of Terminal Alkynes to PbS Quantum Dots

In order to thoroughly examine the options for alkyne-based ligands, the use of terminal alkynes as an anchor moiety was examined. Terminal nitriles containing sp-hybridized carbon with a nitrogen atom have previously been shown to coordinate with quantum dots [55]. The nitrile bonds via the nitrogen's non-bonding electron pair to the Pb^+ on the surface of the quantum dot, as an L-type ligand[108], [171], [288]. This is in contrast to ligands such as thiols or carboxylic acids, which lose their terminal hydrogen to bond to the Pb^+ as an X-type ligand. The hydrogen then bonds to a free sulfur on the surface to passivate it as a Z-type ligand. As discussed in section 2.4, different ligand bonding types will passivate different defects on the PbS quantum dot surface. Of these, X-type ligands are considered the most important due to their passivation of Pb^+ surface atoms, which can act as a mid-gap trap state. A terminal alkyne would be expected to coordinate as an X-type ligand, with the hydrogen dissociating from the triple-bonded carbon to leave an electron pair. This would then coordinate to a Pb^+ surface atom in a similar manner to a terminal amine or thiol.

4.4.1 Results

Solution ligand exchange was attempted as outlined in Section 3.5 using a 1 M solution of phenylacetylene in toluene. Ligand exchange via this method could not be concluded due to the miscibility of toluene and octane. Subsequently, solution ligand exchange was attempted under the same experimental procedure, using pure phenylacetylene as the coordinating immiscible phase. After mixing the solvents and subsequent phase separation, no precipitation or ligand exchange of quantum dots was observed.

4.4.2 Discussion

The initial hypothesis was that a terminal alkyne would behave as the Z-type ligands, with dangling bonds on the surface of the quantum dot coordinating to the carbon at the expense of the terminal hydrogen. Phenylacetylene, shown in Figure 4.7, was chosen due to the aromatic ring having a characteristic signature in FTIR experiments, making its detection in any prospective film simpler. Solution ligand exchange with pure phenylacetylene was anticipated to show ligand exchange through movement of quantum dots into the phenylacetylene solution. Alternatively, if the phenylacetylene coordination produced an insoluble quantum dot complex, precipitation from the octane solution would indicate successful coordination. However, no precipitation or movement into the phenylacetylene phase was observed, indicating that no ligand exchange has taken place.

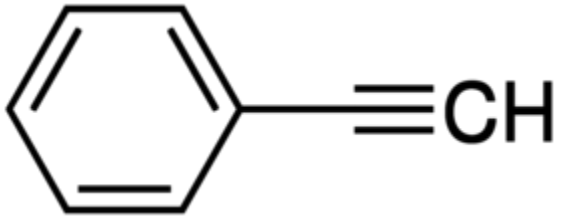


Figure 4.7 - Molecular structure of Phenylacetylene

The lack of ligand exchange by and coordination of the phenylacetylene can be attributed to a lack of possible coordination mechanisms for the molecule. The nature of ligand exchange is to form a chemical bond with the surface of the quantum dot, most ligands achieve this by dissociating in solution into conjugate acidic and basic ions. The clearest example of this is carboxylic acids and halides, which deprotonate to form L-type anchor moieties, as shown in Figure 4.8. This dissociation can be achieved by placing the ligand in a sufficiently polar solvent, such as acetonitrile or methanol. Looking at the phenylacetylene molecule, there are no clear candidate bonds for such dissociation; the hydrogen on the terminal alkyne is bonded too strongly to the carbon for removal under neutral conditions in a polar solvent. Indeed, phenylacetylene is not soluble in most polar solvents. Introduction of a base to deprotonate the terminal alkyne hydrogen

may be a possible solution to allow the formation of a dative bond at the sp-hybridized carbon site, however this would introduce additional species into the ligand exchange solution that may preferentially coordinate to the quantum dot. For example, the thiocyanide ion used by Murray *et al*. coordinates to the quantum dot on the sulfur lattice sites, even though the nitrogen has a nonbonding pair of electrons [289]. As such, no path for terminal alkynes as anchor moieties was seen and their use was abandoned.

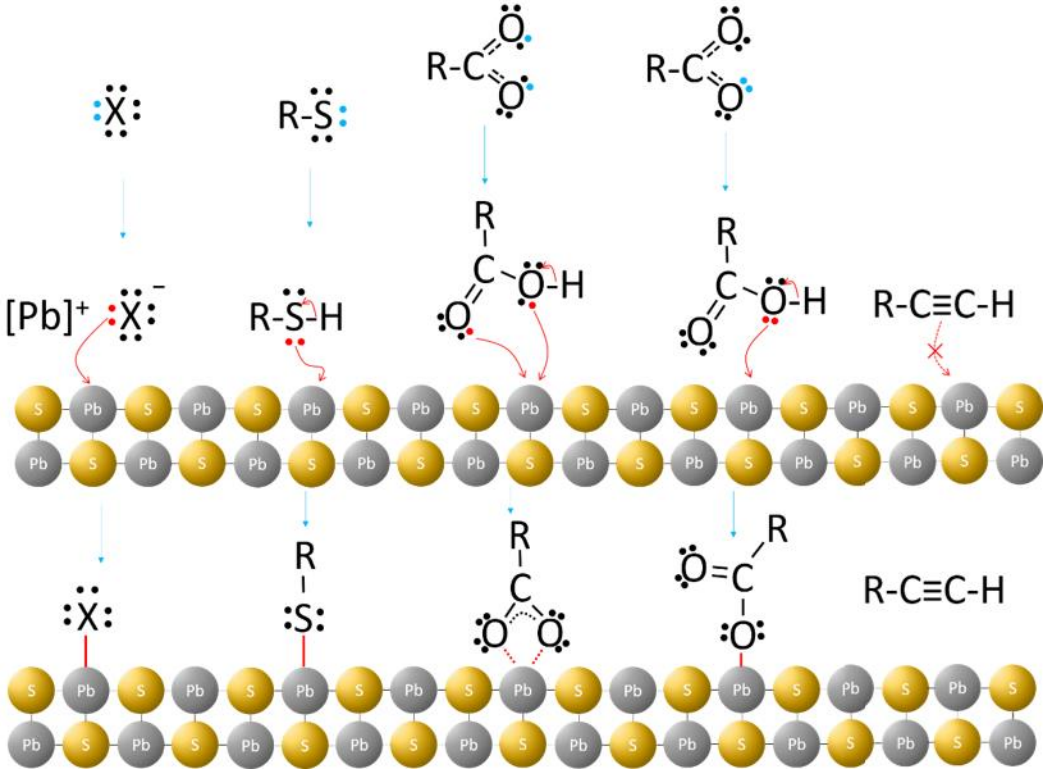


Figure 4.8 - Formation of conjugate bases and proposed coordination methods of common literature anchor moieties. From left: halide ion (PbX), Thiol, Carboxylic acid (L-type), Carboxylic acid (X-type). On the far right is the terminal alkyne, showing its inability to deprotonate and coordinate using the nonbonding electrons and as such is unable to act as an anchor moiety.

4.5 Conclusions of Chapter 4

This chapter's work has examined the ligand dynamics at PbS quantum dot surface, with the intent of modifying a quantum dot band structure by coordinating an alkyne ligand. It was shown that neither terminal alkynes nor amines coordinate to PbS quantum dot surfaces. When using alcohol solvents, it was shown using surface analysis and quantum dot packing structures that amines in

alcohol solvents will coordinate the alcohol to the quantum dot in favor of native synthetic ligand such as oleic acid by way of a nucleophilic substitution reaction. Finally, the work shows that coordination of short-chain alkyne carboxylic acids is possible, and that the ligand n-dopes the resulting quantum dot thin film as a result of increased electron density on surface lead atoms.

The use of surface chemistry to show that amine ligands do not coordinate to the surface of PbS quantum dots means this work helps to settle a debate in the literature over the nature of a common anchor ligand. Further research into the exact mechanism by which amines coordinate alcohols to the quantum dot would lead to greater understanding of ligand surface dynamics and subsequent passivation breakthroughs, for example the use of sulfides to increase sulfur stoichiometry as a method of n-doping. Direct evidence of n-doping via the coordination of 2-butynoic acid also demonstrates an addition to the library of n-type ligands to quantum dots, a significant addition to the field. This builds on the work of Kirmani, Giansante, and Mastria using neighboring high-bandgap or electron-rich materials to fill trap states in the electronic structure of PbS as a passivation mechanism [30], [215], [216], [290]. Using the polarity of the ligand and conjugated ligands close to the anchor moiety to achieve the same effect greatly increases the potential library of n-doping ligands, and further research into this effect is encouraged. This addition to the ligand library on its own could lead to novel implementations of quantum dot structures such as cascaded junctions or quantum wells as shown in section 1.3.3 [58], [59].

Within the context of this thesis, the work presented above provides a solid foundation on which to design a diacetylene ligand for solid-state polymerization. The research shows alkyne backbones can be coordinated using the carboxylic acid anchor moiety, and can be expected to n-dope the resulting quantum dot film. This suggests that the final design of the ligand will work well as the n-type layer in a p-n junction, using conventional ligands such as EDT as the p-type layer. The

work presented also indicates that having a high level of conjugation chemically coupled to the surface of the quantum dot may passivate trap states on the surface, leading to an increase in the mobility of the final material beyond the expected gain of including transport pathways in the polymer itself.

5 Synthesis and Coordination of Diacetylene Ligand

5.1 Introduction

The role of the ligand anchor in passivating the surface of a quantum dot was examined in chapter 4. Carboxylic acid was shown using FTIR and XPS spectroscopy to coordinate to the PbS quantum dots and, in conjunction with an alkyne backbone, exhibited n-type doping. Building on the work from chapter 4, this chapter looks into the design and characterization of a novel polymer for use in a quantum dot solar cell.

The purpose of the polymer is to improve the mobility of the quantum dot layer in the solar cell, using three overlapping methods. Firstly, π-stacking of the ligands in monomer form will influence how adjacent quantum dots organize, as the π-stacking interaction is expected to extend across ligands on multiple quantum dots. This results in long range order within the quantum dot thin film, increasing the probability of overlapping quantum dot wavefunctions and leading to band-like transport [83], [84].

Secondly, topochemical polymerization of the π-stacked ligands will lead to the formation of extended π-states in the material. Extended π-states adjacent to the quantum dots is expected to improve charge transport for holes in the material, as charge transfer from quantum dot to polymer reduces the rate of recombination in quantum dots and provides a high-mobility pathway through the material. This approach has been shown to work by Ortiz-Cervantes in 2D perovskite materials, indicating this approach is feasible [225].

Charge transfer between organic and inorganic layers will be enhanced by the third method of improving mobility – direct coordination between quantum dot and polymer. By coordinating the monomer to the quantum dots and then polymerizing *in-situ*, the number of chemical bonds between quantum dot and polymer will be considerably higher than if the organic and inorganic

components were combined *ex-situ*. This increase in chemical coordination between polymer and nanocrystal has been shown by Kochemba *et al* using Poly(3-HexylThiophene) and PbS quantum dots to increase the rate of charge transfer between organic and inorganic semiconductors [71]. Charges can be separated across the quantum dot-polymer interface, allowing for hole transport via the polymer instead of the quantum dot, similar to the approach of coupled organic-inorganic nanostructures (COINs) used by Scheele [81], [105], [136]. In these COINs, one of the ligand's HOMO or LUMO is designed to lie at the same energy as the quantum dot's valence or conduction bands, respectively. The result is dramatically improved charge transport of one charge in the material. However, these systems still use the quantum dot as part of the transport system, which allows trap states to affect the final mobility of the device.

By using a polymer with an extended π-system, this work aims to avoid quantum dots during hole transport. The general tactic of improving mobility via charge transfer to an extended π-system has been demonstrated by Kim *et al*. using graphene flakes, and later by Tazawa *et al.* using carbon nanotubes. [220], [221]. However, the addition of carbon allotropes into the quantum dot thin film destroys the environment for long-range quantum dot order. Using a topochemical polymerization would preserve that environment. Strong coordination will also stabilize the mixed organic and inorganic phases, a documented issue in the formation of blended hybrid photovoltaics [118], [146], [147], [215].

The majority of cases in which polymer is used in quantum dot solar cells is as a hole-blocking layer due to their comparatively wider band gaps compared to common quantum dot thin films [54], [68]. Favorable alignment of the wide band gap to the quantum dot valence or conduction band suppresses mid-gap trap states in the quantum dot thin film, improving the lifetime of charge carriers.

The identification, design, and synthesis of a polymer system capable of all these effects is the main aim of this chapter. Building on the techniques from Chapter 4 to demonstrate ligand coordination and its effect on the band structure, this polymer system will then be coordinated into quantum dot thin films.

5.2 Ligand Requirements

Before synthesizing the ligand, it is important to consider its design from an optoelectronic and chemical perspective. The central aim of the ligand is to polymerize and form an extended π-system that improves the mobility of charges in the quantum dot thin film. The mobility of holes is generally reported to be lower than that of electrons, therefore the greatest benefit will be the improvement of the hole mobility [291]. As such, the polymer should have a hole mobility higher than that of a quantum dot thin film, reported to be on the order of 10^{-4} $cm^2V^{-1}s^{-1}$ and 10^{-5} cm^2 $V^{-1}s^{-1}$ for EDT and TBAI passivated films, respectively [185], [292]. The band gap of the material and its positions must also be carefully selected, so as not to lose the benefits of the 0D system's quantum confinement. This is what allows graphene and carbon nanotubes to be used for electron transport: despite the alignment of the carbon allotrope's LUMO with the conduction band of the quantum dot, the band gap is sufficiently large to not align with the valence band [220], [221]. It is well documented that quantum dots can tune their band positions by over 2 eV through the use of ligand passivation [280]. However, as the polymer will be directly coordinated to the quantum dots, band position control through additional ligand passivation will not be an option. As such, the focus is put on the band gap of the polymer. A band gap wider than 1.7 eV would guarantee a 0.3 eV offset between the polymer LUMO and the quantum dot conduction band, given the largest band gap reported in PbS quantum dots is 1.4eV [28], [293]. Finally, the positions of the polymer's HOMO and LUMO must be taken into account with respect to the quantum dot energy levels.

Band alignment is critical for efficient charge transfer, given that the polymer is being designed to transport holes, the position of the HOMO should be close to the valence band of the quantum dot. Several reports from literature indicate that a 0.2 eV difference would be a suitable upper bound [215], [217]. Any polymer with the proposed optoelectronic characteristics must also be able to polymerize in the solid state in order to achieve *in-situ* polymerization. This could be done with the use of an initiator or the use of an external source. However, the ligand anchoring group must not interfere with this polymerization.

After considering the chemical and optoelectronic properties of the material, polydiacetylene is selected as the ideal polymer for this application. From an optoelectronic perspective, polydiacetylene has a band gap of 2.2 eV, far surpassing the 1.7eV threshold to guarantee a band offset and maintain quantum confinement [266]. Reported mobilities in polydiacetylene are also on the order of 10^{-2} cm^2 $V^{-1}s^{-1}$, an order of magnitude greater than that of quantum dot thin films [294], [295]. Chemically, polydiacetylene is capable of topochemical polymerization in the solid state. Crucially, this does not require the use of initiator compounds [251], [253]. Polydiacetylene is further suited to this application in PbS quantum dots as the optimal monomer spacing and configuration for topochemical polymerization matches the lattice spacing of PbS closely [264].

5.3 Ligand Design

The structural design of the proposed ligand monomer can be broken down into three parts: the anchoring group, the diacetylene moiety, and the link between these two components.

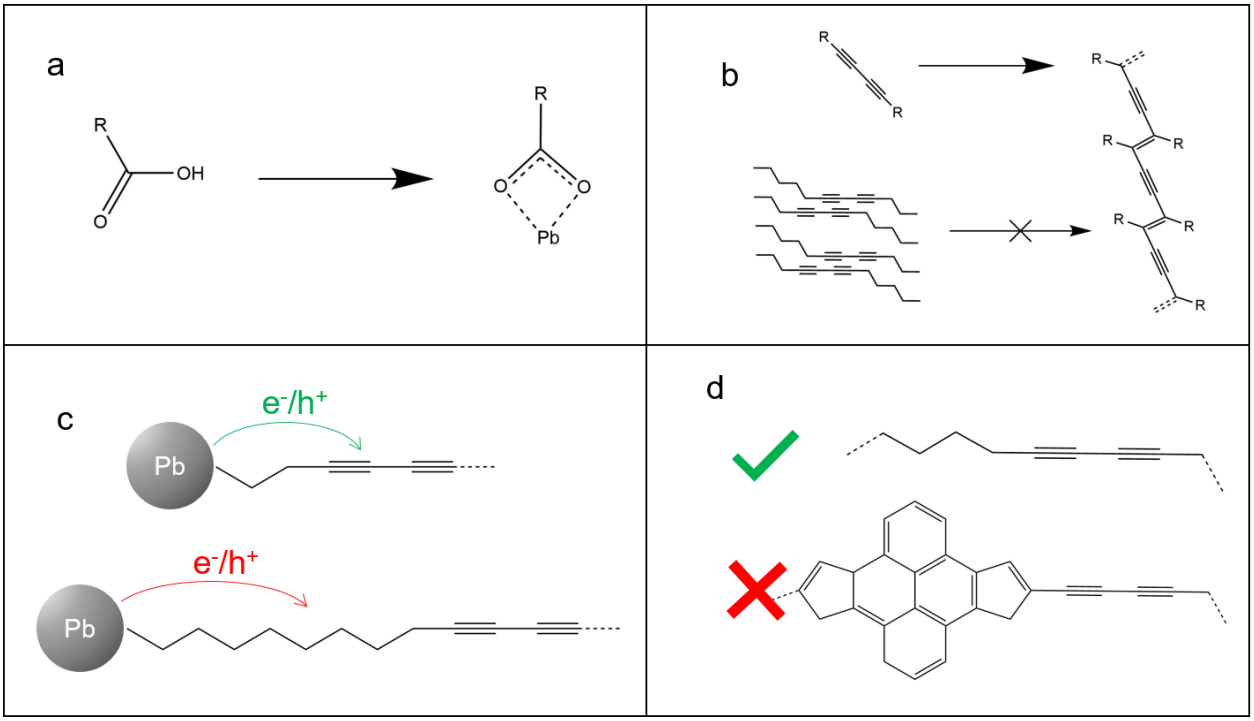


Figure 5.1 - Design principles of the ligand capable of in-situ polymerization. The ligand should a) have carboxylic acid as an anchor moiety to coordinate to the quantum dots, b) include a polydiacetylene moiety to allow topochemical polymerization without the need for molecular initiators or specific polymerization conditions such as extreme heat, c) a linking moiety between the diacetylene and anchor that is short enough for charges to transfer across, and d) a moiety simple enough to be made such that the concept can be proven, and synthesized.

The design process for the diacetylene ligand, illustrated in Figure 5.1, started with the anchor moiety. Of the classic anchoring groups and passivating ligands, it was established from Chapter 0 that a carboxylic acid functional group would be the most suitable anchor moiety. The backbone of the ligand was based on a diacetylene due to the topochemical polymerization phenomenon, discussed at length in section 2.5.1, and the resulting polymer creating extended π-states by way of its conjugated backbone. [105], [255], [257], [296].

The placement of this diacetylene within the ligand must also be carefully planned, the topochemical polymerization requires a specific packing structure of the diacetylene chains [250]. It has been shown by Ortiz-Cervantes that ligands with a single anchor can self-assemble in an interdigitating fashion in 2D systems [225]. However, for a 0D quantum dot system, there is no guarantee of straight lines where interdigitating self-assembly can occur. As such, the conditions

for topochemical polymerization must be designed to achieve the greatest amount of mechanical coupling between organic and inorganic systems [280]. To this end, it was decided that the ligand would be made symmetrical and bifunctional. Symmetry was considered an important design component, as the orientation of the ligand upon coordinating to two separate quantum dots will not affect the alignment of the diacetylene moieties in the space between, illustrated in 5.1b.

The final point on the design of the ligand is the connection between the anchor and the diacetylene. Whilst the inclusion of a more complex, conjugated system in the linker moiety might increase the rate of charge transfer between the quantum dot and extended organic states, as discussed in section 0, it was decided that the link between the diacetylene and the carboxylic acid anchor should be simplified as much as possible with respect to synthesis. As such, an optically inert alkyl chain was chosen as the linking moiety between anchor and backbone. Based on this design selection, the length of the alkyl chain must also be considered. Large, flexible regions between the diacetylene moiety and the anchor group could produce too large a gap for effective electronic coupling, inhibiting charge transfer and overall film performance[119] . However, short bifunctional ligands may also coordinate to multiple sites on the same quantum dot, which would inhibit the ordering of the diacetylene centers [53], [185].

Taking into account all of the design considerations above, the diacetylene ligand selected was a symmetrical diacetylene with the dicarboxylic acids separated from the diyne by 4 alkyl units. The dodeca-5,7-diynedioic acid molecule is shown in Figure 5.2.

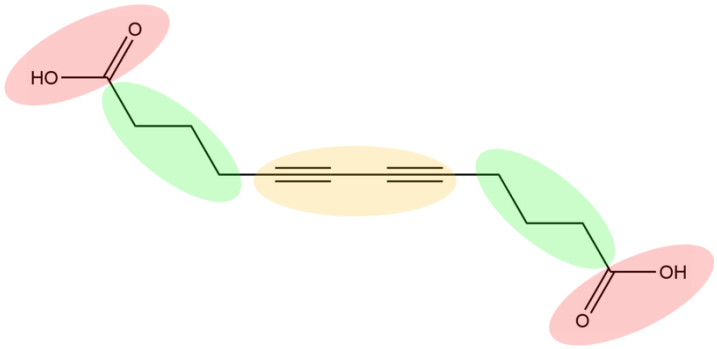


Figure 5.2 - The designed ligand, dodeca-5,7-diynedioic acid. Key parts of the ligand are the carboxylic acid anchor (red shading), the diyne backbone (yellow shading) and the 4-carbon alkyl chain (green shading) to connect the backbone and anchor.

5.4 Synthesis of dodeca-5, 7-diynedioic acid

Having designed the diacetylene ligand, its synthetic realization must be planned with an aim towards reduced resource consumption and simplicity. The synthesis needs to have a high atom economy - the number of atoms in the reactant that are also present in the product – to reduce the number of byproducts formed from the reagents [297]. Additionally, a large number of reaction steps can lead to increasingly low yields, with separation processes between steps further compounding this issue. Ideally, the reaction would require a single step with high yield. Finally, the reagents used for the reaction should be safe to handle and store. This makes the reaction safer to conduct in a laboratory setting, and in a scaled environment should the material be commercialized.

Having laid out the constraints of the process, terminal alkyne coupling was deemed to satisfy all of the imposed conditions [298]. In addition, by having a symmetrical final product, the coupling does not have to preferentially direct to a specific product [236].

An alkyne homocoupling based on the Koevoets reaction was found to fit all of the criteria proposed [243]. The reaction was then carried out as written in section 3.7. Monitoring of the reaction by thin layer chromatography showed the reaction proceeding, and Raman spectroscopy shown in Figure 3.7 of the final reaction mixture showed a peak shift from alkyne reagent to diyne

product. Further, exposure of the dried product to ultraviolet light caused the onset of a characteristic carbon-carbon double bond peak in the Raman spectrum, as well as a visual color change from white to red.

Cyclic voltammetry of the polymer was used to calculate the HOMO level and give greater insight into the band gap of the polymer. Experimental methods and calculations of the band gap are given in section 3.16. The determined level of the HOMO relative to vacuum was found to be -4.70 eV.

5.5 Discussion

The red-shifting of the UV-vis peak with increasing UV curing time seen in Figure 3.6 indicates the formation of a conjugated π-system, as the HOMO-LUMO gap shrinks with a lengthening of the conjugated polymer chain. This is supported by the visual white to red color change of the material after UV irradiation. Additional energy levels are formed in the system as more monomers couple to form the polymer, and this is responsible for this shrinking energy gap [299].

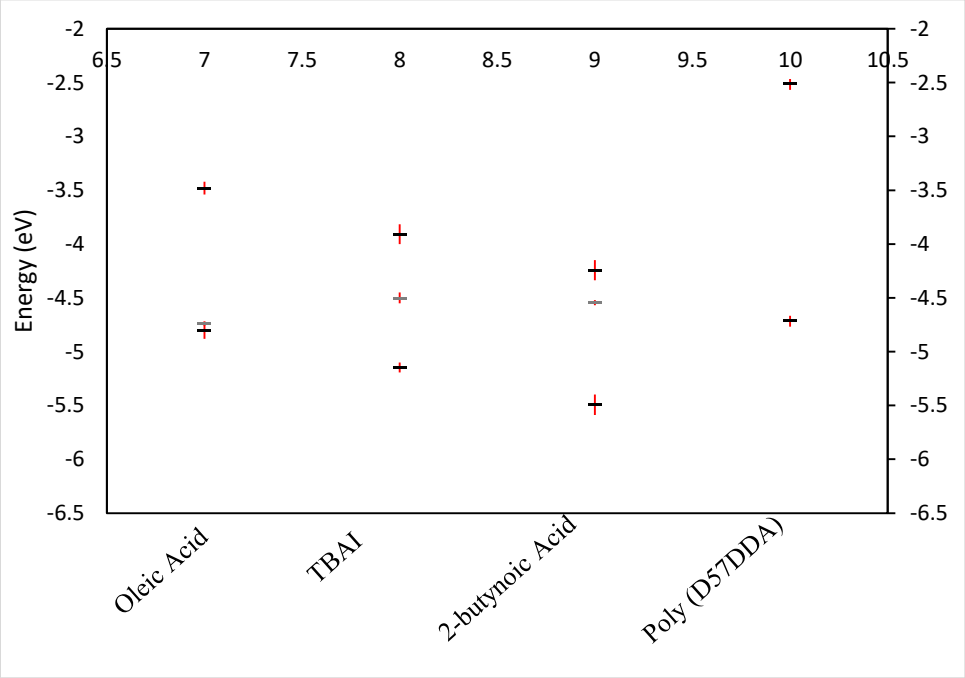


Figure 5.3 – Band position poly(D57DDA), right, as determined by cyclic voltammetry to find the HOMO, and UV-vis spectroscopy to find the band gap. The LUMO is considerably shallower than the conduction bands of quantum dots coordinated with oleic acid, tetrabutylammonium iodide, or 2-butynoic acid (respectively, from left). Error bars (vertical, red) show the range of uncertainty for the values and have been calculated using the method outlined in section 3.16.

The final band gap of 2.2 eV matches the expected literature value of 2.2 eV, indicating that the polymer formed is a poly(diacetylene) [266]. Cyclic voltammetry measurements gave a HOMO level of -4.7 eV. In conjunction with the UV-vis data, this result places the LUMO of the polymer at -2.5 eV. The resulting band structure is relatively shallow compared to the reported band positions of quantum dots coordinated with the more common ligands for solar cell fabrication, as shown in Figure 5.3. Indeed it is significantly shallower than the HOMO level of -5.1 eV reported by Parry *et al*. [266]. This 0.4 eV gap is concerning, as it is outside the proposed 0.2 eV range for efficient charge transfer. The implication of such a gap are poor charge transfer to the polymer, which would result in higher SRH recombination and therefore lower charge mobilities.

However, this result and the literature value both indicate that the polymer would be a good hole-transport layer in a quantum dot photovoltaic device, as the high band gap and shallow HOMO would selectively block electron transfer to the cathode. The shallow HOMO position also raises the question of what effect the polymer will have when coordinated to the quantum dots in a homogeneous film. As the amount of quantum dot by volume will far surpass the polymer, the final band positions of a polymer-coordinated quantum dot should be closer to that of the native quantum dots than the polymer according to Vegard's law of mixed solids [300]. Additionally, coordination of the alkyne ligand from chapter 4 demonstrated n-type doping, this further suggests that the coordinated polymer-quantum dot thin film will have deeper conduction and valence bands than the stand-alone polymer, if following Vegard's law. However, it is important to note that Vegard's law is based on the interaction of crystalline solids, not the hybrid combination of disordered semiconductors likely to exist in this film, therefore it is unlikely to apply in this context.

Verification of the polymer's overall suitability from an electronic standpoint would need to be further characterized, as the 0.4 eV difference between this work and the literature value is considerable. Most notably, cyclic voltammetry measurement of the LUMO [276] in order more accurately compare the band positions to literature values. Further, determination of an upper bound on the polymer's mobility is recommended through the construction of a field-effect transistor (FET) [198].

5.6 Coordination of ligand to quantum dots

Having made the target ligand – dodeca-5,7-diynedioic acid, and demonstrated that it has the band gap and topochemical polymerization properties expected, its ability to coordinate to quantum dots was examined. Solution ligand exchange was not considered as the molecule is bifunctional, and this would lead to aggregation of the PbS QDs in solution, rendering it unable to coat a substrate. As such, solid state ligand exchange using the procedures outlined in Chapter 3 were used. Acetonitrile was used in place of methanol to avoid the coordination of the solvent to the quantum dots, as noted in Chapter 4. As acetonitrile is polar but aprotic, it does not have the ability to form the X-type ligand system that could coordinate to the PbS surface.

Coated substrates were placed under UV irradiation for differing periods of time after the washing stage of each layer deposition. Separate substrates were subjected to UV irradiation times of 0, 5, 15, 30, and 60 minutes to determine if the length of curing time affected the degree of polymerization within the final film.

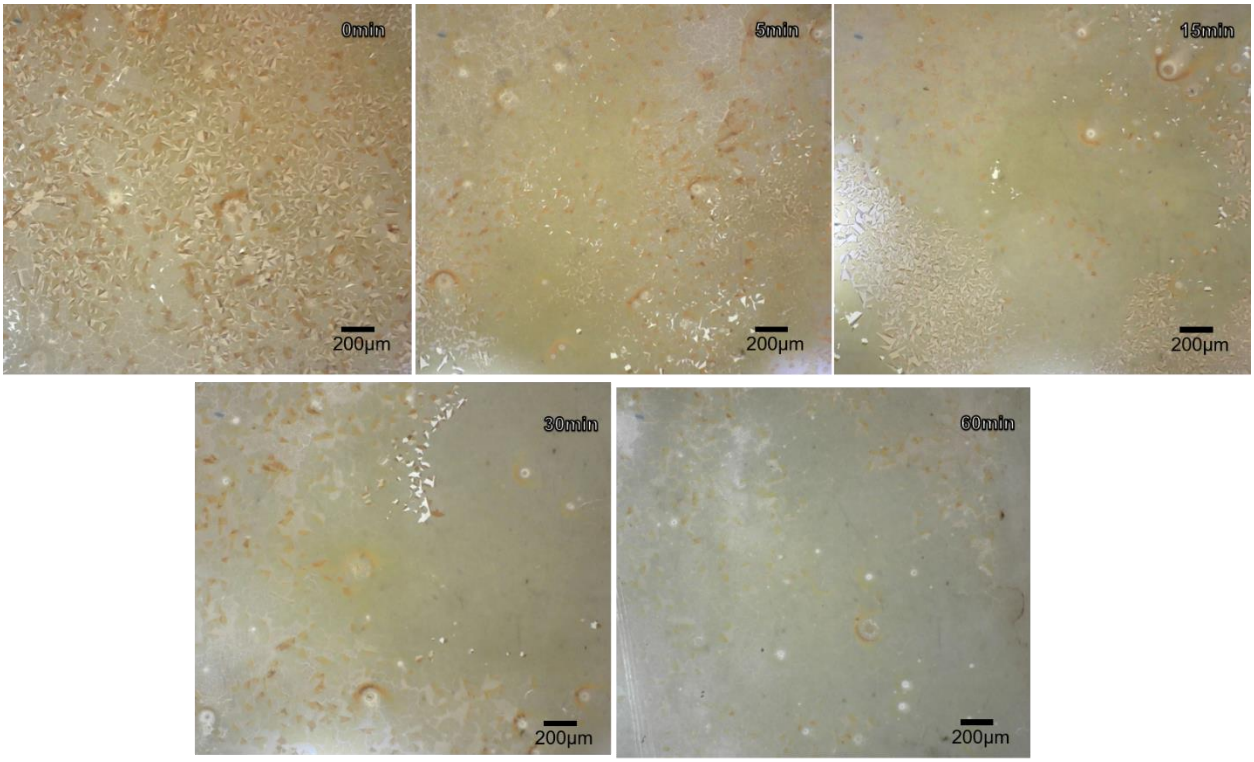


Figure 5.4 - Optical microscopy images of PbS films coordinated with dodeca-5,7-diynedioic acid, with each layer deposition treated under UV light for a defined period of time. Mechanical tears in the film decrease with increasing UV treatment time, suggesting improved mechanical performance. This is attributed to the crosslinking of ligands through polymerization.

Optical microscopy images of the films in Figure 5.4 show that, at 200x magnification, there are substantial differences between the films. At 0 minutes of UV irradiation, the films are more prone to breaking, this can be seen from the large number of triangular tears in the film, with darker triangles being chunks that are hanging over unbroken material. The bright patches are reflections from the light source of the optical microscope and do not give an indication of the optical or mechanical properties of the film.

FTIR analysis of the D57DDA coordinated PbS films was carried out according to the method in section 3.9, with the results shown in Figure 3.5. The results show the gradual onset of a peak at 2950 cm^{-1} which is attributed to the asymmetric, conjugated backbone of the poly(diacetylene) [260].

As an additional characterization method, X-ray photoelectron spectroscopy (XPS) was used to determine the hybridization regimes of carbon in the film. Figure 3.12 shows the de-convoluted C1s peaks.

XPS can also be used to calculate the position of the valence band relative to the Fermi level using the valence scan. This, combined with kelvin probe measurements and UV-vis spectroscopy of the films, can show the band positions relative to the vacuum level seen in Figure 5.6. This was done in the same way as in Chapter 4 and is outlined in section 3.14, so the results are presented here without detailing their acquisition.

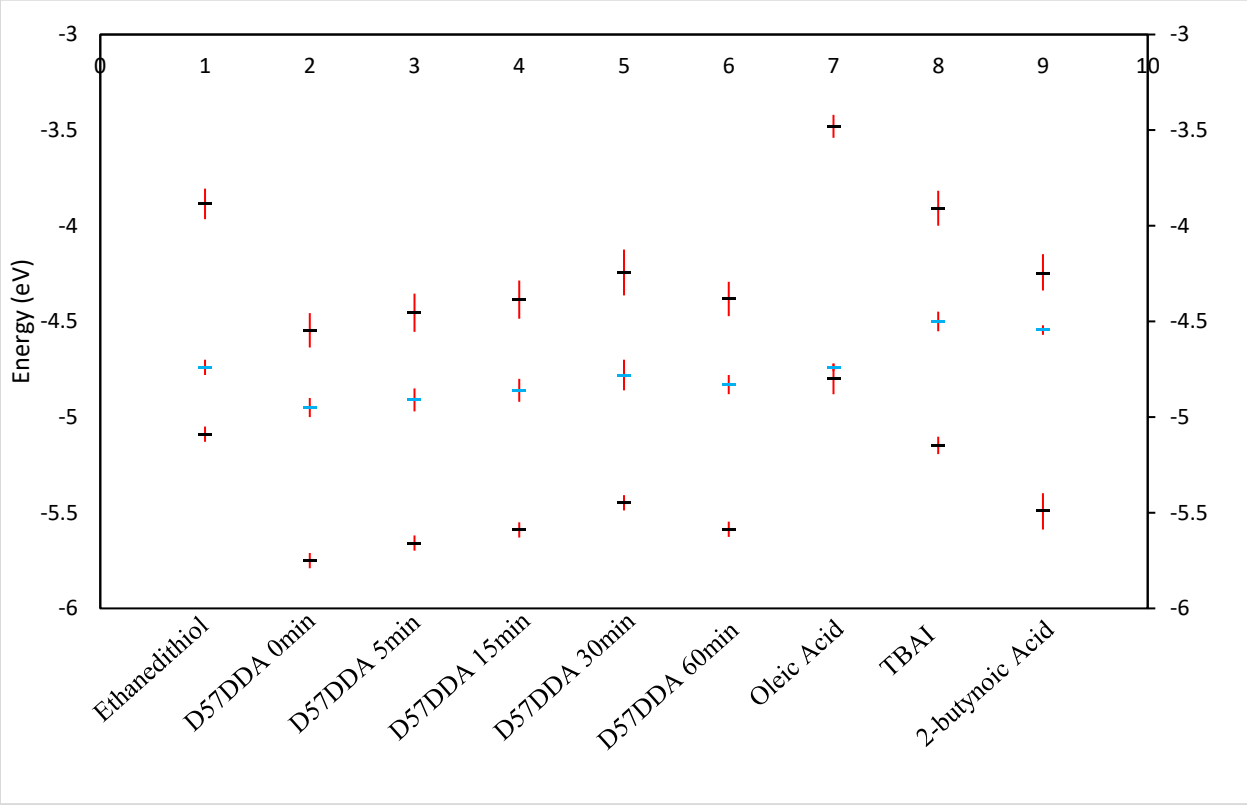


Figure 5.5 - Band positions calculated though XPS, kelvin probe and UV-vis spectrometry PbS films coordinated with (left right): ethanedithiol, dodeca-5,7-diynedioic acid with a UV irradiation time of 0 min, 5min, 15 min, 30 min, and 60 min, oleic acid, tetrabutylammonium iodide, and 2-butynoic acid. The positions show that co-ordination with the diacetylene is distinct from the other ligands, and that the band position is affected by the time under UV irradiation. Error bars (red, vertical) show uncertainty in the valence and conduction bands (black, horizontal) as well as the fermi level (blue, horizontal). Error bars (red, vertical) show the uncertainty in measurements and calculations. A full walk-through of the error calculations is presented in section 3.14.

5.7 Discussion

UV-curing of the coordinated films was done in a layer-by-layer approach as PbS quantum dot solar cells have been shown via EQE to absorb 80% of UV light [53]. This, combined with Mie scattering of light in a nanoparticle film, means that the UV curing is unlikely to work on a film beyond a certain thickness. Optical scans of the resulting layers show fewer tears and defects in the film after longer curing times, indicating that mechanical stability of the films increases with increasing curing time. This is attributed to the crosslinking of coordinated ligands during polymerization, meaning that there is polymerization occurring in the film despite the high UV-vis absorption of the PbS quantum dots.

When examining the FTIR spectra of coordinated and cured films, literature points to characteristic peaks of the backbone structure at 2950 cm^{-1} as the strain on the conjugated backbone will not be even, leading to an asymmetrical bond [260]. The appearance and growth of this peak with increasing curing time heavily suggests that the polymer is being formed throughout the UV-curing process. That there is no indication of carboxylic acid peaks at 1700 cm^{-1} nor the expected oleic acid peak at 3300 cm^{-1} indicates that there is coordination between the polymer and the quantum dot, any uncoordinated polymer would also add the carboxylic acid peak to the FTIR. Given how shallow the peak is, this also suggests that there is very little polymer in the film as a whole, indicating that the band structure of the film will be dominated by the bands of PbS. Indeed, it may be that the polymer serves only to add the occasional energy level, operating more as induced trap states than an alternate charge transport pathway.

Deconvolution of the C1s peak from XPS indicates that the diyne is present, as the peak changes shape in the same way as chapter 4: the transition from sp^2- to sp-hybridized carbon between oleic acid and D57DDA. The re-emergence of the sp^2-hybridized carbon peak after curing shows the

polymerization is successful, as the polymer backbone is composed of alternating double and triple bonds. The growth of this sp^2-hybridized peak relative to the sp-hybridized peak with curing time further suggests this peak is not residual oleic acid, as polymer growth is expected for increasing curing time whereas oleic acid would not be expected to increase its sp^2 component over time. Combined with the information from the FTIR and the optical microscopy, these XPS results show that the monomer ligand has successfully coordinated to the quantum dots and formed the polymer *in-situ* through topochemical polymerization. Band structures collected from kelvin probe, XPS valence scan and UV-vis of the films as outlined in section 3.14 shows the effect of curing time on this world-first *in-situ* polymerized quantum dot-polymer composite film. Figure 5.6 shows a clear shift in the conduction and valence bands relative to oleic acid, confirming a different ligand is present. As the UV treatment time increases, the valance and conduction bands become shallower relative to the vacuum level. This is attributed to the increased presence of the polymer in the film, which would be expected to raise the valence and conduction bands due to the experimentally determined and literature values of the HOMO [266]. Movement of the fermi level is not as pronounced over this curing time, indicating that curing p-dopes the quantum dot thin film. While this can be attributed to the oxidation of the PbS surface due to the presence of UV in an oxygen atmosphere, the concurrent raising of the valence and conduction bands means that the possibility this p-type doping is also a product of polymer formation cannot be excluded. Polymer-induced p-doping is speculated to occur due to the formation of additional energy states in the conjugated π-system of the polymer upon uv-curing.

5.8 Conclusions of Chapter 5

This chapter presents the first reported coordination of a ligand for PbS quantum dots capable of *in-situ* polymerization in the solid state. Further, the band structure of the polymer-quantum dot

film is shown to change with respect to common ligands used in literature and a possible mechanism is speculatively explained. Use of polydiacetylene ligands in quantum dot thin films builds on the work of Ortiz-Cervantes and the use of *in-situ* polymerization for 2D perovskites, extending to 0D structures [225]. Further characterization of the materials by calculating their mobility, ideally through the use of field-effect transistors would be a welcome addition to the body of scientific literature.

Within the context of the thesis, this chapter builds on the ligand dynamics of chapter 4 to present a synthetized ligand using the carboxylic acid anchor to coordinate to the quantum dots. From this proof-of-concept foundation, the performance of this ligand in a photovoltaic cell will be characterized and explained in chapter 6. While the polymer's band positon relative to the quantum dots outside of the composite material is poorly aligned and suggests low chare transfer rates between the organic and inorganic phases, the composite material's deeper band structure and slight n-doping holds promise for future characterization in a photovoltaic device.

6 Characterizing Quantum Dot-Polydiacetylene Photovoltaic Devices

6.1 Introduction

Having demonstrated that a monomer ligand can be polymerized *in-situ* in a quantum dot thin film in the previous chapter, this chapter characterizes its performance in a solar cell. In general, COINs exhibit high mobility due to favorable band alignment between energy levels in the quantum dot and the organic material [211], [225], [287]. However, this use in solar cells is limited. As such, characterization of how the COIN performs in a solar cell is an important step towards their use in diverse optoelectronic devices.

Device performance is expected to improve based on the polymer's inclusion. Short circuit current is expected to improve based on the speculated improvement to mobility the polymer's addition will bring to the quantum dot thin film. Further, the speculated use of the polymer as an efficient method of charge separation is expected to reduce SRH recombination in the cell, resulting in higher V_{oc} and fill factor. This would advance the field of quantum dot-organic hybrid photovoltaics, providing an understanding of how a fully integrated organic phase in a solar cell affects device performance. Further, this work will develop the current understanding of polydiacetylenes in photovoltaic applications.

One important confounding variable may be the work-up method of the ligand during synthesis. It was shown in chapter 3 that an additional purification step could be added to the synthetic work-up, resulting in a 1-step method and 2-step method for ligand isolation and preparation. It is expected that the 1-step preparation method will produce a ligand exchange solution with more impurities that will subsequently inhibit cell performance. For example, these impurities may be optically inactive, providing barriers to charge transport through the film and low shunt resistances, leading to reduced short-circuit current. This chapter therefore looks at what device architecture

the device will perform the best in, and then examines the difference in performance between the two work-up methods.

6.2 Quantum dot- Poly(diacetylene) layer positioning and comparison

To determine a suitable device structure, devices were manufactured as outlined in chapter 3 with the QD-polymer hybrid layer as either the absorber layer or the hole-transport layer. For each cell, 7 layers of the absorber material and 2 layers of the hole-transport layer were deposited, with the process for layer deposition also outlined in Chapter 3. Each D57DDA passivated layer was subjected to 15 minutes of UV irradiation regardless of device, using the 1-step work up solution of diyne mentioned in Chapter 5. The results of the cell are presented in Figure 3.15.

Based on these results, the use of the quantum dot-polymer hybrid layer was selected as a hole-transport layer instead of a light-absorbing layer. To compare the efficacy of the *in-situ* polymerized layer, four types of devices were made with different hole-transport layers, presented in section 3.17.2.

6.2.1 Discussion

The relative positions of the valence band, conduction band, and Fermi level positions of the dodeca-5,7-diynedioic aid (D57DDA) coordinated PbS film as determined in Chapter 5 present a few options for the design of a solar cell device. Figure 6.1 shows the band diagrams of possible device architectures utilizing the D57DDA passivated quantum dot material, under the effects of band bending described by Anderson's rule. Use of the D57DDA material as a hole-transport layer does not look favorable given the large discontinuities in the band structure at the absorber and hole-transport layer interface, which is not as prominent in the use of D57DDA-passivated PbS as the absorber material.

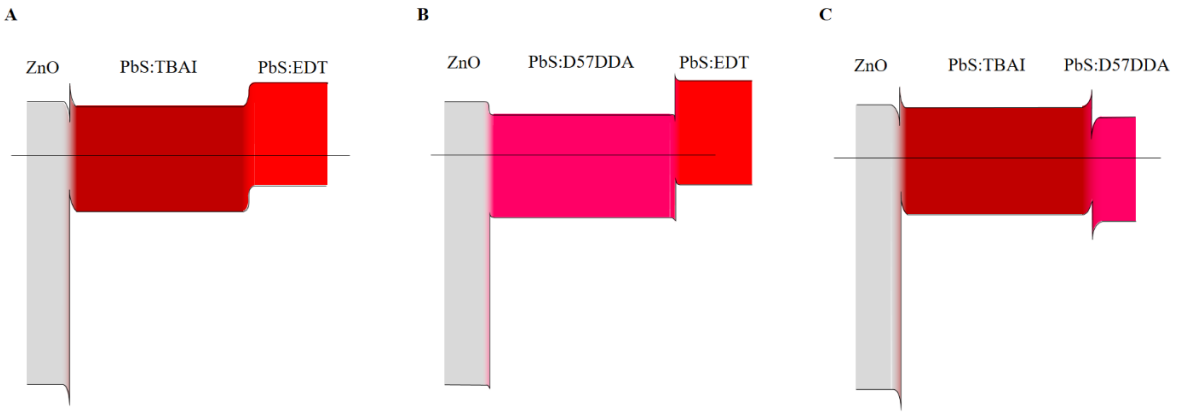


Figure 6.1 - Band structures of the standard control solar cell in this thesis (a). The new D57DDA ligand could replace the absorber layer of TBAI (b) or the hole-transport layer in place of EDT (c). The black line represents the equalized Fermi level across the device, from ITO to gold contacts. Band positions of semiconductor materials have been adjusted accordingly to a constant fermi level. The D57DDA passivated layers (pink) are represented by the band positions after 15 minutes of UV curing.

The results presented in Figure 3.15 contrast this expectation, as the use of D57DDA passivated PbS in the absorber layers leads to lower efficiency. Low J_{sc} and shunt resistance indicate that there are many pathways for charges to recombine through the cell. Similarly, the built-in potential of the cell should be similar to that of an absorber layer passivated with TBAI, as the hole-transport layer and electron-transport layers are the same (ZnO and EDT passivated PbS, respectively). That the V_{oc} is so low indicates that recombination processes are not allowing the applied bias to reach the built-in potential of the device's junction.

Using D57DDA passivated PbS in the hole-transport layer, however, results in higher Jsc, indicating that more charges are able to leave the cell. The lower gradient of the J-V curve at the short circuit current indicates that the shunt resistance is high, suggesting fewer recombination pathways for charges. Another key observation is that the PbS:D57DDA hole-transport layer device follows a similar shape to the control device, however, is offset by the difference in their short circuit currents. A possible explanation for this is light filtering, wherein the polymer formed in the PbS:D57DDA film upon UV curing is absorbing part of the solar spectrum but not

participating in the photovoltaic process. This would also explain the poor performance of the D57DDA absorber layer, as the majority of the cell is absorbing light which would then not generate excitons. However, the cell is constructed such that the hole-transport layer is on the back side of the cell, meaning light will pass through the absorber layer before reaching the hole-transport layer, suggesting that this effect should be minimal with respect to the hole-transport layer.

Figure 3.16 shows how the D57DDA compares in a separate series of devices to poly(D57DDA) on its own and a control using EDT as in a standard device. The high short circuit current indicates that charges are readily being extracted from the cell, suggesting the hole-transport layer is efficient in preventing recombination. However, the lower V_{oc} compared to the control device is expected, as the band structure in Figure 6.1 results in a lower V_{bi} for the device. This is due to the D57DDA hole-transport layer having a deeper work function than the EDT passivated PbS.

Using pure poly(D57DDA) as a hole-transport layer in a similar manner to Neo *et al* [54], the series resistance is higher than the hybrid polymer:quantum dot hole-transport layer device, as indicated by the slope of the curve at open circuit voltage. This is indicative of electrical resistance in the cell, which could be due to the thickness of the hole-transport layer, as 100mg/ml concentration would result in a substantially thick film. It is likely the performance of this hole-transport layer could be improved through the optimization of layer thickness. The performance of the *ex-situ* polymerized D57DDA in conjunction with the performance of the absorber layer in Figure 3.16 is intriguing give the report of polydiacetylenes as pure organic photovoltaics my Muthitamongkol et al., wherein the polymer performs poorly as a photoabsorber [272]. This could indicate that the polymer is dominating the hole-transport properties similar to the use of P3HT as a hole-transport layer by Neo *et al* [54].

6.3 Effect of UV curing on Hole-Transport layer

6.3.1 Discussion

UV curing of the D57DDA passivated films improves the performance of devices. Without UV curing, the device has a low short circuit current, which doubles after 5 minutes of UV-curing and remains mostly constant. However, the EDT devices deteriorate under increasing UV irradiation, indicating that this improvement is due to the presence of the novel ligand rather than an intrinsic improvement of the devices after UV treatment. This increase in performance is also visible in both the 1-step and 2-step work up process batches, further indicating that the improvement is due to the formation of the polymer. It is speculated that the diyne bond in the uncured D57DDA ligand acts as a trap site. As seen in Chang *et al*. [137], formation of the polymer creates an extended π-state which allows hole-transport through the layer, rather than trapping the charges on the monomer ligand. The formation of these extended states would also shift their energy level, reducing their efficacy as recombination centers.

The V_{oc} of devices using the 1-step process also show improvement with increasing UV-curing time. One speculative reason for this is that the UV curing in an oxygenated environment allows unpassivated bonds on the quantum dot surface to form lead oxide. This would introduce additional energy states close to the valence band, p-doping the hole-transport material and leading to a higher built-in voltage. The effect can also be seen in the EDT control device, however to a far lesser extent, as EDT has been suggested to improve solar cell performance via a similar mechanism, leaving fewer opportunities for UV curing to p-dope the layer.

UV Curing Time (minutes)	Series Resistance Control (kΩ)	Series Resistance 1-step (kΩ)	Series Resistance 2-step (kΩ)
0	0.648 ± 0.148	1.360 ± 0.226	0.633 ± 0.144
5	1.602 ± 0.061	0.756 ± 0.065	12.230 ± 4.001
15	1.199 ± 0.070	0.418 ± 0.146	9.740 ± 2.753
30	0.927 ± 0.094	0.945 ± 0.223	6.839 ± 2.169
60	1.234 ± 0.063	0.414 ± 0.005	59.105 ± 3.222

Table 6.1 – Series resistances calculated from the slope of the J-V curve at open circuit voltage for devices exposed to UV irradiation.

The slope of the J-V curve at open circuit voltage is an indication of the series resistance, the internal resistance faced by charges travelling through the device. The series resistances of all devices approximated from the slope at V_{OC} is shown in Table 6.1. Most striking is the high series resistances of the 2-step devices in comparison to the 1-step devices. This suggests that the devices using the pure D57DDA ligand exchange solution are significantly less conductive than those using the contaminated ligand exchange solution. The 1-step method also demonstrates remarkably low series resistance, indicating that the hole-transport layer is highly conductive, more than even that in the control cells. Further, the highest series resistance in the 1-step devices was found in the device with no UV curing, indicating that the polymer is responsible for the reduced series resistance. Tying the differences in series resistance across the 1-step and 2-step devices together, the difference is speculated to be due to the conductivity of the polymer. Polymer un-doped is likely to have trap states like those observed by Chen *et al*, and thus would be less conductive as charges recombine. High recombination in the HTL would also affect the J_{sc} which is seen in the dramatically lower values for the 2-step method.

The two work-up procedures differ in that the 2-step second process results in a lighter peach color when dissolved in acetonitrile to a concentration of 100mg/ml solids. By comparison, the 1-step

process maintains a deep yellow color at the same concentration of dissolved solids in acetonitrile. The lack of this discoloring impurity is speculated to be contributing to the reduced performance of the devices using the 2-step work up process. Understanding the origin of this impurity will provide valuable insight into how to improve future devices.

The impurity is assumed to originate from the synthesis of the diyne ligand, as it is present in the 1-step work up process but not in the 2-step work up process. Given the synthesis and work-up process use only solvents, copper chloride, and ammonium chloride, the impurity is speculated to originate from one of these two halide salts [243]. Based on the results of chapter 4, the method by which the ammonium ion could coordinate with the PbS. Further, there is no literature that suggests the ammonium ion will interact with the diacetylene, thus the ammonium ion can be discarded as a possibility. The Cu^{+} ion could passivate the PbS surface as a Z-type ligand on sulfur sites. Critically, unpassivated sulfur atoms are not targeted by most organic ligands, meaning that the quantum dots could be passivated in a manner closer to a core-shell approach, like the perovskite shelling of Yang *et al*. using PbI_2 [197]. It is speculated that this approach could lead to a shallowing of the quantum dot band positions relative to the vacuum, bringing them more in line with the polymer's band structure as elucidated in section 5.3. This would lead to improved charge transfer within the hole-transport layer and less SRH recombination, improving the short circuit current of the cell as more charges are extracted by the contacts. However, this process does not directly impact the material properties of the polymer in the composite. The discussion in section 6.2.1 indicates that the polymer is defining the role of the hole-transport layer, indicating that the improvement in device performance caused by the impurity is due to its effect on the polymer instead of the quantum dots. Given there are no reported methods of doping polydiacetylene with copper, it is unlikely to be the impurity.

A more likely impurity is the chloride ion, as it is present in both of the synthetic reaction's halide salts. Chloride ions would remain in solution while the D57DDA molecule precipitates out of the cold aqueous hydrochloric acid as described in Section 3.17, meaning the additional work-up step is likely to remove most of the chlorine. Additionally, halides have been shown on numerous occasions to increase the conductivity of polydiacetylene by oxidizing the backbone, forming positively charged polarons with sufficiently lower polaron activation energies to promotes charge transport through the MTR model at room temperature, in a manner similar to that shown by Lu *et al*. in section 1.4.3 [100], [301]. Further, chlorine ions are capable of passivating lead chalcogenide quantum dot surfaces as X-type ligands, resulting in fewer trap states [302]. This would reduce the prevalence of trap-assisted recombination and increase the mobility of the material, dramatically increasing the short circuit current as more charges are collected by the electrodes. An alternative method could be due to the impurity coordinating to the quantum dot and raising its valence band level relative to the vacuum. This would improve the alignment between the polymer and quantum dot, leading to improved charge transfer and higher charge mobilities. However, by using chlorine as the impurity, the speculative improvement due to band alignment after more complete passivation is unlikely. This is because chlorine deepens the band position of quantum dots relative to the vacuum level, which would widen the 0.4 eV gap between polymer and quantum dot, further misaligning them and reducing the chance of charge transfer [55].

6.4 Nature of purified Diyne's poor performance

Having discovered that the additional purification step during the synthesis of D57DDA is not beneficial to the performance of the diyne, two additional questions emerge. Firstly, there is the nature of the purified diyne's worse performance. To this end, dark JV curves of the devices

presented in section 3.17.3 were taken, and analyzed using a semi-log J-V plot, where current density is on a logarithmic scale.

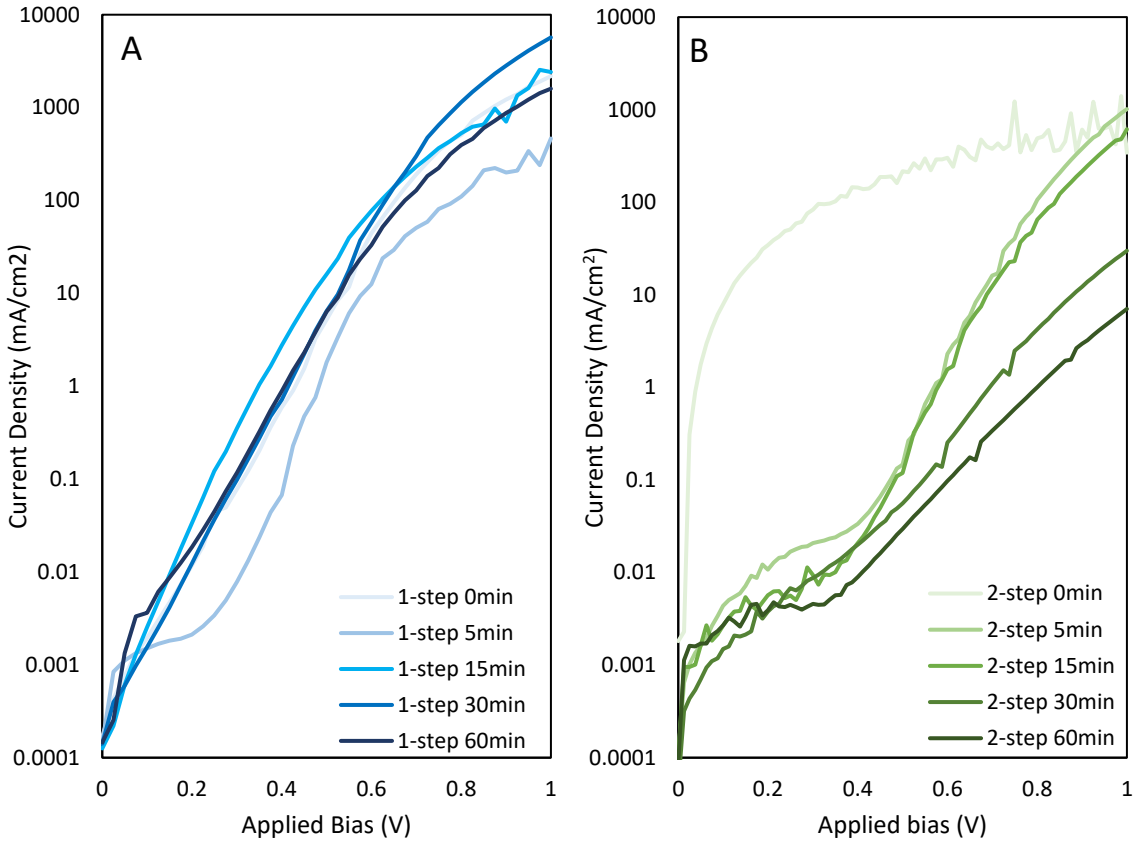


Figure 6.2 – Dark J-V curves of devices passivated with D57DDA made using the (A) 1-step work up method and (B) using the 2-step purification method. Darker shades of line colors represent longer UV irradiation exposure.

Secondly, there is the quantification of the impurity's performance, in order to determine the ratio of impurity to D57DDA in the ligand exchange solution. Here, devices were prepared to assess the effect of chlorine on the samples, as this is considered the most likely contaminant. Device architecture was kept consistent with those in section 3.17.2, however none of the layers were UV-cured. For each hole-transport layer, a solution of D57DDA prepared using the 2-step work up method was used, with the addition of different concentrations of tetrabutylammonium chloride as a chloride ion source. All other fabrication steps proceeded according to the method laid out in section 3.4. Table 6.2 shows the performance metrics of devices with different chloride ion concentrations under 1 sun illumination.

Cl^- Concentration (M)		J_{sc} (mA/cm²)	V_{oc} (mV)	Fill Factor	PCE (%)	R_{sh} (Ω/cm²)	R_{se} (Ω/cm²)
EDT	0	12.82 ± 0.96	485 ± 3	0.511 ± 0.018	3.186 ± 0.373	$7.86E^{5}$ ± $2.42E^{4}$	0.12 ± 0.01
	0.001	14.13 ± 0.44	500 ± 3	0.526 ± 0.015	3.760 ± 0.74	3.76 ± 0.74	0.14 ± 0.02
	0.01	11.47 ± 4.45	510 ± 3	0.365 ± 0.067	2.218 ± 1.235	8.75 ± 1.45	0.05 ± 0.03
D57DDA	0	0.03 ± 0.01	305 ± 45	0.157 ± 0.010	0.002 ± 0.001	$2.03E^{7}$ ± $4.13E^{6}$	$4.09E^{-5}$ ± $6.59E^{-6}$
	0.001	3.82 ± 2.38	36 ± 11	0.157 ± 0.117	0.032 ± 0.041	11.22 ± 8.37	0.10 ± 0.04
	0.01	2.30 ± 1.60	182 ± 270	0.129 ± 0.166	0.215 ± 0.371	8.60 ± 4.91	0.04 ± 0.02

Table 6.2 - changes in various solar cell performance metrics after the introduction of chloride ions to the hole-transport ligand exchange solution during device fabrication. Devices fabricated with D57DDA were not subject to UV irradiation.

6.4.1 Discussion

Dark JV analysis was used to determine the nature of the trap states in the film. Figure 6.2 shows that the 1-step process is roughly linear in the semi-log plot, suggesting that the devices are a single junction that can be modelled by a 1-diode model. Further, this indicates that there is only one dominant recombination method, which is speculated to be Auger recombination. However, it is noted that Auger recombination is unlikely at 1-sun illumination of devices using the AM1.5G solar spectrum, and another candidate could be SRH recombination [303]. In the 5- and 60-minute devices, there is a shoulder at low bias, which may be indicative of another recombination method in the device such as SRH or even radiative recombination. However, that this could also be due to a low shunt resistance means conclusions cannot be drawn on the nature of this defect without additional testing, such as intensity-dependent or temperature-dependent J-V sweeps.

The shape of the plot for the 2-step devices is distinctly different, with two roughly linear regions. This suggests the fit could be more closely approximated by the 2-step model, indicating both speculated methods of recombination are prominent [24]. Combining the illuminated JV sweeps, Table 6.1 shows the series resistances of the 1-step devices are far lower than the 2-step devices, however the influence of R_{se} is more visible in the 1-step devices than the 2-step devices in Table

6.1. This suggests that the influence of recombination in the 1-step devices is lower overall than the 2-step devices. As a result, it can be inferred that there are two recombination pathways in the 2-step but only one in the 1-step devices. This suggests that the impurity dopes the polymer to promote favorable band alignment with the quantum dot, suppressing SRH recombination in a method similar to that reported by Mastria *et al*., leading to the improved performance under illumination [215].

It is important to note that the devices made with the added chloride ion impurity were not exposed to UV irradiation, which can be assumed not to contain the polymer. Therefore, the chloride ion's effect on the polymer has not been addressed with this experiment. While the polymer's absence prevents a complete picture of the chloride ion's inclusion on device properties, this experiment nonetheless gives an indication of whether the passivation of PbS by the impurity plays a role, as discussed in section 6.3.1. Diyne-passivated devices show a far larger short circuit current increase after chlorine introduction than EDT devices, suggesting passivation of Pb^{+} trap states beyond the capabilities of D57DDA alone. This would suppress SRH recombination, consistent with the speculated effect described in section 6.3.1. Future work such as detailed Cl2p and Cu3d scans from X-ray photoelectron spectroscopy would also be able to identify the contaminant, and would give some indication of its quantity in the material.

6.5 Conclusion

In summary, this chapter presents the photovoltaic use of a quantum dot thin film with an *in-situ* polymerized ligand. The performance of the material is evaluated with respect to UV irradiation time, and found that the device performance improves with increasing UV exposure. Further, an impurity is found to cause a dramatic improvement in the short circuit current of the device, this is attributed to the doping of the polydiacetylene backbone formed from the polymerized ligand.

The results of this chapter build upon the previous thesis chapters, wherein the polymerizable ligand has been designed, synthesized, and integrated into a quantum dot thin film. Following from the synthesis and successful coordination of a bifunctional diyne ligand in chapter 5, this chapter utilizes the material in photovoltaic devices and speculates on the performance of the material with and without an unknown impurity. In constructing devices, this work places itself within the broader literature as a demonstration it is possible to build a solar cell using this novel COIN structure with *in-situ* polymerization of the ligand. This expands the available methods of constructing COINs for photovoltaic energy harvesting applications [81], [211], [225].

7 Conclusions and future work

7.1 Conclusions of the Thesis

The field of colloidal quantum dot solar cells holds immense promise for the future of next generation photovoltaics, due to their unique material properties and potential for low-cost processing. By utilizing perovskite shelling on PbS quantum dots and advances in passivation techniques, efficiencies have improved from <0.1% to 18.4% over the past 15 years [200]. Alongside this, hybrid organic-inorganic materials such as 2D-perovskites with polydiacetylene or coupled organic-inorganic nanostructures (COINs) have been developed, and a deep understanding of charge transport phenomena has been established.

The work presented in this thesis represents the design and development of a novel organic-inorganic hybrid material, where the ligands passivating a quantum dot are polymerized *in-situ*, after film formation. This was intended to improve the lifetime and mobility of charges in the material, as electrons and holes would be separated across the inorganic-organic phases, respectively. In pursuit of the proof-of-concept material, this thesis makes the following contribution to the field of PbS Quantum dots:

(i) The first part of this work looks at the dynamics of ligand exchange on the PbS surface through the use of FTIR and XPS spectroscopic methods, with the aim of coordinating an alkyne-based ligand to PbS quantum dots. Here, the work contributes conclusive proof through XPS and electron microscopy to determine the coordination regime of amines on PbS quantum dots. By systematically varying the terminal amine ligand or solvent used in the ligand exchange process, this work has shown that amine anchor moieties do not coordinate to PbS quantum dots. The work presented is in agreement with previous literature, and a speculative mechanism for the coordination of an alcohol in the presence of a terminal amine is presented. Further, this is the first report of an alkyne being coordinated to PbS quantum dots by means of a carboxylic acid anchor moiety. Characterization of the film's electronic structure showed that the alkyne ligand was able to n-dope the quantum dots, expanding the library of ligand available.

(ii) This work designs and synthesizes a bidentate ligand capable of *in-situ* polymerization after the casting of a film. This is the first report of *in-situ* polymerization of a quantum dot ligand. The polymer is electronically characterized in isolation using cyclic voltammetry and UV-vis spectroscopy, before confirmation of *in-situ* polymerization is characterized using FTIR and XPS. In addition, XPS, Kelvin probe, and UV-vis spectroscopy are used in concert to characterize the band structure as a function of UV-irradiation, a proxy for photo-polymerization. It is shown that the material becomes progressively more p-doped as UV-irradiation time increases to 30 minutes.

(iii) Having created a new class of *in-situ* polymerizing ligands for quantum dots, this paper characterizes their performance in a solar cell. Here, this work shows that the organic-inorganic hybrid material performs best as the hole transport layer in a standard p-i-n

heterojunction architecture, and that longer UV irradiation time will increase the collected photocurrent of the cell. This paper also shows that impurities generated by the synthesis of the ligand beneficially impact the performance of the final device. It is speculated that this is due to the impurity doping the polymer and allowing for improved charge transport.

7.2 Future Work

This proof-of-concept thesis provides considerable speculation into the mechanisms and nature of many observed phenomena. Recommendations for future work are as follows:

(i) Determination of the mechanism by which amines assist the coordination of terminal alcohols to the PbS quantum dot surface. This would deepen the understanding of quantum dot ligand exchange dynamics and open the possibility of amine-assisted coordination of more complex alcohol-terminated ligands, expanding the ligand library.

(ii) Characterization of the impurity present in the synthesis of dodeca-5,7-diynedioic acid. This could be achieved using XPS methods. Determination of the mechanism by which this improves the performance of the final solar cell is equally critical, and could be achieved through the use of temperature- or illumination-dependent J-V sweeps. Understanding the role of the impurity could lead to improved device performance through the deliberate introduction of other impurities. Robust characterization of the material's electron and hole mobility and lifetime would be an excellent starting point for this line of future work. Repetition of the introduced chloride ion experiment described in section 6.4 with UV irradiation could determine the effect of the impurity on the polymer, and should be a priority for any future work building upon this thesis.

(iii) Iterations on the polymer design could improve the performance of the material in photovoltaic applications. The side-chains of a polymer will vary the final band positions, even with identical conjugated backbones [217]. The use of density functional theory (DFT) to model the expected band positions of the final polymer would lead to better alignment with the valence and conduction bands of the quantum dots, resulting in improved charge transport characteristics such as lifetime and mobility. Incorporation of aspects such as thiophene moieties and optimizing the length of the pendant may further improve the charge transfer between the organic and inorganic phases of the material [71], [81].

8 References

[1] J. Marotzke and P. M. Forster, "Forcing, feedback and internal variability in global temperature trends," *Nature*, vol. 517, no. 7536, pp. 565–570, Jan. 2015, doi: 10.1038/nature14117.

[2] A. Louwen, W. G. J. H. M. van Sark, R. E. I. Schropp, W. C. Turkenburg, and A. P. C. Faaij, "Life-cycle greenhouse gas emissions and energy payback time of current and prospective silicon heterojunction solar cell designs: LCA of current and prospective silicon heterojunction solar cells," *Prog. Photovolt: Res. Appl.*, vol. 23, no. 10, pp. 1406–1428, Oct. 2015, doi: 10.1002/pip.2540.

[3] T. Princen, J. P. Manno, and P. L. Martin, *Ending the Fossil Fuel Era*. MIT Press, 2015.

[4] D. Helm, *Burn Out: The Endgame for Fossil Fuels*. Yale University Press, 2017.

[5] K. P. Bhandari, J. M. Collier, R. J. Ellingson, and D. S. Apul, "Energy payback time (EPBT) and energy return on energy invested (EROI) of solar photovoltaic systems: A systematic review and meta-analysis," *Renewable and Sustainable Energy Reviews*, vol. 47, pp. 133–141, Jul. 2015, doi: 10.1016/j.rser.2015.02.057.

[6] G. Masson, I. Kaizuka, A. Detollenaere, and J. Lindahl, "PVPS Snapshot 2019 Report," *International Energy Association*, vol. T1, no. 35, 2019.

[7] G. Masson, I. Kaizuka, E. Bosch, A. Detollenaere, G. Neuborg, and J. van Wetter, "Trends in Potovoltaic Applications 2019," *International Energy Association*, vol. T1, no. 36, 2019.

[8] "Renewable energy market analysis: GCC 2019," p. 154.

[9] H.-W. Sinn, "Buffering volatility: A study on the limits of Germany's energy revolution," *European Economic Review*, vol. 99, pp. 130–150, Oct. 2017, doi: 10.1016/j.euroecorev.2017.05.007.

[10] F. Marechal, D. Favrat, and E. Jochem, "Energy in the perspective of the sustainable development: The 2000W society challenge," *Resources, Conservation and Recycling*, vol. 44, no. 3, pp. 245–262, Jun. 2005, doi: 10.1016/j.resconrec.2005.01.008.

[11] T. D. Lee and A. U. Ebong, "A review of thin film solar cell technologies and challenges," *Renewable and Sustainable Energy Reviews*, vol. 70, pp. 1286–1297, Apr. 2017, doi: 10.1016/j.rser.2016.12.028.

[12] R. J. Ellingson *et al.*, “Highly Efficient Multiple Exciton Generation in Colloidal PbSe and PbS Quantum Dots,” *Nano Letters*, vol. 5, no. 5, pp. 865–871, May 2005, doi: 10.1021/nl0502672.
[13] A. Shabaev, Al. L. Efros, and A. J. Nozik, “Multiexciton Generation by a Single Photon in Nanocrystals,” *Nano Lett.*, vol. 6, no. 12, pp. 2856–2863, Dec. 2006, doi: 10.1021/nl062059v.
[14] H. Goodwin, T. C. Jellicoe, N. J. L. K. Davis, and M. L. Böhm, “Multiple exciton generation in quantum dot-based solar cells,” *Nanophotonics*, vol. 7, no. 1, pp. 111–126, Jan. 2018, doi: 10.1515/nanoph-2017-0034.
[15] J. A. McGuire, J. Joo, J. M. Pietryga, R. D. Schaller, and V. I. Klimov, “New Aspects of Carrier Multiplication in Semiconductor Nanocrystals,” *Acc. Chem. Res.*, vol. 41, no. 12, pp. 1810–1819, Dec. 2008, doi: 10.1021/ar800112v.
[16] V. I. Rupasov and V. I. Klimov, “Carrier multiplication in semiconductor nanocrystals via intraband optical transitions involving virtual biexciton states,” *Phys. Rev. B*, vol. 76, no. 12, p. 125321, Sep. 2007, doi: 10.1103/PhysRevB.76.125321.
[17] M. C. Beard, J. M. Luther, O. E. Semonin, and A. J. Nozik, “Third Generation Photovoltaics based on Multiple Exciton Generation in Quantum Confined Semiconductors,” *Acc. Chem. Res.*, vol. 46, no. 6, pp. 1252–1260, Jun. 2013, doi: 10.1021/ar3001958.
[18] A. J. Nozik, M. C. Beard, J. M. Luther, M. Law, R. J. Ellingson, and J. C. Johnson, “Semiconductor Quantum Dots and Quantum Dot Arrays and Applications of Multiple Exciton Generation to Third-Generation Photovoltaic Solar Cells,” *Chemical Reviews*, vol. 110, no. 11, pp. 6873–6890, Nov. 2010, doi: 10.1021/cr900289f.
[19] M. C. Hanna and A. J. Nozik, “Solar conversion efficiency of photovoltaic and photoelectrolysis cells with carrier multiplication absorbers,” *Journal of Applied Physics*, vol. 100, no. 7, p. 074510, Oct. 2006, doi: 10.1063/1.2356795.
[20] M. Iqbal, *An Introduction To Solar Radiation*. Elsevier, 2012.
[21] B. Ashton, M. Stevenson, and J. Canning, “Solar hypersensitization of optical fibers,” *Optics Letters*, vol. 32, no. 6, p. 608, Mar. 2007, doi: 10.1364/OL.32.000608.
[22] J. Chantana, Y. Kawano, T. Nishimura, A. Mavlonov, and T. Minemoto, “Thermodynamic limit of tandem solar cells under different solar spectra and their perovskite top solar cell,” *Optical Materials*, vol. 113, p. 110819, Mar. 2021, doi: 10.1016/j.optmat.2021.110819.
[23] P. Altermatt, “The Role of a PN Junction,” *PV Lighthouse*, Jun. 01, 2011. https://pvlighthouse.com.au/cms/lectures/altermatt/principle/p-n-junction (accessed Jul. 15, 2022).
[24] J. Nelson, *The Physics of Solar Cells*, vol. 1, 1 vols. London, United Kingdom: Imperial College Press, 2003.
[25] A. Rao and R. H. Friend, “Harnessing singlet exciton fission to break the Shockley–Queisser limit,” *Nat Rev Mater*, vol. 2, no. 11, p. 17063, Nov. 2017, doi: 10.1038/natrevmats.2017.63.
[26] C. A. Nelson, N. R. Monahan, and X.-Y. Zhu, “Exceeding the Shockley–Queisser limit in solar energy conversion,” *Energy & Environmental Science*, vol. 6, no. 12, p. 3508, 2013, doi: 10.1039/c3ee42098a.
[27] Y. Zhang, Y. Liu, C. Li, X. Chen, and Q. Wang, “Controlled Synthesis of Ag_2S Quantum Dots and Experimental Determination of the Exciton Bohr Radius,” *The Journal of Physical Chemistry C*, vol. 118, no. 9, pp. 4918–4923, Mar. 2014, doi: 10.1021/jp501266d.
[28] S. Baskoutas and A. F. Terzis, “Size-dependent band gap of colloidal quantum dots,” *Journal of Applied Physics*, vol. 99, no. 1, p. 013708, Jan. 2006, doi: 10.1063/1.2158502.
[29] M. A. Hines and G. D. Scholes, “Colloidal PbS Nanocrystals with Size-Tunable Near-Infrared Emission: Observation of Post-Synthesis Self-Narrowing of the Particle Size Distribution,” *Adv. Mater.*, vol. 15, no. 21, pp. 1844–1849, Nov. 2003, doi: 10.1002/adma.200305395.

[30] A. Stavrinadis and G. Konstantatos, “Strategies for the Controlled Electronic Doping of Colloidal Quantum Dot Solids,” *ChemPhysChem*, vol. 17, no. 5, pp. 632–644, Mar. 2016, doi: 10.1002/cphc.201500834.
[31] S. J. Oh *et al.*, “Stoichiometric Control of Lead Chalcogenide Nanocrystal Solids to Enhance Their Electronic and Optoelectronic Device Performance,” *ACS Nano*, vol. 7, no. 3, pp. 2413–2421, Mar. 2013, doi: 10.1021/nn3057356.
[32] J. M. Luther and J. M. Pietryga, “Stoichiometry Control in Quantum Dots: A Viable Analog to Impurity Doping of Bulk Materials,” *ACS Nano*, vol. 7, no. 3, pp. 1845–1849, Mar. 2013, doi: 10.1021/nn401100n.
[33] L. Meng *et al.*, “Unusual Surface Ligand Doping-Induced p-Type Quantum Dot Solids and Their Application in Solar Cells,” *ACS Appl. Mater. Interfaces*, vol. 12, no. 48, pp. 53942–53949, Dec. 2020, doi: 10.1021/acsami.0c15576.
[34] J. B. Rivest and P. K. Jain, “Cation exchange on the nanoscale: an emerging technique for new material synthesis, device fabrication, and chemical sensing,” *Chem. Soc. Rev.*, vol. 42, no. 1, pp. 89–96, 2013, doi: 10.1039/C2CS35241A.
[35] M. S. Kang, A. Sahu, C. D. Frisbie, and D. J. Norris, “Influence of Silver Doping on Electron Transport in Thin Films of PbSe Nanocrystals,” *Adv. Mater.*, vol. 25, no. 5, pp. 725–731, Feb. 2013, doi: 10.1002/adma.201203114.
[36] S. K. Saha, A. Bera, and A. J. Pal, “Improvement in PbS-based Hybrid Bulk-Heterojunction Solar Cells through Band Alignment via Bismuth Doping in the Nanocrystals,” *ACS Appl. Mater. Interfaces*, vol. 7, no. 16, pp. 8886–8893, Apr. 2015, doi: 10.1021/acsami.5b01521.
[37] D. Yu, C. Wang, and P. Guyot-Sionnest, “*n* -Type Conducting CdSe Nanocrystal Solids,” *Science*, vol. 300, no. 5623, pp. 1277–1280, May 2003, doi: 10.1126/science.1084424.
[38] W. Koh *et al.*, “Heavily doped n-type PbSe and PbS nanocrystals using ground-state charge transfer from cobaltocene,” *Sci Rep*, vol. 3, no. 1, p. 2004, Dec. 2013, doi: 10.1038/srep02004.
[39] H. Liu, S. Keuleyan, and P. Guyot-Sionnest, “n- and p-Type HgTe Quantum Dot Films,” *J. Phys. Chem. C*, vol. 116, no. 1, pp. 1344–1349, Jan. 2012, doi: 10.1021/jp2109169.
[40] F. P. García de Arquer, T. Lasanta, M. Bernechea, and G. Konstantatos, “Tailoring the Electronic Properties of Colloidal Quantum Dots in Metal-Semiconductor Nanocomposites for High Performance Photodetectors,” *Small*, vol. 11, no. 22, pp. 2636–2641, Jun. 2015, doi: 10.1002/smll.201403359.
[41] A. Rath *et al.*, “Remote Trap Passivation in Colloidal Quantum Dot Bulk Nano-heterojunctions and Its Effect in Solution-Processed Solar Cells,” *Adv. Mater.*, vol. 26, pp. 4741–4747, 2014.
[42] M. Liu *et al.*, “Hybrid organic–inorganic inks flatten the energy landscape in colloidal quantum dot solids,” *Nature Materials*, vol. 16, no. 2, pp. 258–263, Nov. 2016, doi: 10.1038/nmat4800.
[43] B. Sun *et al.*, “Pseudohalide-Exchanged Quantum Dot Solids Achieve Record Quantum Efficiency in Infrared Photovoltaics,” *Advanced Materials*, p. 1700749, May 2017, doi: 10.1002/adma.201700749.
[44] P. K. Santra and P. V. Kamat, “Mn-Doped Quantum Dot Sensitized Solar Cells: A Strategy to Boost Efficiency over 5%,” *Journal of the American Chemical Society*, vol. 134, no. 5, pp. 2508–2511, Feb. 2012, doi: 10.1021/ja211224s.
[45] Q. Hou, L. Zhu, H. Chen, H. Liu, and W. Li, “Highly regular and ultra-thin porous ZnO nanosheets: An indirect electrodeposition method using acetate-containing precursor and their application in quantum dots-sensitized solar cells,” *Electrochimica Acta*, vol. 94, pp. 72–79, Apr. 2013, doi: 10.1016/j.electacta.2013.01.122.
[46] Z. L. Wang, “Zinc oxide nanostructures: growth, properties and applications,” *Journal of Physics: Condensed Matter*, vol. 16, no. 25, pp. R829–R858, Jun. 2004, doi: 10.1088/0953-8984/16/25/R01.

[47] J. Khan *et al.*, "Low-temperature-processed SnO_2–Cl for efficient PbS quantum-dot solar cells via defect passivation," *J. Mater. Chem. A*, 2017, doi: 10.1039/C7TA05366E.
[48] B. D. Chernomordik, A. R. Marshall, G. F. Pach, J. M. Luther, and M. C. Beard, "Quantum Dot Solar Cell Fabrication Protocols," *Chemistry of Materials*, vol. 29, no. 1, pp. 189–198, Jan. 2017, doi: 10.1021/acs.chemmater.6b02939.
[49] R. Sathyamoorthy, K. M. Abhirami, B. Gokul, S. Gautam, K. H. Chae, and K. Asokan, "Fabrication of p-n junction diode using SnO/SnO2 thin films and its device characteristics," *Electronic Materials Letters*, vol. 10, no. 4, pp. 743–747, Jul. 2014, doi: 10.1007/s13391-013-3297-6.
[50] S. N. Habisreutinger, B. Wenger, H. J. Snaith, and R. J. Nicholas, "Dopant-Free Planar n–i–p Perovskite Solar Cells with Steady-State Efficiencies Exceeding 18%," *ACS Energy Letters*, vol. 2, no. 3, pp. 622–628, Mar. 2017, doi: 10.1021/acsenergylett.7b00028.
[51] X. Lan *et al.*, "10.6% Certified Colloidal Quantum Dot Solar Cells via Solvent-Polarity-Engineered Halide Passivation," *Nano Letters*, vol. 16, no. 7, pp. 4630–4634, Jul. 2016, doi: 10.1021/acs.nanolett.6b01957.
[52] X. Lan *et al.*, "Passivation Using Molecular Halides Increases Quantum Dot Solar Cell Performance," *Advanced Materials*, vol. 28, no. 2, pp. 299–304, Jan. 2016, doi: 10.1002/adma.201503657.
[53] N. Zhang *et al.*, "Narrow Band Gap Lead Sulfide Hole Transport Layers for Quantum Dot Photovoltaics," *ACS Applied Materials & Interfaces*, vol. 8, no. 33, pp. 21417–21422, Aug. 2016, doi: 10.1021/acsami.6b01018.
[54] D. C. J. Neo *et al.*, "Poly(3-hexylthiophene-2,5-diyl) as a Hole Transport Layer for Colloidal Quantum Dot Solar Cells," *ACS Applied Materials & Interfaces*, vol. 8, no. 19, pp. 12101–12108, May 2016, doi: 10.1021/acsami.5b10228.
[55] P. R. Brown *et al.*, "Energy Level Modification in Lead Sulfide Quantum Dot Thin Films through Ligand Exchange," *ACS Nano*, vol. 8, no. 6, pp. 5863–5872, Jun. 2014, doi: 10.1021/nn500897c.
[56] C.-H. M. Chuang, P. R. Brown, V. Bulović, and M. G. Bawendi, "Improved performance and stability in quantum dot solar cells through band alignment engineering," *Nature Materials*, vol. 13, no. 8, pp. 796–801, May 2014, doi: 10.1038/nmat3984.
[57] D. Park and S. Yim, "Cascaded band alignments of PbS heterojunction layers for improved performance of PbS quantum dot solar cells," *Solar Energy Materials and Solar Cells*, vol. 208, p. 110363, May 2020, doi: 10.1016/j.solmat.2019.110363.
[58] I. J. Kramer, L. Levina, R. Debnath, D. Zhitomirsky, and E. H. Sargent, "Solar Cells Using Quantum Funnels," *Nano Letters*, vol. 11, no. 9, pp. 3701–3706, Sep. 2011, doi: 10.1021/nl201682h.
[59] D. C. J. Neo, S. D. Stranks, G. E. Eperon, H. J. Snaith, H. E. Assender, and A. A. R. Watt, "Quantum funneling in blended multi-band gap core/shell colloidal quantum dot solar cells," *Applied Physics Letters*, vol. 107, no. 10, p. 103902, Sep. 2015, doi: 10.1063/1.4930144.
[60] E. H. Sargent, "Colloidal quantum dot solar cells," *Nature photonics*, vol. 6, no. 3, pp. 133–135, 2012.
[61] J. C. Ondry, S. Robbennolt, H. Kang, Y. Yan, and S. H. Tolbert, "A Room-Temperature, Solution Phase Method for the Synthesis of Mesoporous Metal Chalcogenide Nanocrystal-Based Thin Films with Precisely Controlled Grain Sizes," *Chemistry of Materials*, vol. 28, no. 17, pp. 6105–6117, Sep. 2016, doi: 10.1021/acs.chemmater.6b01681.
[62] C. Cheng *et al.*, "Polystyrene Templated Porous Titania Wells for Quantum Dot Heterojunction Solar Cells," *ACS Applied Materials & Interfaces*, vol. 6, no. 16, pp. 14247–14252, Aug. 2014, doi: 10.1021/am503558q.
[63] J. Jean *et al.*, "ZnO Nanowire Arrays for Enhanced Photocurrent in PbS Quantum Dot Solar Cells," *Advanced Materials*, vol. 25, no. 20, pp. 2790–2796, May 2013, doi: 10.1002/adma.201204192.

[64] L. Vayssieres, K. Keis, S.-E. Lindquist, and A. Hagfeldt, “Purpose-Built Anisotropic Metal Oxide Material: 3D Highly Oriented Microrod Array of ZnO,” *The Journal of Physical Chemistry B*, vol. 105, no. 17, pp. 3350–3352, May 2001, doi: 10.1021/jp010026s.
[65] E. Marino *et al.*, “Controlling Superstructure–Property Relationships via Critical Casimir Assembly of Quantum Dots,” *J. Phys. Chem. C*, vol. 123, no. 22, pp. 13451–13457, Jun. 2019, doi: 10.1021/acs.jpcc.9b02033.
[66] T. Kawawaki *et al.*, “Efficiency Enhancement of PbS Quantum Dot/ZnO Nanowire Bulk-Heterojunction Solar Cells by Plasmonic Silver Nanocubes,” *ACS Nano*, vol. 9, no. 4, pp. 4165–4172, Apr. 2015, doi: 10.1021/acsnano.5b00321.
[67] S. Pradhan, A. Stavrinadis, S. Gupta, S. Christodoulou, and G. Konstantatos, “Breaking the Open-circuit Voltage Deficit Floor in PbS Quantum Dot Solar Cells Through Synergistic Ligand and Architecture Engineering,” *ACS Energy Letters*, 2017, Accessed: Jun. 05, 2017. [Online]. Available: http://pubs.acs.org/doi/abs/10.1021/acsenergylett.7b00244
[68] W. U. Huynh, J. J. Dittmer, and A. P. Alivisatos, “Hybrid nanorod-polymer solar cells,” *science*, vol. 295, no. 5564, pp. 2425–2427, 2002.
[69] J. Gong, K. Sumathy, Q. Qiao, and Z. Zhou, “Review on dye-sensitized solar cells (DSSCs): Advanced techniques and research trends,” *Renewable and Sustainable Energy Reviews*, vol. 68, pp. 234–246, Feb. 2017, doi: 10.1016/j.rser.2016.09.097.
[70] S. Ren *et al.*, “Inorganic–Organic Hybrid Solar Cell: Bridging Quantum Dots to Conjugated Polymer Nanowires,” *Nano Letters*, vol. 11, no. 9, pp. 3998–4002, Sep. 2011, doi: 10.1021/nl202435t.
[71] W. M. Kochemba, D. L. Pickel, B. G. Sumpter, J. Chen, and S. M. Kilbey, “In Situ Formation of Pyridyl-Functionalized Poly(3-hexylthiophene)s via Quenching of the Grignard Metathesis Polymerization: Toward Ligands for Semiconductor Quantum Dots,” *Chemistry of Materials*, vol. 24, no. 22, pp. 4459–4467, Nov. 2012, doi: 10.1021/cm302915h.
[72] B.-R. Hyun *et al.*, “Electron Injection from PbS Quantum Dots into Titanium Dioxide Nanoparticles,” p. 6.
[73] I. Robel, M. Kuno, and P. V. Kamat, “Size-Dependent Electron Injection from Excited CdSe Quantum Dots into TiO_2 Nanoparticles,” *Journal of the American Chemical Society*, vol. 129, no. 14, pp. 4136–4137, Apr. 2007, doi: 10.1021/ja070099a.
[74] G. Shi *et al.*, “Stable and Highly Efficient PbS Quantum Dot Tandem Solar Cells Employing a Rationally Designed Recombination Layer,” *Advanced Energy Materials*, p. 1602667, Apr. 2017, doi: 10.1002/aenm.201602667.
[75] R. W. Crisp *et al.*, “Tandem Solar Cells from Solution-Processed CdTe and PbS Quantum Dots Using a ZnTe–ZnO Tunnel Junction,” *Nano Letters*, vol. 17, no. 2, pp. 1020–1027, Feb. 2017, doi: 10.1021/acs.nanolett.6b04423.
[76] T. Kim *et al.*, “Hybrid tandem quantum dot/organic photovoltaic cells with complementary near infrared absorption,” *Applied Physics Letters*, vol. 110, no. 22, p. 223903, May 2017, doi: 10.1063/1.4984023.
[77] A. Luque and A. Martí, “Increasing the Efficiency of Ideal Solar Cells by Photon Induced Transitions at Intermediate Levels,” *Phys. Rev. Lett.*, vol. 78, no. 26, pp. 5014–5017, Jun. 1997, doi: 10.1103/PhysRevLett.78.5014.
[78] E. López *et al.*, “Demonstration of the operation principles of intermediate band solar cells at room temperature,” *Solar Energy Materials and Solar Cells*, vol. 149, pp. 15–18, May 2016, doi: 10.1016/j.solmat.2015.12.031.
[79] H. Boustanji, S. Jaziri, and J.-L. Lazzari, “Contribution of a single quantum dots layer in intermediate band solar cells: A capacitance analysis,” *Solar Energy Materials and Solar Cells*, vol. 159, pp. 633–639, Jan. 2017, doi: 10.1016/j.solmat.2016.03.038.

[80] L. Cuadra, A. Marti, and A. Luque, “Type II broken band heterostructure quantum dot to obtain a material for the intermediate band solar cell,” *Physica E*, vol. 14, pp. 162–165, 2002.
[81] A. André, M. Weber, K. M. Wurst, S. Maiti, F. Schreiber, and M. Scheele, “Electron-Conducting PbS Nanocrystal Superlattices with Long-Range Order Enabled by Terthiophene Molecular Linkers,” *ACS Applied Materials & Interfaces*, vol. 10, no. 29, pp. 24708–24714, Jul. 2018, doi: 10.1021/acsami.8b06044.
[82] M. Sainato *et al.*, “Long-Range Order in Nanocrystal Assemblies Determines Charge Transport of Films,” *ACS Omega*, vol. 2, no. 7, pp. 3681–3690, Jul. 2017, doi: 10.1021/acsomega.7b00433.
[83] J.-H. Choi *et al.*, “Bandlike Transport in Strongly Coupled and Doped Quantum Dot Solids: A Route to High-Performance Thin-Film Electronics,” *Nano Letters*, vol. 12, no. 5, pp. 2631–2638, May 2012, doi: 10.1021/nl301104z.
[84] C. R. Kagan and C. B. Murray, “Charge transport in strongly coupled quantum dot solids,” *Nature Nanotechnology*, vol. 10, no. 12, pp. 1013–1026, Nov. 2015, doi: 10.1038/nnano.2015.247.
[85] R. H. Gilmore *et al.*, “Inverse Temperature Dependence of Charge Carrier Hopping in Quantum Dot Solids,” *ACS Nano*, vol. 12, no. 8, pp. 7741–7749, Aug. 2018, doi: 10.1021/acsnano.8b01643.
[86] S. D. Baranovskii, “Theoretical description of charge transport in disordered organic semiconductors: Charge transport in disordered organic semiconductors,” *Phys. Status Solidi B*, vol. 251, no. 3, pp. 487–525, Mar. 2014, doi: 10.1002/pssb.201350339.
[87] D. Yu, C. Wang, B. L. Wehrenberg, and P. Guyot-Sionnest, “Variable Range Hopping Conduction in Semiconductor Nanocrystal Solids,” *Phys. Rev. Lett.*, vol. 92, no. 21, p. 216802, May 2004, doi: 10.1103/PhysRevLett.92.216802.
[88] A. L. Efros and B. I. Shklovskii, “Coulomb gap and low temperature conductivity of disordered systems,” p. 4.
[89] D. L. Dexter, “A Theory of Sensitized Luminescence in Solids,” *The Journal of Chemical Physics*, vol. 21, no. 5, pp. 836–850, May 1953, doi: 10.1063/1.1699044.
[90] Y. Zhang and Z. Xu, “Direct observation of the size dependence of Dexter energy transfer from polymer to small PbS quantum dots,” *Applied Physics Letters*, vol. 93, no. 8, p. 083106, Aug. 2008, doi: 10.1063/1.2975847.
[91] C. R. Kagan, C. B. Murray, M. Nirmal, and M. G. Bawendi, “Electronic Energy Transfer in CdSe Quantum Dot Solids,” *PHYSICAL REVIEW LETTERS*, vol. 76, no. 9, p. 4, 1996.
[92] M. Cardoso Dos Santos, W. R. Algar, I. L. Medintz, and N. Hildebrandt, “Quantum dots for Förster Resonance Energy Transfer (FRET),” *TrAC Trends in Analytical Chemistry*, vol. 125, p. 115819, Apr. 2020, doi: 10.1016/j.trac.2020.115819.
[93] S. W. Clark, J. M. Harbold, and F. W. Wise, “Resonant Energy Transfer in PbS Quantum Dots,” *The Journal of Physical Chemistry C*, vol. 111, no. 20, pp. 7302–7305, May 2007, doi: 10.1021/jp0713561.
[94] G. A. Jones and D. S. Bradshaw, “Resonance Energy Transfer: From Fundamental Theory to Recent Applications,” *Frontiers in Physics*, vol. 7, Jul. 2019, doi: 10.3389/fphy.2019.00100.
[95] A. L. Rogach, “Fluorescence energy transfer in hybrid structures of semiconductor nanocrystals,” *Nano Today*, vol. 6, no. 4, pp. 355–365, Aug. 2011, doi: 10.1016/j.nantod.2011.06.001.
[96] A. Wagenpfahl, “Mobility dependent recombination models for organic solar cells,” *J. Phys.: Condens. Matter*, vol. 29, no. 37, p. 373001, Sep. 2017, doi: 10.1088/1361-648X/aa7952.
[97] A. V. Nenashev, J. O. Oelerich, and S. D. Baranovskii, “Theoretical tools for the description of charge transport in disordered organic semiconductors,” *J. Phys.: Condens. Matter*, vol. 27, no. 9, p. 093201, Mar. 2015, doi: 10.1088/0953-8984/27/9/093201.
[98] R. A. Marcus, “Chemical and Electrochemical Electron-Transfer Theory,” *Annu. Rev. Phys. Chem.*, vol. 15, no. 1, pp. 155–196, Oct. 1964, doi: 10.1146/annurev.pc.15.100164.001103.

[99] N. Lu, L. Li, W. Banerjee, P. Sun, N. Gao, and M. Liu, “Charge carrier hopping transport based on Marcus theory and variable-range hopping theory in organic semiconductors,” *Journal of Applied Physics*, vol. 118, no. 4, p. 045701, Jul. 2015, doi: 10.1063/1.4927334.
[100] N. Lu, L. Li, D. Geng, and M. Liu, “A review for polaron dependent charge transport in organic semiconductor,” *Organic Electronics*, vol. 61, pp. 223–234, Oct. 2018, doi: 10.1016/j.orgel.2018.05.053.
[101] T. Upreti, Y. Wang, H. Zhang, D. Scheunemann, F. Gao, and M. Kemerink, “Experimentally Validated Hopping-Transport Model for Energetically Disordered Organic Semiconductors,” *Phys. Rev. Applied*, vol. 12, no. 6, p. 064039, Dec. 2019, doi: 10.1103/PhysRevApplied.12.064039.
[102] V. I. Arkhipov *et al.*, “Polaron effects on thermally stimulated photoluminescence in disordered organic systems,” *Phys. Rev. B*, vol. 65, no. 16, p. 165218, Apr. 2002, doi: 10.1103/PhysRevB.65.165218.
[103] J. A. Carr, M. Elshobaki, and S. Chaudhary, “Deep defects and the attempt to escape frequency in organic photovoltaic materials,” *Appl. Phys. Lett.*, vol. 107, no. 20, p. 203302, Nov. 2015, doi: 10.1063/1.4936160.
[104] I. I. Fishchuk *et al.*, “Unified description for hopping transport in organic semiconductors including both energetic disorder and polaronic contributions,” *Phys. Rev. B*, vol. 88, no. 12, p. 125202, Sep. 2013, doi: 10.1103/PhysRevB.88.125202.
[105] A. M. Steiner, F. Lissel, A. Fery, J. Lauth, and M. Scheele, “Prospects of Coupled Organic-Inorganic Nanostructures for Charge and Energy Transfer Applications,” *Angew. Chem. Int. Ed.*, p. anie.201916402, Mar. 2020, doi: 10.1002/anie.201916402.
[106] W. J. Bowman, K. March, C. A. Hernandez, and P. A. Crozier, “Measuring bandgap states in individual non-stoichiometric oxide nanoparticles using monochromated STEM EELS: The Praseodymium–ceria case,” *Ultramicroscopy*, vol. 167, pp. 5–10, Aug. 2016, doi: 10.1016/j.ultramic.2016.04.009.
[107] D. Kim, D.-H. Kim, J.-H. Lee, and J. C. Grossman, “Impact of Stoichiometry on the Electronic Structure of PbS Quantum Dots,” *Physical Review Letters*, vol. 110, no. 19, May 2013, doi: 10.1103/PhysRevLett.110.196802.
[108] A. J. Houtepen, Z. Hens, J. S. Owen, and I. Infante, “On the Origin of Surface Traps in Colloidal II–VI Semiconductor Nanocrystals,” *Chemistry of Materials*, vol. 29, no. 2, pp. 752–761, Jan. 2017, doi: 10.1021/acs.chemmater.6b04648.
[109] Y. Zhang *et al.*, “Molecular Oxygen Induced in-Gap States in PbS Quantum Dots,” *ACS Nano*, vol. 9, no. 10, pp. 10445–10452, Oct. 2015, doi: 10.1021/acsnano.5b04677.
[110] D. Zherebetskyy *et al.*, “Hydroxylation of the surface of PbS nanocrystals passivated with oleic acid,” *Science*, vol. 344, no. 6190, pp. 1380–1384, Jun. 2014, doi: 10.1126/science.1252727.
[111] R. H. Gilmore *et al.*, “Epitaxial Dimers and Auger-Assisted Detrapping in PbS Quantum Dot Solids,” *Matter*, vol. 1, no. 1, pp. 250–265, Jul. 2019, doi: 10.1016/j.matt.2019.05.015.
[112] B. Sun *et al.*, “Ligand-Assisted Reconstruction of Colloidal Quantum Dots Decreases Trap State Density,” *Nano Lett.*, p. acs.nanolett.0c00638, Apr. 2020, doi: 10.1021/acs.nanolett.0c00638.
[113] N. B. Pendyala and K. S. R. Koteswara Rao, “Identification of surface states in PbS quantum dots by temperature dependent photoluminescence,” *Journal of Luminescence*, vol. 128, no. 11, pp. 1826–1830, Nov. 2008, doi: 10.1016/j.jlumin.2008.05.004.
[114] Y. Xia *et al.*, “Facet Control for Trap-State Suppression in Colloidal Quantum Dot Solids,” *Adv. Funct. Mater.*, p. 2000594, Apr. 2020, doi: 10.1002/adfm.202000594.
[115] J.-S. Lee, M. V. Kovalenko, J. Huang, D. S. Chung, and D. V. Talapin, “Band-like transport, high electron mobility and high photoconductivity in all-inorganic nanocrystal arrays,” *Nature Nanotechnology*, vol. 6, no. 6, pp. 348–352, Jun. 2011, doi: 10.1038/nnano.2011.46.

[116] M. Scheele, “To Be or not to Be: Band-Like Transport in Quantum Dot Solids,” *Zeitschrift für Physikalische Chemie*, vol. 229, no. 1–2, Jan. 2015, doi: 10.1515/zpch-2014-0587.
[117] F. M. Gómez-Campos, S. Rodríguez-Bolívar, and M. Califano, “High-Mobility Toolkit for Quantum Dot Films,” *ACS Photonics*, vol. 3, no. 11, pp. 2059–2067, Nov. 2016, doi: 10.1021/acsphotonics.6b00377.
[118] M. J. Greaney *et al.*, “Effects of interfacial ligand type on hybrid P3HT:CdSe quantum dot solar cell device parameters,” *J. Chem. Phys.*, vol. 151, no. 7, p. 074704, Aug. 2019, doi: 10.1063/1.5114932.
[119] K. V. Vokhmintcev, P. S. Samokhvalov, and I. Nabiev, “Charge transfer and separation in photoexcited quantum dot-based systems,” *Nano Today*, vol. 11, no. 2, pp. 189–211, Apr. 2016, doi: 10.1016/j.nantod.2016.04.005.
[120] J.-S. Chen, M. Li, and M. Cotlet, “Nanoscale Photoinduced Charge Transfer with Individual Quantum Dots: Tunability through Synthesis, Interface Design, and Interaction with Charge Traps,” *ACS Omega*, vol. 4, no. 5, pp. 9102–9112, May 2019, doi: 10.1021/acsomega.9b00803.
[121] V. Gray *et al.*, “Direct vs Delayed Triplet Energy Transfer from Organic Semiconductors to Quantum Dots and Implications for Luminescent Harvesting of Triplet Excitons,” *ACS Nano*, Mar. 2020, doi: 10.1021/acsnano.9b09339.
[122] H. Wang *et al.*, “Charge Carrier Conduction Mechanism in PbS Quantum Dot Solar Cells: Electrochemical Impedance Spectroscopy Study,” *ACS Applied Materials & Interfaces*, vol. 8, no. 28, pp. 18526–18533, Jul. 2016, doi: 10.1021/acsami.6b03198.
[123] X. Li, Z. Huang, R. Zavala, and M. L. Tang, “Distance-Dependent Triplet Energy Transfer between CdSe Nanocrystals and Surface Bound Anthracene,” *The Journal of Physical Chemistry Letters*, vol. 7, no. 11, pp. 1955–1959, Jun. 2016, doi: 10.1021/acs.jpclett.6b00761.
[124] H. Choi, P. K. Santra, and P. V. Kamat, “Synchronized Energy and Electron Transfer Processes in Covalently Linked CdSe–Squaraine Dye–TiO_2 Light Harvesting Assembly,” *ACS Nano*, vol. 6, no. 6, pp. 5718–5726, Jun. 2012, doi: 10.1021/nn301982e.
[125] Q. Zhang, T. Atay, J. R. Tischler, M. S. Bradley, V. Bulović, and A. V. Nurmikko, “Highly efficient resonant coupling of optical excitations in hybrid organic/inorganic semiconductor nanostructures,” *Nature Nanotech*, vol. 2, no. 9, pp. 555–559, Sep. 2007, doi: 10.1038/nnano.2007.253.
[126] W. R. Algar *et al.*, “Concurrent Modulation of Quantum Dot Photoluminescence Using a Combination of Charge Transfer and Förster Resonance Energy Transfer: Competitive Quenching and Multiplexed Biosensing Modality,” *J. Am. Chem. Soc.*, vol. 139, no. 1, pp. 363–372, Jan. 2017, doi: 10.1021/jacs.6b11042.
[127] A. E. Colbert, E. Jedlicka, W. Wu, and D. S. Ginger, “Subpicosecond Photon-Energy-Dependent Hole Transfer from PbS Quantum Dots to Conjugated Polymers,” *J. Phys. Chem. Lett.*, vol. 7, no. 24, pp. 5150–5155, Dec. 2016, doi: 10.1021/acs.jpclett.6b02490.
[128] A. E. Colbert, “Spectroscopic Characterization of Interfacial Charge Transfer and Recombination in Polymer/Quantum Dot Blends,” University of Washington, 2016.
[129] N. Guijarro *et al.*, “Direct Correlation between Ultrafast Injection and Photoanode Performance in Quantum Dot Sensitized Solar Cells,” *J. Phys. Chem. C*, vol. 114, no. 50, pp. 22352–22360, Dec. 2010, doi: 10.1021/jp108499h.
[130] J. T. Margraf, A. Ruland, V. Sgobba, D. M. Guldi, and T. Clark, “Quantum-Dot-Sensitized Solar Cells: Understanding Linker Molecules through Theory and Experiment,” *Langmuir*, vol. 29, no. 7, pp. 2434–2438, Feb. 2013, doi: 10.1021/la3047609.
[131] M. Tagliazucchi, D. B. Tice, C. M. Sweeney, A. J. Morris-Cohen, and E. A. Weiss, “Ligand-Controlled Rates of Photoinduced Electron Transfer in Hybrid CdSe Nanocrystal/Poly(viologen) Films,” *ACS Nano*, vol. 5, no. 12, pp. 9907–9917, Dec. 2011, doi: 10.1021/nn203683s.

[132] Z. Wang, M. Rafipoor, P. G. Risueño, J.-P. Merkl, H. Lange, and G. Bester, “Phonon-assisted Auger enables ultrafast charge transfer in CdSe Quantum Dot/Organic Molecule,” p. 21, 2019.
[133] P. Zereshki, M. M. Tavakoli, P. Valencia-Acuna, J.-H. Park, J. Kong, and H. Zhao, “Observation of charge transfer in mixed-dimensional heterostructures formed by transition metal dichalcogenide monolayers and PbS quantum dots,” *Phys. Rev. B*, vol. 100, no. 23, p. 235411, Dec. 2019, doi: 10.1103/PhysRevB.100.235411.
[134] B. P. Bloom *et al.*, “Directing Charge Transfer in Quantum Dot Assemblies,” *Acc. Chem. Res.*, vol. 51, no. 10, pp. 2565–2573, Oct. 2018, doi: 10.1021/acs.accounts.8b00355.
[135] A. O. El-Ballouli, E. Alarousu, A. R. Kirmani, A. Amassian, O. M. Bakr, and O. F. Mohammed, “Overcoming the Cut-Off Charge Transfer Bandgaps at the PbS Quantum Dot Interface,” *Advanced Functional Materials*, vol. 25, no. 48, pp. 7435–7441, Dec. 2015, doi: 10.1002/adfm.201504035.
[136] M. Scheele *et al.*, “PbS Nanoparticles Capped with Tetrathiafulvalenetetracarboxylate: Utilizing Energy Level Alignment for Efficient Carrier Transport,” *ACS Nano*, vol. 8, no. 3, pp. 2532–2540, Mar. 2014, doi: 10.1021/nn406127s.
[137] J. Chang *et al.*, “Ligand-dependent exciton dynamics and photovoltaic properties of PbS quantum dot heterojunction solar cells,” *Physical Chemistry Chemical Physics*, vol. 19, no. 9, pp. 6358–6367, 2017, doi: 10.1039/C6CP06561A.
[138] D. Zhitomirsky *et al.*, “Engineering colloidal quantum dot solids within and beyond the mobility-invariant regime,” *Nature Communications*, vol. 5, May 2014, doi: 10.1038/ncomms4803.
[139] R. H. Gilmore, E. M. Y. Lee, M. C. Weidman, A. P. Willard, and W. A. Tisdale, “Charge Carrier Hopping Dynamics in Homogeneously Broadened PbS Quantum Dot Solids,” *Nano Letters*, vol. 17, no. 2, pp. 893–901, Feb. 2017, doi: 10.1021/acs.nanolett.6b04201.
[140] S. Chand, N. Thakur, S. C. Katyal, P. B. Barman, V. Sharma, and P. Sharma, “Recent developments on the synthesis, structural and optical properties of chalcogenide quantum dots,” *Solar Energy Materials and Solar Cells*, vol. 168, pp. 183–200, Aug. 2017, doi: 10.1016/j.solmat.2017.04.033.
[141] C. H. R, J. D. Schiffman, and R. G. Balakrishna, “Quantum dots as fluorescent probes: Synthesis, surface chemistry, energy transfer mechanisms, and applications,” *Sensors and Actuators B: Chemical*, vol. 258, pp. 1191–1214, Apr. 2018, doi: 10.1016/j.snb.2017.11.189.
[142] S. V. Kershaw, A. S. Susha, and A. L. Rogach, “Narrow bandgap colloidal metal chalcogenide quantum dots: synthetic methods, heterostructures, assemblies, electronic and infrared optical properties,” *Chem. Soc. Rev.*, vol. 42, no. 7, p. 3033, 2013, doi: 10.1039/c2cs35331h.
[143] K. K. Nanda and S. N. Sahu, “One-Dimensional Quantum Confinement in Electrodeposited PbS Nanocrystalline Semiconductors,” *Advanced Materials*, vol. 13, no. 4, pp. 280–283, Feb. 2001, doi: 10.1002/1521-4095(200102)13:4<280::AID-ADMA280>3.0.CO;2-T.
[144] G. Savelli, S. Silveira Stein, G. Bernard-Granger, P. Faucherand, and L. Montès, “Monocrystalline molybdenum silicide based quantum dot superlattices grown by chemical vapor deposition,” *Superlattices and Microstructures*, vol. 97, pp. 341–345, Sep. 2016, doi: 10.1016/j.spmi.2016.06.042.
[145] C. E. Reilly, C. Lund, S. Nakamura, U. K. Mishra, S. P. DenBaars, and S. Keller, “Infrared luminescence from N-polar InN quantum dots and thin films grown by metal organic chemical vapor deposition,” *Appl. Phys. Lett.*, vol. 114, no. 24, p. 241103, Jun. 2019, doi: 10.1063/1.5109734.
[146] Y. Golan, B. Alperson, J. L. Hutchison, G. Hodes, and I. Rubinstein, “Electrodeposited quantum dots: Coherent nanocrystalline cdse on oriented polycrystalline au films,” *Adv. Mater.*, vol. 9, no. 3, pp. 236–238, Mar. 1997, doi: 10.1002/adma.19970090310.

[147] Y. Golan, J. L. Hutchison, I. Rubinstein, and G. Hodes, “Epitaxial size control by mismatch tuning in electrodeposited Cd(Se, Te) quantum dots on {111} gold,” *Adv. Mater.*, vol. 8, no. 8, pp. 631–633, Aug. 1996, doi: 10.1002/adma.19960080804.
[148] X.-Y. Yu, J.-Y. Liao, K.-Q. Qiu, D.-B. Kuang, and C.-Y. Su, “Dynamic Study of Highly Efficient CdS/CdSe Quantum Dot-Sensitized Solar Cells Fabricated by Electrodeposition,” *ACS Nano*, vol. 5, no. 12, pp. 9494–9500, Dec. 2011, doi: 10.1021/nn203375g.
[149] M. Hao *et al.*, “Ligand-assisted cation-exchange engineering for high-efficiency colloidal Cs1−xFAxPbI3 quantum dot solar cells with reduced phase segregation,” *Nat Energy*, vol. 5, no. 1, pp. 79–88, Jan. 2020, doi: 10.1038/s41560-019-0535-7.
[150] Y. Xia *et al.*, “Cation-Exchange Synthesis of Highly Monodisperse PbS Quantum Dots from ZnS Nanorods for Efficient Infrared Solar Cells,” *Adv. Funct. Mater.*, vol. 30, no. 4, p. 1907379, Jan. 2020, doi: 10.1002/adfm.201907379.
[151] J. Joo *et al.*, “A Reduction Pathway in the Synthesis of PbSe Nanocrystal Quantum Dots,” *J. Am. Chem. Soc.*, vol. 131, no. 30, pp. 10620–10628, Aug. 2009, doi: 10.1021/ja903445f.
[152] L. Cademartiri, J. Bertolotti, R. Sapienza, D. S. Wiersma, G. von Freymann, and G. A. Ozin, “Multigram Scale, Solventless, and Diffusion-Controlled Route to Highly Monodisperse PbS Nanocrystals,” *J. Phys. Chem. B*, vol. 110, no. 2, pp. 671–673, Jan. 2006, doi: 10.1021/jp0563585.
[153] H.-Y. Si, D. Yuan, J.-S. Chen, and G.-M. Chow, “Synthesis of PbS nanocrystals from sulfur–amine solutions at room temperature,” *RSC Advances*, vol. 1, no. 5, p. 817, 2011, doi: 10.1039/c1ra00279a.
[154] M. R. McPhail and E. A. Weiss, “Role of Organosulfur Compounds in the Growth and Final Surface Chemistry of PbS Quantum Dots,” *Chemistry of Materials*, vol. 26, no. 11, pp. 3377–3384, Jun. 2014, doi: 10.1021/cm4040819.
[155] Z. Huang *et al.*, “Low cost and large scale synthesis of PbS quantum dots with hybrid surface passivation,” *CrystEngComm*, vol. 19, no. 6, pp. 946–951, 2017, doi: 10.1039/C6CE02471H.
[156] I. Moreels, Y. Justo, B. De Geyter, K. Haustraete, J. C. Martins, and Z. Hens, “Size-Tunable, Bright, and Stable PbS Quantum Dots: A Surface Chemistry Study,” *ACS Nano*, vol. 5, no. 3, pp. 2004–2012, Mar. 2011, doi: 10.1021/nn103050w.
[157] M. Yuan *et al.*, “High-Performance Quantum-Dot Solids via Elemental Sulfur Synthesis,” *Adv. Mater.*, vol. 26, no. 21, pp. 3513–3519, Jun. 2014, doi: 10.1002/adma.201305912.
[158] A. A. R. Watt *et al.*, “Lead sulfide nanocrystal: conducting polymer solar cells,” *Journal of Physics D: Applied Physics*, vol. 38, no. 12, pp. 2006–2012, Jun. 2005, doi: 10.1088/0022-3727/38/12/023.
[159] J. Zhang, J. Gao, E. M. Miller, J. M. Luther, and M. C. Beard, “Diffusion-Controlled Synthesis of PbS and PbSe Quantum Dots with *in Situ* Halide Passivation for Quantum Dot Solar Cells,” *ACS Nano*, vol. 8, no. 1, pp. 614–622, Jan. 2014, doi: 10.1021/nn405236k.
[160] J. Zhang, R. W. Crisp, J. Gao, D. M. Kroupa, M. C. Beard, and J. M. Luther, “Synthetic Conditions for High-Accuracy Size Control of PbS Quantum Dots,” *The Journal of Physical Chemistry Letters*, vol. 6, no. 10, pp. 1830–1833, May 2015, doi: 10.1021/acs.jpclett.5b00689.
[161] M. C. Weidman, Q. Nguyen, D.-M. Smilgies, and W. A. Tisdale, “Impact of Size Dispersity, Ligand Coverage, and Ligand Length on the Structure of PbS Nanocrystal Superlattices,” *Chemistry of Materials*, vol. 30, no. 3, pp. 807–816, Feb. 2018, doi: 10.1021/acs.chemmater.7b04322.
[162] M. C. Weidman, K. G. Yager, and W. A. Tisdale, “Interparticle Spacing and Structural Ordering in Superlattice PbS Nanocrystal Solids Undergoing Ligand Exchange,” *Chemistry of Materials*, vol. 27, no. 2, pp. 474–482, Jan. 2015, doi: 10.1021/cm503626s.
[163] L. K. Sagar, W. Walravens, Q. Zhao, A. Vantomme, P. Geiregat, and Z. Hens, “PbS/CdS Core/Shell Quantum Dots by Additive, Layer-by-Layer Shell Growth,” *Chemistry of Materials*, vol. 28, no. 19, pp. 6953–6959, Oct. 2016, doi: 10.1021/acs.chemmater.6b02638.

[164] D. C. J. Neo *et al.*, "Influence of Shell Thickness and Surface Passivation on PbS/CdS Core/Shell Colloidal Quantum Dot Solar Cells," *Chemistry of Materials*, vol. 26, no. 13, pp. 4004–4013, Jul. 2014, doi: 10.1021/cm501595u.
[165] D. Dorfs *et al.*, "Type-I and Type-II Nanoscale Heterostructures Based on CdTe Nanocrystals: A Comparative Study," *Small*, vol. 4, no. 8, pp. 1148–1152, Aug. 2008, doi: 10.1002/smll.200800287.
[166] M. Nasilowski, L. Nienhaus, S. N. Bertram, and M. G. Bawendi, "Colloidal atomic layer deposition growth of PbS/CdS core/shell quantum dots," *Chem. Commun.*, vol. 53, no. 5, pp. 869–872, 2017, doi: 10.1039/C6CC07403K.
[167] S. Jiao *et al.*, "Band Engineering in Core/Shell ZnTe/CdSe for Photovoltage and Efficiency Enhancement in Exciplex Quantum Dot Sensitized Solar Cells," *ACS Nano*, vol. 9, no. 1, pp. 908–915, Jan. 2015, doi: 10.1021/nn506638n.
[168] A. Jain, O. Voznyy, S. Hoogland, M. Korkusinski, P. Hawrylak, and E. H. Sargent, "Atomistic Design of CdSe/CdS Core–Shell Quantum Dots with Suppressed Auger Recombination," *Nano Letters*, vol. 16, no. 10, pp. 6491–6496, Oct. 2016, doi: 10.1021/acs.nanolett.6b03059.
[169] F. Ren *et al.*, "Towards understanding the unusual photoluminescence intensity variation of ultrasmall colloidal PbS quantum dots with the formation of a thin CdS shell," *Phys. Chem. Chem. Phys.*, vol. 18, no. 46, pp. 31828–31835, 2016, doi: 10.1039/C6CP05786A.
[170] Z. Fan, L.-C. Lin, W. Buijs, T. J. H. Vlugt, and M. A. van Huis, "Atomistic understanding of cation exchange in PbS nanocrystals using simulations with pseudoligands," *Nature Communications*, vol. 7, p. 11503, May 2016, doi: 10.1038/ncomms11503.
[171] M. L. H. Green, "A new approach to the formal classification of covalent compounds of the elements," *Journal of organometallic chemistry*, vol. 500, no. 1–2, pp. 127–148, 1995.
[172] C. Giansante, I. Infante, E. Fabiano, R. Grisorio, G. P. Suranna, and G. Gigli, "'Darker-than-Black' PbS Quantum Dots: Enhancing Optical Absorption of Colloidal Semiconductor Nanocrystals via Short Conjugated Ligands," *Journal of the American Chemical Society*, vol. 137, no. 5, pp. 1875–1886, Feb. 2015, doi: 10.1021/ja510739q.
[173] R. Grisorio, D. Debellis, G. P. Suranna, G. Gigli, and C. Giansante, "The Dynamic Organic/Inorganic Interface of Colloidal PbS Quantum Dots," *Angewandte Chemie International Edition*, vol. 55, no. 23, pp. 6628–6633, Jun. 2016, doi: 10.1002/anie.201511174.
[174] M. A. Abbas *et al.*, "Revival of Solar Paint Concept: Air-Processable Solar Paints for the Fabrication of Quantum Dot-Sensitized Solar Cells," *The Journal of Physical Chemistry C*, Aug. 2017, doi: 10.1021/acs.jpcc.7b05207.
[175] P. K. Santra, A. F. Palmstrom, J. T. Tanskanen, N. Yang, and S. F. Bent, "Improving Performance in Colloidal Quantum Dot Solar Cells by Tuning Band Alignment through Surface Dipole Moments," *The Journal of Physical Chemistry C*, vol. 119, no. 6, pp. 2996–3005, Feb. 2015, doi: 10.1021/acs.jpcc.5b00341.
[176] D. M. Kroupa *et al.*, "Tuning colloidal quantum dot band edge positions through solution-phase surface chemistry modification," *Nature Communications*, vol. 8, p. 15257, May 2017, doi: 10.1038/ncomms15257.
[177] Q. Lin *et al.*, "Phase-Transfer Ligand Exchange of Lead Chalcogenide Quantum Dots for Direct Deposition of Thick, Highly Conductive Films," *Journal of the American Chemical Society*, vol. 139, no. 19, pp. 6644–6653, May 2017, doi: 10.1021/jacs.7b01327.
[178] M. J. Turo and J. E. Macdonald, "Crystal-Bound *vs* Surface-Bound Thiols on Nanocrystals," *ACS Nano*, vol. 8, no. 10, pp. 10205–10213, Oct. 2014, doi: 10.1021/nn5032164.
[179] K. Singh and O. Voznyy, "It's a Trap! Fused Quantum Dots Are Undesired Defects in Thin-Film Solar Cells," *Chem*, vol. 5, no. 7, pp. 1692–1694, Jul. 2019, doi: 10.1016/j.chempr.2019.06.015.

[180] Y. Cao, A. Stavrinadis, T. Lasanta, D. So, and G. Konstantatos, “The role of surface passivation for efficient and photostable PbS quantum dot solar cells,” *Nature Energy*, vol. 1, no. 4, p. 16035, Apr. 2016, doi: 10.1038/nenergy.2016.35.
[181] A. F. Fidler, J. Gao, and V. I. Klimov, “Electron–hole exchange blockade and memory-less recombination in photoexcited films of colloidal quantum dots,” *Nature Physics*, Mar. 2017, doi: 10.1038/nphys4073.
[182] G. W. Hwang *et al.*, “Identifying and Eliminating Emissive Sub-bandgap States in Thin Films of PbS Nanocrystals,” *Adv. Mater.*, vol. 27, no. 30, pp. 4481–4486, Aug. 2015, doi: 10.1002/adma.201501156.
[183] S. A. McDonald *et al.*, “Solution-processed PbS quantum dot infrared photodetectors and photovoltaics,” *Nature Materials*, vol. 4, no. 2, pp. 138–142, Feb. 2005, doi: 10.1038/nmat1299.
[184] E. J. D. Klem, D. D. MacNeil, P. W. Cyr, L. Levina, and E. H. Sargent, “Efficient solution-processed infrared photovoltaic cells: Planarized all-inorganic bulk heterojunction devices via inter-quantum-dot bridging during growth from solution,” *Appl. Phys. Lett.*, vol. 90, no. 18, p. 183113, Apr. 2007, doi: 10.1063/1.2735674.
[185] E. J. D. Klem, H. Shukla, S. Hinds, D. D. MacNeil, L. Levina, and E. H. Sargent, “Impact of dithiol treatment and air annealing on the conductivity, mobility, and hole density in PbS colloidal quantum dot solids,” *Appl. Phys. Lett.*, vol. 92, no. 21, p. 212105, May 2008, doi: 10.1063/1.2917800.
[186] N. Nakazawa *et al.*, “The interparticle distance limit for multiple exciton dissociation in PbS quantum dot solid films,” *Nanoscale Horiz.*, vol. 4, no. 2, pp. 445–451, 2019, doi: 10.1039/C8NH00341F.
[187] A. Shestha, Y. Yin, G. G. Andersson, N. A. Spooner, S. Qiao, and S. Dai, “Versatile PbS Quantum Dot Ligand Exchange Systems in the Presence of Pb-Thiolates,” *Small*, vol. 13, no. 5, p. 1602956, Feb. 2017, doi: 10.1002/smll.201602956.
[188] M. Law, J. M. Luther, Q. Song, B. K. Hughes, C. L. Perkins, and A. J. Nozik, “Structural, Optical, and Electrical Properties of PbSe Nanocrystal Solids Treated Thermally or with Simple Amines,” *J. Am. Chem. Soc.*, vol. 130, no. 18, pp. 5974–5985, Apr. 2008, doi: 10.1021/ja800040c.
[189] A. Hassinen, I. Moreels, K. De Nolf, P. F. Smet, J. C. Martins, and Z. Hens, “Short-Chain Alcohols Strip X-Type Ligands and Quench the Luminescence of PbSe and CdSe Quantum Dots, Acetonitrile Does Not,” *Journal of the American Chemical Society*, vol. 134, no. 51, pp. 20705–20712, Dec. 2012, doi: 10.1021/ja308861d.
[190] D. Becker-Koch *et al.*, “Ligand dependent oxidation dictates the performance evolution of high efficiency PbS quantum dot solar cells,” *Sustainable Energy Fuels*, vol. 4, no. 1, pp. 108–115, 2020, doi: 10.1039/C9SE00602H.
[191] C. Ding *et al.*, “Passivation Strategy of Reducing Both Electron and Hole Trap States for Achieving High-Efficiency PbS Quantum-Dot Solar Cells with Power Conversion Efficiency over 12%,” *ACS Energy Lett.*, vol. 5, no. 10, pp. 3224–3236, Oct. 2020, doi: 10.1021/acsenergylett.0c01561.
[192] A. H. Ip *et al.*, “Hybrid passivated colloidal quantum dot solids,” *Nature Nanotechnology*, vol. 7, no. 9, pp. 577–582, Sep. 2012, doi: 10.1038/nnano.2012.127.
[193] S. J. Oh *et al.*, “Engineering the surface chemistry of lead chalcogenide nanocrystal solids to enhance carrier mobility and lifetime in optoelectronic devices,” *Chem. Commun.*, vol. 53, no. 4, pp. 728–731, 2017, doi: 10.1039/C6CC07916D.
[194] R. W. Crisp *et al.*, “Metal Halide Solid-State Surface Treatment for High Efficiency PbS and PbSe QD Solar Cells,” *Scientific Reports*, vol. 5, no. 1, Sep. 2015, doi: 10.1038/srep09945.
[195] A. Kiani *et al.*, “Single-step colloidal quantum dot films for infrared solar harvesting,” *Applied Physics Letters*, vol. 109, no. 18, p. 183105, Oct. 2016, doi: 10.1063/1.4966217.

[196] L. Hu *et al.*, "Temperature- and ligand-dependent carrier transport dynamics in photovoltaic PbS colloidal quantum dot thin films using diffusion-wave methods," *Solar Energy Materials and Solar Cells*, vol. 164, pp. 135–145, May 2017, doi: 10.1016/j.solmat.2017.02.024.
[197] Z. Yang *et al.*, "Colloidal Quantum Dot Photovoltaics Enhanced by Perovskite Shelling," *Nano Letters*, vol. 15, no. 11, pp. 7539–7543, Nov. 2015, doi: 10.1021/acs.nanolett.5b03271.
[198] E. M. Sanehira *et al.*, "Enhanced mobility CsPbI3 quantum dot arrays for record-efficiency, high-voltage photovoltaic cells," *Science Advances*, vol. 3, no. 10, p. eaao4204, 2017.
[199] M. Albaladejo-Siguan *et al.*, "Efficient and Stable PbS Quantum Dot Solar Cells by Triple-Cation Perovskite Passivation," *ACS Nano*, vol. 14, no. 1, pp. 384–393, Jan. 2020, doi: 10.1021/acsnano.9b05848.
[200] D. of E. NREL, "Best Research-Cell Efficiency Chart," *National Renewable Energy Laboratory*, Jul. 16, 2022. https://www.nrel.gov/pv/cell-efficiency.html (accessed Apr. 17, 2020).
[201] Ruizhi Wang, Xiaoliang Yan, Xiao Yang, Yuchen Wang, Heng Li, and Chuanxiang Sheng, "Long Lived Photoexcitation Dynamics in π-Conjugated Polymer/PbS Quantum Dot Blended Films for Photovoltaic Application," *Polymers*, vol. 9, no. 12, p. 352, Aug. 2017, doi: 10.3390/polym9080352.
[202] M. L. Waters, "Aromatic interactions in model systems," *Current Opinion in Chemical Biology*, vol. 6, no. 6, pp. 736–741, Dec. 2002, doi: 10.1016/S1367-5931(02)00359-9.
[203] H. K. Bisoyi and S. Kumar, "Liquid-crystal nanoscience: an emerging avenue of soft self-assembly," *Chem. Soc. Rev.*, vol. 40, no. 1, pp. 306–319, 2011, doi: 10.1039/B901793N.
[204] C. Giansante *et al.*, "Colloidal Arenethiolate-Capped PbS Quantum Dots: Optoelectronic Properties, Self-Assembly, and Application in Solution-Cast Photovoltaics," *The Journal of Physical Chemistry C*, vol. 117, no. 25, pp. 13305–13317, Jun. 2013, doi: 10.1021/jp403066q.
[205] S. Bettis Homan, V. K. Sangwan, I. Balla, H. Bergeron, E. A. Weiss, and M. C. Hersam, "Ultrafast Exciton Dissociation and Long-Lived Charge Separation in a Photovoltaic Pentacene–MoS_2 van der Waals Heterojunction," *Nano Lett.*, vol. 17, no. 1, pp. 164–169, Jan. 2017, doi: 10.1021/acs.nanolett.6b03704.
[206] B. Reiser, L. González-García, I. Kanelidis, J. H. M. Maurer, and T. Kraus, "Gold nanorods with conjugated polymer ligands: sintering-free conductive inks for printed electronics," *Chem. Sci.*, vol. 7, no. 7, pp. 4190–4196, 2016, doi: 10.1039/C6SC00142D.
[207] S. Maiti *et al.*, "Dye-Sensitized Ternary Copper Chalcogenide Nanocrystals: Optoelectronic Properties, Air Stability, and Photosensitivity," *Chem. Mater.*, vol. 31, no. 7, pp. 2443–2449, Apr. 2019, doi: 10.1021/acs.chemmater.8b05108.
[208] N. Nishimura, J. R. Allardice, J. Xiao, Q. Gu, V. Gray, and A. Rao, "Photon upconversion utilizing energy beyond the band gap of crystalline silicon with a hybrid TES-ADT/PbS quantum dots system," *Chem. Sci.*, vol. 10, no. 18, pp. 4750–4760, 2019, doi: 10.1039/C9SC00821G.
[209] C. Mongin, P. Moroz, M. Zamkov, and F. N. Castellano, "Thermally activated delayed photoluminescence from pyrenyl-functionalized CdSe quantum dots," *Nature Chem*, vol. 10, no. 2, pp. 225–230, Feb. 2018, doi: 10.1038/nchem.2906.
[210] Z. Huang *et al.*, "Enhanced Near-Infrared-to-Visible Upconversion by Synthetic Control of PbS Nanocrystal Triplet Photosensitizers," *J. Am. Chem. Soc.*, vol. 141, no. 25, pp. 9769–9772, Jun. 2019, doi: 10.1021/jacs.9b03385.
[211] M. Scheele, W. Brütting, and F. Schreiber, "Coupled organic–inorganic nanostructures (COIN)," *Phys. Chem. Chem. Phys.*, vol. 17, no. 1, pp. 97–111, 2015, doi: 10.1039/C4CP03094J.
[212] N. J. Hestand and F. C. Spano, "Expanded Theory of H- and J-Molecular Aggregates: The Effects of Vibronic Coupling and Intermolecular Charge Transfer," *Chem. Rev.*, vol. 118, no. 15, pp. 7069–7163, Aug. 2018, doi: 10.1021/acs.chemrev.7b00581.

[213] B. J. Walker, G. P. Nair, L. F. Marshall, V. Bulović, and M. G. Bawendi, "Narrow-Band Absorption-Enhanced Quantum Dot/J-Aggregate Conjugates," *J. Am. Chem. Soc.*, vol. 131, no. 28, pp. 9624–9625, Jul. 2009, doi: 10.1021/ja902813q.
[214] B. J. Walker, V. Bulović, and M. G. Bawendi, "Quantum Dot/J-Aggregate Blended Films for Light Harvesting and Energy Transfer," *Nano Lett.*, vol. 10, no. 10, pp. 3995–3999, Oct. 2010, doi: 10.1021/nl1018639.
[215] R. Mastria *et al.*, "Role of Polymer in Hybrid Polymer/PbS Quantum Dot Solar Cells," *J. Phys. Chem. C*, vol. 119, no. 27, pp. 14972–14979, Jul. 2015, doi: 10.1021/acs.jpcc.5b03761.
[216] C. Giansante *et al.*, "Molecular-Level Switching of Polymer/Nanocrystal Non-Covalent Interactions and Application in Hybrid Solar Cells," *Adv. Funct. Mater.*, vol. 25, no. 1, pp. 111–119, Jan. 2015, doi: 10.1002/adfm.201401841.
[217] Y. Xue *et al.*, "Toward Scalable PbS Quantum Dot Solar Cells Using a Tailored Polymeric Hole Conductor," *ACS Energy Lett.*, vol. 4, no. 12, pp. 2850–2858, Dec. 2019, doi: 10.1021/acsenergylett.9b02301.
[218] M. Bernechea, N. C. Miller, G. Xercavins, D. So, A. Stavrinadis, and G. Konstantatos, "Solution-processed solar cells based on environmentally friendly AgBiS2 nanocrystals," *Nature Photon*, vol. 10, no. 8, pp. 521–525, Aug. 2016, doi: 10.1038/nphoton.2016.108.
[219] Y. Zhang *et al.*, "Hybrid Quantum Dot/Organic Heterojunction: A Route to Improve Open-Circuit Voltage in PbS Colloidal Quantum Dot Solar Cells," *ACS Energy Lett.*, vol. 5, no. 7, pp. 2335–2342, Jul. 2020, doi: 10.1021/acsenergylett.0c01136.
[220] B.-S. Kim *et al.*, "High Performance PbS Quantum Dot/Graphene Hybrid Solar Cell with Efficient Charge Extraction," *ACS Applied Materials & Interfaces*, vol. 8, no. 22, pp. 13902–13908, Jun. 2016, doi: 10.1021/acsami.6b02544.
[221] Y. Tazawa *et al.*, "Carbon Nanotubes for Quantum Dot Photovoltaics with Enhanced Light Management and Charge Transport," *ACS Photonics*, vol. 5, no. 12, pp. 4854–4863, Dec. 2018, doi: 10.1021/acsphotonics.8b00982.
[222] H.-P. Shi, D.-W. Lin, and R. Wu, "Synthesis of High-Quality Carboxyl End-Functionalized Poly(3-hexylthiophene)/CdSe Nanocomposites," *Journal of Nanomaterials*, vol. 2019, pp. 1–8, Sep. 2019, doi: 10.1155/2019/1251598.
[223] J. Liu, T. Tanaka, K. Sivula, A. P. Alivisatos, and J. M. J. Frechet, "Employing End-Functional Polythiophene To Control the Morphology of Nanocrystal-Polymer Composites in Hybrid Solar Cells," *J. Am. Chem. Soc.*, vol. 126, pp. 6550–6551, Feb. 2004, doi: 10.1145/1961678.1961690.
[224] V. Senkovskyy *et al.*, "'Hairy' Poly(3-hexylthiophene) Particles Prepared via Surface-Initiated Kumada Catalyst-Transfer Polycondensation," *J. Am. Chem. Soc.*, vol. 131, no. 45, pp. 16445–16453, Nov. 2009, doi: 10.1021/ja904885w.
[225] C. Ortiz-Cervantes, P. I. Román-Román, J. Vazquez-Chavez, M. Hernández-Rodríguez, and D. Solis-Ibarra, "Thousand-fold Conductivity Increase in 2D Perovskites by Polydiacetylene Incorporation and Doping," *Angew. Chem. Int. Ed.*, vol. 57, no. 42, pp. 13882–13886, Oct. 2018, doi: 10.1002/anie.201809028.
[226] R. Chauvin and C. Lepetit, "Theoretical Studies on Acetylenic Scaffolds," in *Acetylene Chemistry*, John Wiley & Sons, Ltd, 2005, pp. 1–50. doi: 10.1002/3527605487.ch1.
[227] X. Qian and B. Städler, "Recent Developments in Polydiacetylene-Based Sensors," *Chem. Mater.*, vol. 31, no. 4, pp. 1196–1222, Feb. 2019, doi: 10.1021/acs.chemmater.8b05185.
[228] H. Jiang, G. Hershtig, S. Richter, and R. Jelinek, "Light-Induced Conductivity in a Solution-Processed Film of Polydiacetylene and Perylene Diimide," *J. Phys. Chem. Lett.*, vol. 7, no. 9, pp. 1628–1631, May 2016, doi: 10.1021/acs.jpclett.6b00690.
[229] P. Tanphibal, K. Tashiro, and S. Chirachanchai, "Constructing π-Electron-Conjugated Diarylbutadiyne-Based Polydiacetylene under Molecular Framework Controlled by Hydrogen

Bond and Side-Chain Substituent Position," *Macromol. Rapid Commun.*, vol. 37, no. 8, pp. 685–690, Apr. 2016, doi: 10.1002/marc.201500690.
[230] S. Wu, L. Pan, Y. Huang, N. Yang, and Q. Zhang, "Co-assemblies of polydiacetylenes and metal ions for solvent sensing," *Soft Matter*, vol. 14, no. 33, pp. 6929–6937, 2018, doi: 10.1039/C8SM01282B.
[231] N. Stojanovska, A. De Grazia, M. Tahtouh, R. Shimmon, and B. Reedy, "Refining Fingermark Development using Diacetylene Copolymers on Difficult Surfaces ," *Journal of Forensic Sciences*, vol. 60, no. 3, pp. 619–626, May 2015, doi: 10.1111/1556-4029.12692.
[232] C. Glaser, "Beiträge zur Kenntniss des Acetenylbenzols," *Ber. Dtsch. Chem. Ges.*, vol. 2, no. 1, pp. 422–424, Jan. 1869, doi: 10.1002/cber.186900201183.
[233] W. Shi and A. Lei, "1,3-Diyne chemistry: synthesis and derivations," *Tetrahedron Letters*, vol. 55, no. 17, pp. 2763–2772, Apr. 2014, doi: 10.1016/j.tetlet.2014.03.022.
[234] M. M. Chamberlain, G. A. Jabs, and B. B. Wayland, "Systems Containing a Silicon—Oxygen—Vanadium Linkage [1]," *J. Org. Chem.*, vol. 27, no. 9, pp. 3321–3323, Sep. 1962, doi: 10.1021/jo01056a512.
[235] F. Sondheimer, Y. Amiel, and R. Wolovsky, "Unsaturated Macrocyclic Componds V1. - Large Ring Poly-Acetylenes," *J. Am. Chem. Soc.*, vol. 79, no. 15, pp. 4247–4248, Aug. 1957, doi: 10.1021/ja01572a080.
[236] H. A. Stefani, A. S. Guarezemini, and R. Cella, "Homocoupling reactions of alkynes, alkenes and alkyl compounds," *Tetrahedron*, vol. 66, no. 40, pp. 7871–7918, Oct. 2010, doi: 10.1016/j.tet.2010.07.001.
[237] S.-N. Chen, T.-T. Hung, T.-C. Lin, and F.-Y. Tsai, "Reusable and Efficient CuI/TBAB-Catalyzed Iodination of Terminal Alkynes in Water under Air," *Journal of the Chinese Chemical Society*, vol. 56, no. 5, pp. 1078–1081, Oct. 2009, doi: 10.1002/jccs.200900156.
[238] S.-N. Chen, W.-Y. Wu, and F.-Y. Tsai, "Homocoupling reaction of terminal alkynes catalyzed by a reusable cationic 2,2'-bipyridyl palladium(II)/CuI system in water," *Green Chem.*, vol. 11, no. 2, pp. 269–274, 2009, doi: 10.1039/B815812F.
[239] F. V. Singh, M. F. Z. J. Amaral, and H. A. Stefani, "Synthesis of symmetrical 1,3-diynes via homocoupling reaction of n-butyl alkynyltellurides," *Tetrahedron Letters*, vol. 50, no. 22, pp. 2636–2639, Jun. 2009, doi: 10.1016/j.tetlet.2009.03.078.
[240] G. Cahiez, A. Moyeux, J. Buendia, and C. Duplais, "Manganese- or Iron-Catalyzed Homocoupling of Grignard Reagents Using Atmospheric Oxygen as an Oxidant," *J. Am. Chem. Soc.*, vol. 129, no. 45, pp. 13788–13789, Nov. 2007, doi: 10.1021/ja075417k.
[241] Y. Nishihara, K. Ikegashira, K. Hirabayashi, J. Ando, A. Mori, and T. Hiyama, "Coupling Reactions of Alkynylsilanes Mediated by a Cu(I) Salt: Novel Syntheses of Conjugate Diynes and Disubstituted Ethynes," *J. Org. Chem.*, vol. 65, no. 6, pp. 1780–1787, Mar. 2000, doi: 10.1021/jo991686k.
[242] K. Yin, C. Li, J. Li, and X. Jia, "CuCl-catalyzed green oxidative alkyne homocoupling without palladium, ligands and bases," *Green Chemistry*, vol. 13, no. 3, p. 591, 2011, doi: 10.1039/c0gc00413h.
[243] R. A. Koevoets, S. Karthikeyan, P. C. M. M. Magusin, E. W. Meijer, and R. P. Sijbesma, "Cross-Polymerization of Hard Blocks in Segmented Copoly(ether urea)s," *Macromolecules*, vol. 42, no. 7, pp. 2609–2617, Apr. 2009, doi: 10.1021/ma801220q.
[244] K. Kikuchi, Y. Tatewaki, and S. Okada, "Self-Assembly and Solid-State Polymerization of Butadiyne Derivatives with Amide and Trialkoxyphenyl Groups," *BCSJ*, vol. 90, no. 3, pp. 298–305, Mar. 2017, doi: 10.1246/bcsj.20160347.
[245] K. S. Sindhu, A. P. Thankachan, P. S. Sajitha, and G. Anilkumar, "Recent developments and applications of the Cadiot–Chodkiewicz reaction," *Org. Biomol. Chem.*, vol. 13, no. 25, pp. 6891–6905, 2015, doi: 10.1039/C5OB00697J.

[246] V. Mouriès, R. Waschbüsch, J. Carran, and P. Savignac, “A Facile and High Yielding Synthesis of Symmetrical and Unsymmetrical Diarylalkynes Using Diethyl Dichloromethylphosphonate as Precursor,” *Synthesis*, vol. 1998, no. 03, pp. 271–274, Mar. 1998, doi: 10.1055/s-1998-2037.
[247] W. Yin, C. He, M. Chen, H. Zhang, and A. Lei, “Nickel-Catalyzed Oxidative Coupling Reactions of Two Different Terminal Alkynes Using O_2 as the Oxidant at Room Temperature: Facile Syntheses of Unsymmetric 1,3-Diynes,” *Org. Lett.*, vol. 11, no. 3, pp. 709–712, Feb. 2009, doi: 10.1021/ol8027863.
[248] E. Negishi, N. Okukado, S. F. Lovich, and F. T. Luo, “A method for the preparation of terminal and internal conjugated diynes via palladium-catalyzed cross-coupling,” *J. Org. Chem.*, vol. 49, no. 14, pp. 2629–2632, Jul. 1984, doi: 10.1021/jo00188a025.
[249] E. Negishi, M. Hata, and C. Xu, “A Strictly ‘Pair’-Selective Synthesis of Conjugated Diynes via Pd-Catalyzed Cross Coupling of 1,3-Diynylzincs: A Superior Alternative to the Cadiot−Chodkiewicz Reaction,” *Org. Lett.*, vol. 2, no. 23, pp. 3687–3689, Nov. 2000, doi: 10.1021/ol000270m.
[250] K. Biradha and R. Santra, “Crystal engineering of topochemical solid state reactions,” *Chem. Soc. Rev.*, vol. 42, no. 3, pp. 950–967, 2013, doi: 10.1039/C2CS35343A.
[251] G. Wegner, “Topochemical Polymerization of Monomers with Conjugated Triple Bonds,” *Makromol. Chem.*, vol. 154, no. 1, pp. 35–48, Apr. 1972, doi: 10.1002/macp.1972.021540103.
[252] A. Seher, “Die Konstitution der Isan- und Isanolsäure,” *Justus Liebigs Ann. Chem.*, vol. 589, no. 3, pp. 222–238, Oct. 1954, doi: 10.1002/jlac.19545890308.
[253] K. Lochner, H. Bässler, B. Tieke, and G. Wegner, “Photoconduction in Polydiacetylene Multilayer Structures and Single Crystals. Evidence for Band-to-Band Excitation,” *Physica Status Solidi (b)*, vol. 88, no. 2, pp. 653–661, Aug. 1978, doi: 10.1002/pssb.2220880232.
[254] A. Matsumoto, S. Nagahama, and T. Odani, “Molecular Design and Polymer Structure Control Based on Polymer Crystal Engineering. Topochemical Polymerization of 1,3-Diene Mono- and Dicarboxylic Acid Derivatives Bearing a Naphthylmethylammonium Group as the Countercation,” *Journal of the American Chemical Society*, vol. 122, no. 38, pp. 9109–9119, Sep. 2000, doi: 10.1021/ja001093n.
[255] D. Krishnan, A. Raj R B, and E. B. Gowd, “Topochemical polymerization of hierarchically ordered diacetylene monomers within the block copolymer domains,” *Polymer Chemistry*, vol. 10, no. 23, pp. 3154–3162, 2019, doi: 10.1039/C9PY00156E.
[256] S. Schrettl *et al.*, “Functional carbon nanosheets prepared from hexayne amphiphile monolayers at room temperature,” *Nature Chemistry*, vol. 6, no. 6, pp. 468–476, Jun. 2014, doi: 10.1038/nchem.1939.
[257] J. Deschamps *et al.*, “Tuning Topochemical Polymerization of Diacetylenes: A Joint Synthetic, Structural, Photophysical, and Theoretical Study of a Series of Analogues of a Known Reactive Monomer, 1,6-Bis(diphenylamino)-2,4-hexadiyne (THD),” *Chemistry of Materials*, vol. 22, no. 13, pp. 3961–3982, Jul. 2010, doi: 10.1021/cm1008703.
[258] Z. Wang *et al.*, “Stereoregular Two-Dimensional Polymers Constructed by Topochemical Polymerization,” *Macromolecules*, vol. 48, no. 9, pp. 2894–2900, May 2015, doi: 10.1021/acs.macromol.5b00109.
[259] G. N. Patel, J. D. Witt, and Y. P. Khanna, “Thermochromism in polydiacetylene solutions,” *Journal of Polymer Science: Polymer Physics Edition*, vol. 18, no. 6, pp. 1383–1391, Jun. 1980, doi: 10.1002/pol.1980.180180616.
[260] D. Bloor, “FTIR-Raman spectroscopy of polydiacetylenes with chiral pendent groups,” *Polymer*, vol. 40, no. 14, pp. 3901–3908, Jun. 1999, doi: 10.1016/S0032-3861(98)00618-1.
[261] Y. Lu *et al.*, “Self-assembly of mesoscopically ordered chromatic polydiacetylene/silica nanocomposites,” *Nature*, vol. 410, no. 6831, pp. 913–917, Apr. 2001, doi: 10.1038/35073544.

[262] T. Aida and K. Tajima, “Photoluminescent Silicate Microsticks Containing Aligned Nanodomains of Conjugated Polymers by Sol-Gel-Based In Situ Polymerization,” *Angewandte Chemie International Edition*, vol. 40, no. 20, pp. 3803–3806, Oct. 2001, doi: 10.1002/1521-3773(20011015)40:20<3803::AID-ANIE3803>3.0.CO;2-T.

[263] Y. Wang, L. Li, K. Yang, L. A. Samuelson, and J. Kumar, “Nanocrystalline TiO_2 -Catalyzed Solid-State Polymerization of Diacetylene in the Visible Region,” *J. Am. Chem. Soc.*, vol. 129, no. 23, pp. 7238–7239, Jun. 2007, doi: 10.1021/ja071296c.

[264] N. Belman, A. Berman, V. Ezersky, Y. Lifshitz, and Y. Golan, “Transmission electron microscopy of epitaxial PbS nanocrystals on polydiacetylene Langmuir films,” *Nanotechnology*, vol. 15, no. 4, pp. S316–S321, Apr. 2004, doi: 10.1088/0957-4484/15/4/036.

[265] M. Kamath *et al.*, “Kinetics of diacetylene polymerization: an FT-Raman study,” *Macromolecules*, vol. 26, no. 22, pp. 5954–5958, Oct. 1993, doi: 10.1021/ma00074a017.

[266] D. E. Parry, “Electronic band structure of model polydiacetylene chains,” *Chemical Physics Letters*, vol. 43, no. 3, pp. 597–599, Nov. 1976, doi: 10.1016/0009-2614(76)80632-X.

[267] S. Kumar, “Self-organization of disc-like molecules: chemical aspects,” *Chem. Soc. Rev.*, vol. 35, no. 1, pp. 83–109, 2006, doi: 10.1039/B506619K.

[268] C. Reanprayoon, J. Gasiorowski, M. Sukwattanasinitt, N. S. Sariciftci, and P. Thamyongkit, “Polydiacetylene-nested porphyrin as a potential light harvesting component in bulk heterojunction solar cells,” *RSC Adv.*, vol. 4, no. 6, pp. 3045–3050, 2014, doi: 10.1039/C3RA45373A.

[269] L. Li, Y. Wang, F. Yan, L. A. Samuelson, and J. Kumar, “Photosensitized Solid-state Polymerization of Diacetylenes in Nanoporous TiO_2 Structures,” *Journal of Macromolecular Science, Part A*, vol. 47, no. 12, pp. 1161–1166, Oct. 2010, doi: 10.1080/10601325.2010.518813.

[270] K. Lochner, H. Bassler, L. Sebastian, G. Weiser, G. Wegner, and V. Enkelmann, “Sensitized photoconduction in a polydiacetylene crystal (DCHD),” *Chemical Physics Letters*, vol. 78, no. 2, pp. 366–370, Mar. 1981, doi: 10.1016/0009-2614(81)80034-6.

[271] J. H. Song, T. J. Kang, Y. D. Cho, S. H. Lee, and J. S. Kim, “The fabrication and characterization of the photovoltaic cells composed of polydiacetylene and fullerene,” *Fibers Polym*, vol. 7, no. 3, pp. 217–222, Sep. 2006, doi: 10.1007/BF02875675.

[272] P. Muthitamongkol, C. Thanachayanont, and M. Sukwattanasinitt, “Fabrication and characterization of solar cells containing polydiacetylene,” *Current Applied Physics*, vol. 11, no. 1, pp. S163–S165, Jan. 2011, doi: 10.1016/j.cap.2010.11.092.

[273] Y. Wang, K. Yang, X. Wang, R. Nagarajan, L. A. Samuelson, and J. Kumar, “In situ polymerization of amphiphilic diacetylene for hole transport in solid state dye-sensitized solar cells,” *Organic Electronics*, vol. 7, no. 6, pp. 546–550, Dec. 2006, doi: 10.1016/j.orgel.2006.07.013.

[274] H. Choi *et al.*, “An Efficient Dye-Sensitized Solar Cell with an Organic Sensitizer Encapsulated in a Cyclodextrin Cavity,” *Angew. Chem. Int. Ed.*, vol. 48, no. 32, pp. 5938–5941, Jul. 2009, doi: 10.1002/anie.200902013.

[275] M. Giesbers, A. T. M. Marcelis, and H. Zuilhof, “Simulation of XPS C1s Spectra of Organic Monolayers by Quantum Chemical Methods,” *Langmuir*, vol. 29, no. 15, pp. 4782–4788, Apr. 2013, doi: 10.1021/la400445s.

[276] A. Shafiee, M. Mat Salleh, and M. Yahaya, “Fabrication of organic solar cells based on a blend of poly (3-octylthiophene-2, 5-diyl) and fullerene derivative using inkjet printing technique,” Weihai, China, Jul. 2009, p. 74932D. doi: 10.1117/12.843467.

[277] C. Giansante, I. Infante, E. Fabiano, R. Grisorio, G. P. Suranna, and G. Gigli, “‘Darker-than-Black’ PbS Quantum Dots: Enhancing Optical Absorption of Colloidal Semiconductor Nanocrystals via Short Conjugated Ligands,” *Journal of the American Chemical Society*, vol. 137, no. 5, pp. 1875–1886, Feb. 2015, doi: 10.1021/ja510739q.

[278] B. Kundu and A. J. Pal, “Ligand-Mediated Energy-Level Modification in PbS Quantum Dots as Probed by Density of States (DOS) Spectra,” *J. Phys. Chem. C*, vol. 122, no. 21, pp. 11570–11576, May 2018, doi: 10.1021/acs.jpcc.8b03022.
[279] N. Zhao *et al.*, “Colloidal PbS Quantum Dot Solar Cells with High Fill Factor,” *ACS Nano*, vol. 4, no. 7, pp. 3743–3752, Jul. 2010, doi: 10.1021/nn100129j.
[280] D. M. Kroupa *et al.*, “Control of Energy Flow Dynamics between Tetracene Ligands and PbS Quantum Dots by Size Tuning and Ligand Coverage,” *Nano Letters*, vol. 18, no. 2, pp. 865–873, Feb. 2018, doi: 10.1021/acs.nanolett.7b04144.
[281] N. Kim, G. S. Lee, C. Cui, and D. J. Ahn, “A facile fabrication of polydiacetylene nanowires and their response to aqueous solutions with basicity,” *Synthetic Metals*, vol. 213, pp. 42–46, Mar. 2016, doi: 10.1016/j.synthmet.2015.12.025.
[282] J. W. Chan, J. Shin, C. E. Hoyle, C. N. Bowman, and A. B. Lowe, “Synthesis, Thiol−Yne ‘Click’ Photopolymerization, and Physical Properties of Networks Derived from Novel Multifunctional Alkynes,” *Macromolecules*, vol. 43, no. 11, pp. 4937–4942, Jun. 2010, doi: 10.1021/ma1004452.
[283] J. W. Chan, H. Zhou, C. E. Hoyle, and A. B. Lowe, “Photopolymerization of Thiol-Alkynes: Polysulfide Networks,” *Chem. Mater.*, vol. 21, no. 8, pp. 1579–1585, Apr. 2009, doi: 10.1021/cm803262p.
[284] B. D. Fairbanks, T. F. Scott, C. J. Kloxin, K. S. Anseth, and C. N. Bowman, “Thiol−Yne Photopolymerizations: Novel Mechanism, Kinetics, and Step-Growth Formation of Highly Cross-Linked Networks,” *Macromolecules*, vol. 42, no. 1, pp. 211–217, Jan. 2009, doi: 10.1021/ma801903w.
[285] R. van Geel, G. J. M. Pruijn, F. L. van Delft, and W. C. Boelens, “Preventing Thiol-Yne Addition Improves the Specificity of Strain-Promoted Azide–Alkyne Cycloaddition,” *Bioconjugate Chemistry*, vol. 23, no. 3, pp. 392–398, Mar. 2012, doi: 10.1021/bc200365k.
[286] M. Aerts, F. C. M. Spoor, F. C. Grozema, A. J. Houtepen, J. M. Schins, and L. D. A. Siebbeles, “Cooling and Auger Recombination of Charges in PbSe Nanorods: Crossover from Cubic to Bimolecular Decay,” *Nano Letters*, vol. 13, no. 9, pp. 4380–4386, Sep. 2013, doi: 10.1021/nl402223q.
[287] S. Maiti *et al.*, “Monitoring Self-Assembly and Ligand Exchange of PbS Nanocrystal Superlattices at the Liquid/Air Interface in Real Time,” *The Journal of Physical Chemistry Letters*, vol. 9, no. 4, pp. 739–744, Feb. 2018, doi: 10.1021/acs.jpclett.7b03278.
[288] G. Iucci *et al.*, “XPS, NEXAFS and theoretical study of phenylacetylene adsorbed on Cu(100),” *Chemical Physics*, vol. 302, no. 1–3, pp. 43–52, Jul. 2004, doi: 10.1016/j.chemphys.2004.03.012.
[289] W. Koh, S. R. Saudari, A. T. Fafarman, C. R. Kagan, and C. B. Murray, “Thiocyanate-Capped PbS Nanocubes: Ambipolar Transport Enables Quantum Dot Based Circuits on a Flexible Substrate,” *Nano Lett.*, vol. 11, no. 11, pp. 4764–4767, Nov. 2011, doi: 10.1021/nl202578g.
[290] A. R. Kirmani *et al.*, “Remote Molecular Doping of Colloidal Quantum Dot Photovoltaics,” *ACS Energy Lett.*, vol. 1, no. 5, pp. 922–930, Nov. 2016, doi: 10.1021/acsenergylett.6b00429.
[291] L. Hu, A. Mandelis, X. Lan, A. Melnikov, S. Hoogland, and E. H. Sargent, “Imbalanced charge carrier mobility and Schottky junction induced anomalous current-voltage characteristics of excitonic PbS colloidal quantum dot solar cells,” *Solar Energy Materials and Solar Cells*, vol. 155, pp. 155–165, Oct. 2016, doi: 10.1016/j.solmat.2016.06.012.
[292] Y. Wang *et al.*, “In Situ Passivation for Efficient PbS Quantum Dot Solar Cells by Precursor Engineering,” *Adv. Mater.*, vol. 30, no. 16, p. 1704871, Apr. 2018, doi: 10.1002/adma.201704871.
[293] E. M. Miller *et al.*, “Revisiting the Valence and Conduction Band Size Dependence of PbS Quantum Dot Thin Films,” *ACS Nano*, vol. 10, no. 3, pp. 3302–3311, Mar. 2016, doi: 10.1021/acsnano.5b06833.

[294] J. Nishide, T. Oyamada, S. Akiyama, H. Sasabe, and C. Adachi, “High Field-Effect Mobility in an Organic Thin-Film Transistor with a Solid-State Polymerized Polydiacetylene Film as an Active Layer,” *Adv. Mater.*, vol. 18, no. 23, pp. 3120–3124, Dec. 2006, doi: 10.1002/adma.200601419.
[295] T. Koyanagi *et al.*, “Organic Field-effect Transistor Based on a Thin Film of Polydiacetylene Prepared from 10,12-Pentacosadiynoic Acid,” *Chem. Lett.*, vol. 35, no. 1, pp. 20–21, Jan. 2006, doi: 10.1246/cl.2006.20.
[296] Z. G. Soos, M. H. Hennessy, and G. Wen, “Frenkel and charge transfer states of conjugated polymers and molecules,” *Chemical Physics*, vol. 227, no. 1–2, pp. 19–32, Feb. 1998, doi: 10.1016/S0301-0104(97)00307-8.
[297] R. A. Sheldon, “Metrics of Green Chemistry and Sustainability: Past, Present, and Future,” *ACS Sustainable Chem. Eng.*, vol. 6, no. 1, pp. 32–48, Jan. 2018, doi: 10.1021/acssuschemeng.7b03505.
[298] S. Wang, L. Yu, P. Li, L. Meng, and L. Wang, “Copper(I) Iodide Catalyzed Cross-Coupling Reaction of Terminal Alkynes with 1-Bromoalkynes: A Simple Synthesis of Unsymmetrical Buta-1,3-diynes,” *Synthesis*, vol. 2011, no. 10, pp. 1541–1546, May 2011, doi: 10.1055/s-0030-1259998.
[299] S. S. Zade, N. Zamoshchik, and M. Bendikov, “From Short Conjugated Oligomers to Conjugated Polymers. Lessons from Studies on Long Conjugated Oligomers,” *Acc. Chem. Res.*, vol. 44, no. 1, pp. 14–24, Jan. 2011, doi: 10.1021/ar1000555.
[300] L. Vegard, “Die Konstitution der Mischkristalle und die Raumfüllung der Atome,” *Zeitschrift für Physik*, vol. 5, pp. 17–26, 1921.
[301] C. K. Chiang *et al.*, “Electrical Conductivity in Doped Polyacetylene,” *Phys. Rev. Lett.*, vol. 39, no. 17, pp. 1098–1101, Oct. 1977, doi: 10.1103/PhysRevLett.39.1098.
[302] W. K. Bae *et al.*, “Highly Effective Surface Passivation of PbSe Quantum Dots through Reaction with Molecular Chlorine,” *J. Am. Chem. Soc.*, vol. 134, no. 49, pp. 20160–20168, Dec. 2012, doi: 10.1021/ja309783v.
[303] A. P. Kirk and M. V. Fischetti, “Fundamental limitations of hot-carrier solar cells,” *Phys. Rev. B*, vol. 86, no. 16, p. 165206, Oct. 2012, doi: 10.1103/PhysRevB.86.165206.